

Tissue- and cell-type specific compartmentalization  
of surface-modified fluorescent nanoparticles:  
Enhanced detection with spectral imaging  
fluorescence microscopy

PhD thesis

**Kata Kenesei**

Semmelweis University  
Molecular Medicine Doctoral School



Supervisor: Emília Madarász, DSc

Official reviewers: László Péter Bíró, DSc  
Sára Tóth, PhD

Head of the Final Examination Committee: Pál Röhlich MD, DSc  
Members of the Final Examination Committee: László Kőhidai MD, PhD  
István Krizbai MD, DSc

Budapest  
2016

**TABLE OF CONTENT**

1. LIST OF ABBREVIATIONS .....	4
2. INTRODUCTION .....	6
2.1. Nanomaterials and nanoparticles .....	6
2.2. Properties of nanoparticles .....	7
2.3. Health risks of NP production and application.....	8
2.3.1. Use of nanoparticles in consumer products.....	8
2.3.2. Health risks of NPs .....	10
2.4. NPs with non-toxic core materials .....	10
2.4.1. Polystyrene nanoparticles .....	10
2.4.2. Silica nanoparticles.....	11
2.5. Protein corona.....	12
2.5.1. Protein corona formation on NP surfaces.....	12
2.5.2. Effects of surface functional groups on corona formation .....	14
2.6. Detection of NPs in biological samples.....	15
2.6.1. Electron microscopy .....	15
2.6.2. Fluorescent light microscopy .....	16
3. OBJECTIVES.....	19
4. METHODS.....	20
4.1. Nanoparticles used in experiments .....	20
4.1.1. Polystyrene nanoparticles .....	20
4.1.2. Silica nanoparticles.....	20
4.2. Physicochemical characterization of polystyrene nanoparticles .....	21
4.2.1. Dynamic light scattering (DLS) measurements .....	21
4.2.2. Transmission electron microscopy measurements .....	21
4.2.3. Zeta-potential measurements .....	22
4.2.4. Assays on protein adsorption.....	22
4.3. Cell cultures.....	22
4.3.1. Primary astroglial and neuronal cultures .....	22
4.3.2. Primary microglial cultures .....	23
4.3.3. BV2 microglial cells.....	23
4.3.4. NE-4C stem cells .....	24

4.3.5. Radial glia.....	25
4.4. In vitro uptake of nanoparticles .....	25
4.5. In vivo distribution of polystyrene nanoparticles .....	26
4.6. Microscopic evaluation.....	26
4.6.1. Immunohistochemical procedures .....	27
4.6.2. Detection of particles by spectral imaging fluorescence microscopy .....	28
5. RESULTS.....	30
5.1. Physicochemical characterization of nanoparticles .....	30
5.1.1. Polystyrene nanoparticles .....	30
5.1.2. Silica nanoparticles.....	34
5.2. In vitro cellular uptake of nanoparticles .....	36
5.2.1. Interaction of PS-NPs with neural stem- and tissue-type cells.....	36
5.2.2. Interaction of Si-NP with neural stem- and tissue-type cells .....	41
5.3. Optimization of NP-detection by spectral imaging fluorescence microscopy ...	45
5.3.1. Optimization of imaging.....	46
5.3.2. Spectra of nanoparticles used in experiments are stable .....	47
5.4. In vivo distribution of polystyrene nanoparticles .....	50
6. DISCUSSION.....	61
7. CONCLUSIONS .....	68
8. SUMMARY .....	70
9. ÖSSZEFOGLALÁS .....	71
10. REFERENCES .....	72
11. PUBLICATIONS .....	82
Publications related to the PhD dissertation .....	82
Other publications .....	82
12. ACKNOWLEDGEMENTS .....	83

**1. LIST OF ABBREVIATIONS**

<b>AK-cyclo[RGDfC]</b>	– peptide polymer with cyclic arginyl-glycyl-aspartic acid motifs
<b>APTES</b>	– 3-aminopropyltriethoxysilane
<b>BSA</b>	– bovine serum albumin
<b>BV2</b>	– mouse microglial cell line
<b>CPI</b>	– Nanotechnology Consumer Product Inventory
<b>CX3CR1</b>	– CX3C chemokine receptor 1 or fractalkine receptor 1
<b>DAPI</b>	– 4',6-diamidino-2-phenylindole, nuclear staining
<b>DLS</b>	– dynamic light scattering
<b>DMEM</b>	– Dulbecco's modified Eagle's cell culture medium
<b>EGF</b>	– epidermal growth factor
<b>F12</b>	– Ham's F12 nutrient mixture
<b>FCS</b>	– fetal calf serum
<b>FITC</b>	– fluorescein-isothiocyanate
<b>GFAP</b>	– glial fibrillary acidic protein
<b>Iba-1</b>	– ionized calcium-binding adapter molecule 1
<b>ITS</b>	– insulin, transferrin and selenium solution
<b>LDH assay</b>	– lactate dehydrogenase release assay
<b>M</b>	– molecular weight marker in SDS-PAGE analysis
<b>MEM</b>	– minimum essential medium
<b>MEM-F12-ITS</b>	– 1:1 mixture of MEM:F12 supplemented with 1 % ITS
<b>MEM-F12-B27</b>	– 1:1 mixture of MEM:F12 supplemented with 1 % B27
<b>MPTMS</b>	– 3-mercaptopropyltrimethoxysilane
<b>MRI</b>	– magnetic resonance imaging
<b>MTT assay</b>	– colorimetric assay for assessing cell metabolic activity
<b>NE-4C</b>	– mouse neuroectodermal stem cell line
<b>NIR</b>	– near-infrared
<b>NP</b>	– nanoparticles
<b>p53</b>	– cellular tumor suppressor protein p53
<b>PBS</b>	– phosphate buffered saline
<b>PEG</b>	– polyethylene glycol
<b>PET</b>	– positron emission tomography

<b>PFA</b>	– paraformaldehyde
<b>PLL</b>	– poly-L-lysine
<b>PS-NP</b>	– polystyrene nanoparticles
<b>PS-COOH</b>	– carboxylated polystyrene nanoparticles
<b>PS-PEG</b>	– PEGylated polystyrene nanoparticles
<b>PVP</b>	– polyvinylpyrrolidone
<b>RA</b>	– <i>all-trans</i> retinoic acid
<b>ROI</b>	– region of interest
<b>SD</b>	– spectral detector
<b>SDS-PAGE</b>	– sodium dodecyl sulfate polyacrylamide gel electrophoresis
<b>SEM</b>	– scanning electron microscopy
<b>SiO<sub>2</sub>-NH<sub>2</sub></b>	– amino-modified silica nanoparticles
<b>SiO<sub>2</sub>-NP</b>	– silica nanoparticles
<b>SiO<sub>2</sub>-PVP</b>	– PVP-coated silica nanoparticles
<b>SiO<sub>2</sub>-SH</b>	– mercapto-modified silica nanoparticles
<b>SPECT</b>	– single photon emission computed tomography
<b>SR</b>	– spectral ratio
<b>TEM</b>	– transmission electron microscopy

## 2. INTRODUCTION

### 2.1. Nanomaterials and nanoparticles

Nanomaterials are usually categorized as structured components with at least one dimension in the 1-100 nm range (ISO/TS 80004-1:2015, (ISO 2015)). Within the broad definition, nanostructured materials can be classified according to their internal or surface structures in the nanoscale, or, in case of nano-objects, according to their “external” dimensions in the 1-100 nm range. Nano-objects, with one dimension in the sub-micron range are layers, such as graphene or thin films; materials with two dimensions in the nanoscale include nanofibers. My thesis work was focused on nanoparticles (NP), which have three external dimensions in the nanoscale (Figure 1; (ISO 2015)).

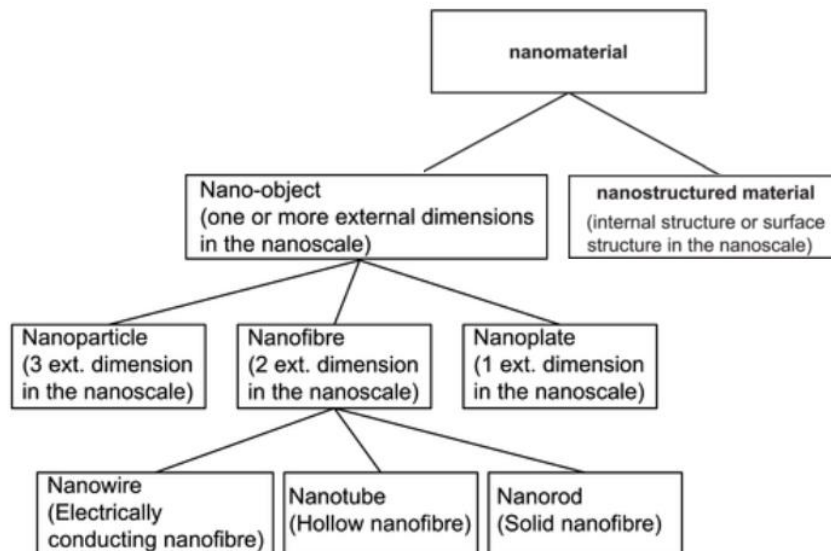


**Figure 1: Hierarchy of nanomaterials**

Nanomaterials can be classified into several categories based on their external or internal dimensions in the nanometer range.

While nanotechnology is a new and rapidly growing field that cuts across an array of industrial and scientific sectors, the coexistence with and the use of nanoparticles has a long history. In stained glass and pottery gold nanoparticles had been used for centuries as inorganic dyes to create red color (Cao and Wang 2004). Nanoparticles are inherent components of the nature as well. Natural nanoparticles exist in the environment, as the products of biological decay, forest fires and volcanic activity, they occur naturally in ocean spray, fine sand or even cosmic dust (Strambeanu et al. 2015) and can be created by plants and bacteria (Lin et al. 2014). NPs are generated by human activity as incidental

by-products of combustion or even food cooking, and more recently, as derivatives of vehicle exhausts of car or airplane engines. Engineered nanoparticles, which facilitate the most dramatic technological advances, are novel products of human activity and are produced in rapidly growing quantities all over the World.

## 2.2. Properties of nanoparticles

Regarding physicochemical characteristics, nanoparticles lay between molecular structures and bulk materials. Materials with known properties in the bulk form can exert new characteristics in the nanoscale range. The unique characteristics of NPs arise from the small size and their consequent high surface-to-volume ratio. Compared to bulk material, a much larger proportion of atoms are surface-exposed atoms in nanoparticles. Figure 2 shows, how the percentage of the surface atoms changes with the cluster diameter for palladium. When the particles change from centimeter size to nanometer size, the surface area and the surface energy increase seven orders of magnitude (Cao and Wang 2004).

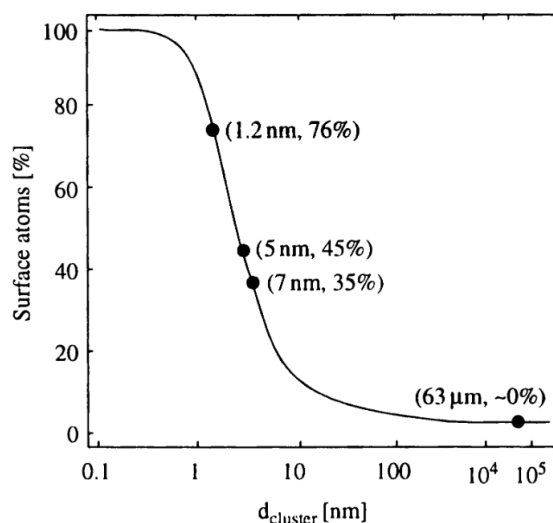


**Figure 2: The percentage of surface atoms changes with the palladium cluster diameter**

The total number of surface exposed atoms increases with the decrease of the cluster diameter, which in turn will strongly effect the overall surface energy. (C. Nützenadel 2000)

Surface atoms have fewer neighbors, thus are prone to less cohesive energy and higher chemical reactivity. The resulting huge surface energy creates unique mechanical, electrical, thermodynamical properties, changes the catalytic activity of NPs and makes

NPs advantageous for various applications. The increased activity makes NPs more prone to reactions with the environment and also with each other, which can result in formation of homo- and hetero-agglomerates. One of the great challenges in fabrication and processing of nanomaterials is to overcome the surface energy, and to prevent the growth in size, driven by the natural force to reduce the overall surface energy (Cao and Wang 2004). In parallel with the surface-effects, quantum mechanical properties of materials are also altered in the nanometer range. The energy-states of electrons are relatively easily modified in nanoparticles, leading to characteristic semiconductor, magnetic and optical behaviour (e.g. surface plasmon resonance, or particle size dependent color and emitted light) (Roduner 2006).

The unique physicochemical properties that make NPs attractive for pioneering research, however, may bring potential health hazards. Regarding the increased production, the widespread industrial, medical and domestic applications, the enhanced presence of engineered NPs in our surrounding raises serious questions concerning their interaction with biological systems.

### **2.3. Health risks of NP production and application**

#### *2.3.1. Use of nanoparticles in consumer products*

Many authorities predict that applications of nanotechnologies will pervade all areas of life and will enable dramatic advances (ISO 2015). According to the Nanotechnology Consumer Product Inventory (CPI, <http://www.nanotechproject.org>) the number of products containing NPs is continuously increasing (Figure 3).

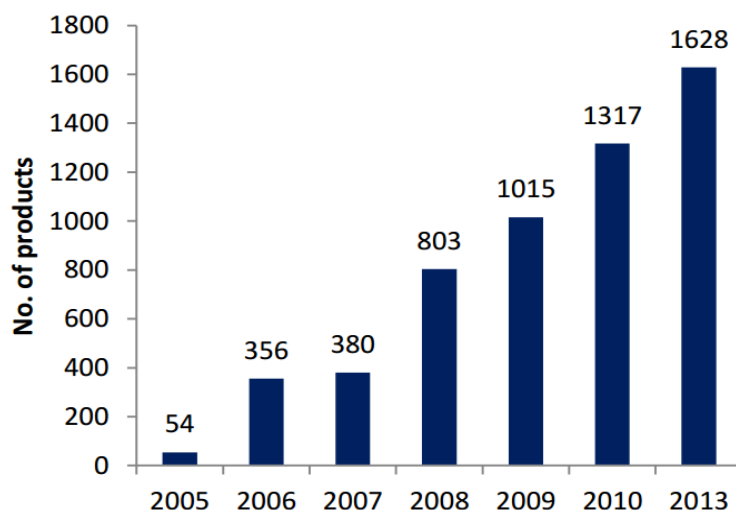


**Figure 3: Number of consumer products containing nanoparticles**

The number of NP-containing consumer products, increased ~30-fold from 2005 to 2013. (<http://www.nanotechproject.org>)

Nanomaterials are widely used in various consumer goods, from electronics and wall paint to clothing, food and personal care products (e.g. cosmetics and sunscreens). Nano-additives are usually used to improve handling, stability and efficacy of the products (Vance et al. 2015).

In nanomedicine nanoparticles may find application in drug delivery, bio-imaging, diagnostics and therapeutics. NPs can modify the kinetics, body distribution and drug release of an associated drug. A famous example of NP-mediated drug delivery is the anti-cancer nanoliposomal doxorubicin (Doxil®), the first FDA-approved nano-drug, which can "passively target" and attack tumors due to the enhanced penetration of nanoliposomes and the retention of encapsulated doxorubicin (Barenholz 2012).

Furthermore, several NP-based bio-imaging techniques are used or are under development. NP probes have been used in conjunction with magnetic resonance imaging (MRI), positron emission tomography (PET), single photon emission computed tomography (SPECT), and near-infrared (NIR) fluorescence imaging (Geng et al. 2014, Leary and Key 2014, Bouccara et al. 2015). Given the high performance of nanostructure-based NP-probes, application in human subjects is appealing (Hu et al. 2010). Prior to clinical application, however, a comprehensive understanding of the biological effects of diverse types of NPs is essential including toxicity, biodistribution and pharmacokinetics.

### 2.3.2. *Health risks of NPs*

Developments in nanomedicine aim to improve efficacy of NPs by increasing specific cellular uptake and tissue permeation (Chen et al. 2014), whereas consumers and factory workers should be protected against non-intended exposure and uptake of nanoparticles. While early and intensive efforts have been made to study the toxicity of various NPs, keeping pace with the fast development of nanotechnology is challenging nanosafety measures. For testing the safety of nanoparticles researchers, regulators and protection agencies should possess fast and reliable measurement systems and evaluation protocols supported by robust standards (ISO 2015).

To facilitate hazard assessment of NPs several classification approaches have been proposed. NPs can be classified into categories based on the similarities in their physicochemical properties and their biological effects. Testing according to the category requirements, can reduce the number of case-by-case evaluation (Gebel et al. 2014). In contrast to fibrous nanomaterials (Champion and Mitragotri 2006), the shape of spherical nanoparticles is not considered as an immediate hazard. The major mode of action in case of spherical NPs is chemically mediated toxicity. The adverse effects may originate from (1) the release of toxicants from NPs, usually ions, (2) the reactions of active surface groups and (3) the catalytic activity of NP surfaces (Gebel et al. 2014).

## **2.4. NPs with non-toxic core materials**

Nanoparticles, and especially non-metal nanoparticles, are widely used in biomedical applications because of the biologically inert or biosimilar properties. From the variety of NPs with non-toxic core material, the properties of two widely produced and applied NPs are presented.

### 2.4.1. *Polystyrene nanoparticles*

Polystyrene (PS) is a nontoxic and not carcinogenic polymer. Due to its inertness and biocompatibility, polystyrene is widely used for the production of biomedical devices and laboratory equipment. It is a well characterized and extensively used polymer, with many applications in the everyday life (European Commission Risk Assessment Report 2002). In the present EU regulation, both styrene and polystyrene are listed without any restriction to come into contact with food (EU 2008). Consumers are continuously exposed to polystyrene and low-dose styrene residues from food-packaging. REACH

(Registration, Evaluation, Authorisation and Restriction of Chemicals) regulation established a “derived no effect level” for long-term, oral route exposure in the general population, which was 2.1 mg/kg bodyweight /day for styrene (Gelbke et al. 2014). Polystyrene does not degrade in the cellular environment and exhibits no short-term cytotoxicity, facilitating its use in food and medical products. On the other hand, styrene’s elimination is slow and it can be bio-transformed into styrene-7,8-oxide in the liver and excreted as catabolites (Filser and Gelbke 2016).

Polystyrene nanoparticles are commercially available in plain or in fluorescently labelled forms, synthesized in various sizes with diverse surface functional groups. Such particles are used in many applications, including diagnostic tests, flow cytometry, fluorescent microscopy and as calibration particle standards.

Despite of the non-toxic nature of bulk polystyrene and styrene, several recent data indicated mild toxicity of PS nanoparticles (Lunov et al. 2011, Fröhlich et al. 2012, Mahler et al. 2012, Paget et al. 2015). Experimental data indicated that the cytotoxic effects were mediated by surface functional groups and not by the core material. In general, positively charged PS-NPs with cationic functional groups, showed higher cytotoxicity compared to negatively charged or neutral particles (Hardy et al. 2012, Paget et al. 2015, Ruenraroengsak and Tetley 2015). The mild or non-toxic properties allowed us to use polystyrene NPs for studying the effects of surface functionalization on the interactions of NPs with biological material.

#### 2.4.2. *Silica nanoparticles*

The term silica, refers to naturally occurring or anthropogenic materials composed of silicon dioxide (SiO<sub>2</sub>), which appear in two major forms, i.e., crystalline and amorphous. Crystalline silica is most commonly found in nature as quartz, and is a basic component of soil, sand, granite, and many other minerals, as well as glass. While silica is regarded generally as a non-toxic chemical, occupational exposure to crystalline silica dust (for example in case of construction and mine workers) was associated with an increased risk for pulmonary diseases such as silicosis, tuberculosis, chronic bronchitis, and lung cancer (Merget et al. 2002).

In contrast to crystalline silica, amorphous silica particles have been approved for oral administration for decades and are registered by the EU as a food additive with code E551 (OECD 2016). Synthetic amorphous silica is widely applied in processed foods, it is

added to prevent caking, poor flow, to control foaming, to clarify beverages or to carry flavors (EU 2011).

In medical applications amorphous silica nanoparticles have attracted significant interest as promising candidates for drug delivery systems (Garcia-Bennett 2011, Tang and Cheng 2013), imaging or diagnostic tools and anti-cancer therapeutics (Hirsch et al. 2003). For example, ultrasmall nonporous silica NPs were already approved for human clinical trial by the FDA for exploring targeted molecular imaging of tumors (Benezra et al. 2011, Bradbury et al. 2013).

As potential drug delivery vehicles, amorphous silica nanoparticles were shown to carry sufficient drug loads, efficiently cross physiological barriers to reach target sites (Baghirov et al. 2016, Mo et al. 2016). Further favorable properties of amorphous silica nanoparticles include good biocompatibility (Lu et al. 2010), versatile silane-chemistry for surface functionalization and tailoring of surface reactivity (Walcarius and Ganesan 2006), the ease of large-scale synthesis and the low cost of NP production.

Despite of the favorable properties and the potential medical applications, important questions were raised regarding the biosafety of amorphous silica particles. Sound evidence of safety is still missing, and relevant risk assessment has never been satisfactorily completed (Winkler et al. 2016).

## **2.5. Protein corona**

The biological identity of NPs can be altered by interactions with the physiological environment, through the formation of a biomolecular corona. The biomolecular corona is composed by several layers of compounds adsorbed from the actual environment. Particles can act by a ‘Trojan horse mechanism’, as chemicals bound to particle surfaces may be taken up by cells more efficiently. After particle uptake, the solubility and bioavailability of internalized compounds may increase due to the lower pH in phagolysosomes. This mechanism can enhance toxicity compared to the standard bulk material (Gebel et al. 2014).

### *2.5.1. Protein corona formation on NP surfaces*

NPs readily adsorb various chemical substances from their environments due to the highly reactive surface (Monopoli et al. 2012). Unless they are specifically designed to avoid it, NPs in contact with biological fluids are rapidly covered by a selected group of

biomolecules. The biomolecules on NP surfaces form the so-called protein corona that masks the “bare” NP-surface (Figure 4). Since the original surface of the particle is no longer “visible” to the cells, the corona governs the interactions of NPs with biological structures and plays a decisive role in the tissue- and cell-type-specific NP distribution (Monopoli et al. 2012, Salvati et al. 2013, Tenzer et al. 2013).

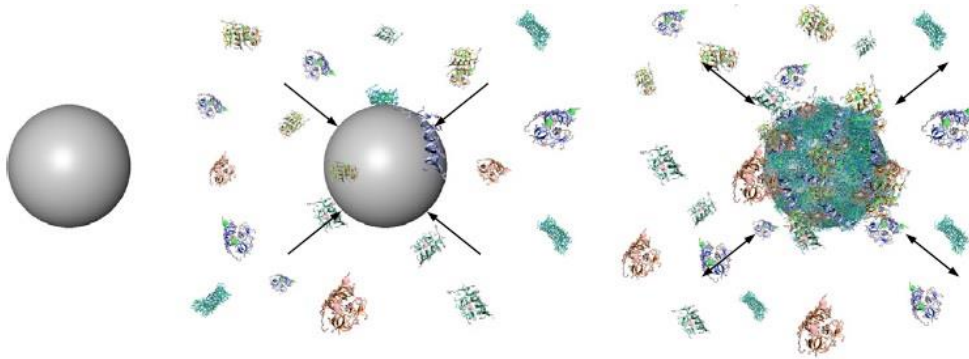


**Figure 4: Formation of nanoparticle corona:** In contact with biological fluids proteins and biomolecules adhere to “bare” nanoparticles. The surrounding layer around NP-surfaces is the so-called protein corona. (Elsaesser and Howard 2012)

The protein corona is changing dynamically over time. The composition and thickness of the adsorbed layers depends on the chemical properties of both the NP surface and the environment (Casals et al. 2010, Lundqvist et al. 2011, Casals and Puentes 2012). The “soft corona” that forms initially, consists of high-abundance and/or high-mobility proteins. Over time, the weakly bound, low-affinity proteins are replaced by high-affinity, tightly bound proteins that comprise the “hard corona” (Figure 5) (Fleischer and Payne 2014). The initial adsorption is mediated by protein-nanoparticle binding affinities, while later, protein-protein interactions play a role as well.

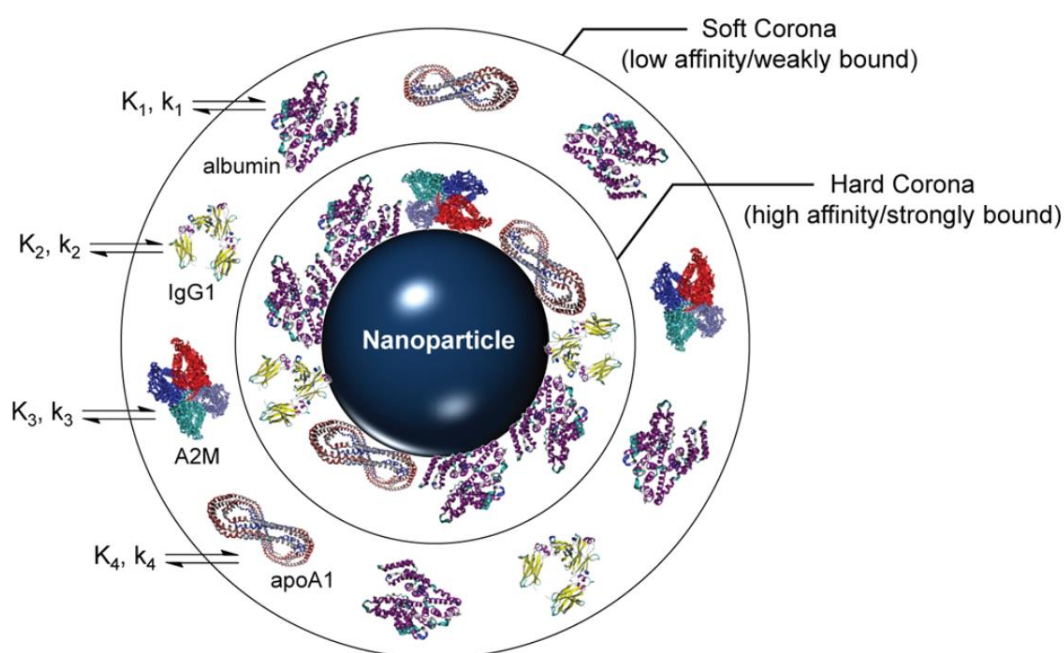


**Figure 5: Schematic representation of protein corona formation on a nanoparticle surface**

Protein adsorption is a kinetic ( $k$ ) and thermodynamic ( $K$ ) function of both the individual proteins and NP properties. Initially, high-abundance and/or high-mobility proteins bind to the nanoparticle surface, which are replaced gradually by proteins with lower-mobility but higher binding affinity. Serum proteins commonly observed in NP coronas are shown as a representative corona: serum albumin, immunoglobulin G1 (IgG1), alpha-2 macroglobulin (A2M), and apolipoprotein A-1 (apoA1) (Fleischer and Payne 2014). It has to be noted, that while the majority of biomolecules adsorbed from blood plasma are proteins, some minor traces of lipids have also been reported (Hellstrand et al. 2009).

The composition of the evolving protein corona is affected by various parameters. Physical and chemical properties of the nanoparticles, including size, shape, curvature, composition, surface charge (zeta-potential) and surface modifications play important role, just as the properties of the surrounding environment (Lundqvist et al. 2008). As a result of chemical exchange reactions, the corona is expected to change with time even within the same tissue environment (Casals et al. 2010, Casals and Puntès 2012, Milani et al. 2012), however, if particles are transferred to a new environment, significant evolution of the corona occurs and the final corona will contain the print of the NP's history (Lundqvist et al. 2011).

### 2.5.2. Effects of surface functional groups on corona formation

While NP surfaces are ultimately functionalized by the actual environment, this process can be regulated by changing the charge and chemical composition of NP surfaces. Via

functional groups, nanoparticles can gain activated or passivated surfaces, which attract or repel inorganic, organic and biological macromolecules, resulting particles with novel reactivity and consequently, absorbed bio-molecules with altered activity (Wang et al. 2011). By coating the NPs with specific functional groups, NPs can target certain cells or tissues (Mahon et al. 2012), or if coated with biologically inert substances, as hydrophilic polymers (Izak-Nau et al. 2013b, Sacchetti et al. 2013) they can avoid particular unwanted interactions.

Polyvinylpyrrolidone (PVP) and polyethylene glycol (PEG) polymers with different oligomer-numbers and linear or branching chains have been widely used to reduce the chemical reactivity of surfaces (Izak-Nau et al. 2013a, Sacchetti et al. 2013). Accordingly, protein adsorption and cellular uptake of NPs could be reduced by PEGylation and PVP-coating (Peracchia et al. 1999b, Essa et al. 2011, Murali et al. 2015). *In vivo* studies demonstrated that PEGylated and PVP-coated nanoparticles remained longer in the circulation due to their reduced attachment to vessel walls and cell surfaces (Peracchia et al. 1999a, Chilukuri et al. 2008, Fang et al. 2014).

## **2.6. Detection of NPs in biological samples**

Observations on nanoparticle distribution in cells and whole organisms are indispensable to localize the sites of interaction with living structures. Combining visualization techniques with antibody-based labelling methods enables the identification of cells by molecular phenotype. This allows to interpret the presence of NPs within the biological context.

Various imaging techniques can be used for localizing inorganic, metal or organic nanoparticles, yet all techniques have limitations, which often make NP-detection in the living body laborious. Here I introduce the advantages and disadvantages of the two most widely applied detection technique used to visualize inorganic nanoparticles. Several methods try to overcome the limitations of these techniques and meet the specific requirements of the detection of various types of NPs.

### *2.6.1. Electron microscopy*

Transmission and scanning electron microscopy (TEM, SEM) can provide a very high spatial resolution (down to 0.1 nm) and magnification (Krijnse Locker and Schmid 2013, Begemann and Galic 2016). It gives detailed information on subcellular structures and

shows the precise localization of NPs. However, the sample preparation for electron microscopy is more time taking compared to other microscopic methods and is prone to artifacts. Artifacts may be caused by chemical fixation, dehydration and staining with lead citrate or uranyl acetate (Shah et al. 2015, Chen et al. 2016); this renders image interpretation challenging. Analysis of NP distribution and tissue effects with electron microscopy requires a deep understanding of normal and diseased cellular ultrastructure. Additionally, a certain electron density of NPs is required for a contrasted image, hence electron microscopy is more often used for the visualization of electron-dense inorganic and metal NPs.

The time intensive sample preparation, the small analyzed volume and the limited analytical throughput of the method does not suggest to use electron microscopy as a high-throughput imaging technique for detecting NPs in tissues.

#### *2.6.2. Fluorescent light microscopy*

Fluorescent microscopy allows for a sensitive, efficient, and time- and cost-effective evaluation of large amounts of samples (Kobayashi et al. 2010). The capabilities of the technique largely satisfy demands by researchers and regulatory authorities. However, the resolution in optical microscopy is limited due to diffraction; the wavelength of light determines the maximum resolution of a microscope. The nanoparticle's size (typically being between 1 and 100 nm) is below the diffraction limit of ~ 250 nm, thus, only NP that cluster or form aggregates can be visualized directly.

NPs must be able to emit fluorescent light upon excitation to be detectable by fluorescent microscopy. Any surface labeling of NP, however, may possess the risk of changing their physicochemical characteristics and their bioreactivity. In contrast, NPs which encapsulate the fluorescent dye in their core structure and have an unlabeled shell leave the overall properties of NPs unchanged.

Despite its favorable properties, the core-shell structure limits the amount of dye per particle, lowering brightness. Moreover, the detection is further hindered by the high autofluorescence intensity of biological samples (Figure 6), resulting in a limited visualization of NPs due to the low signal-to-noise ratio.

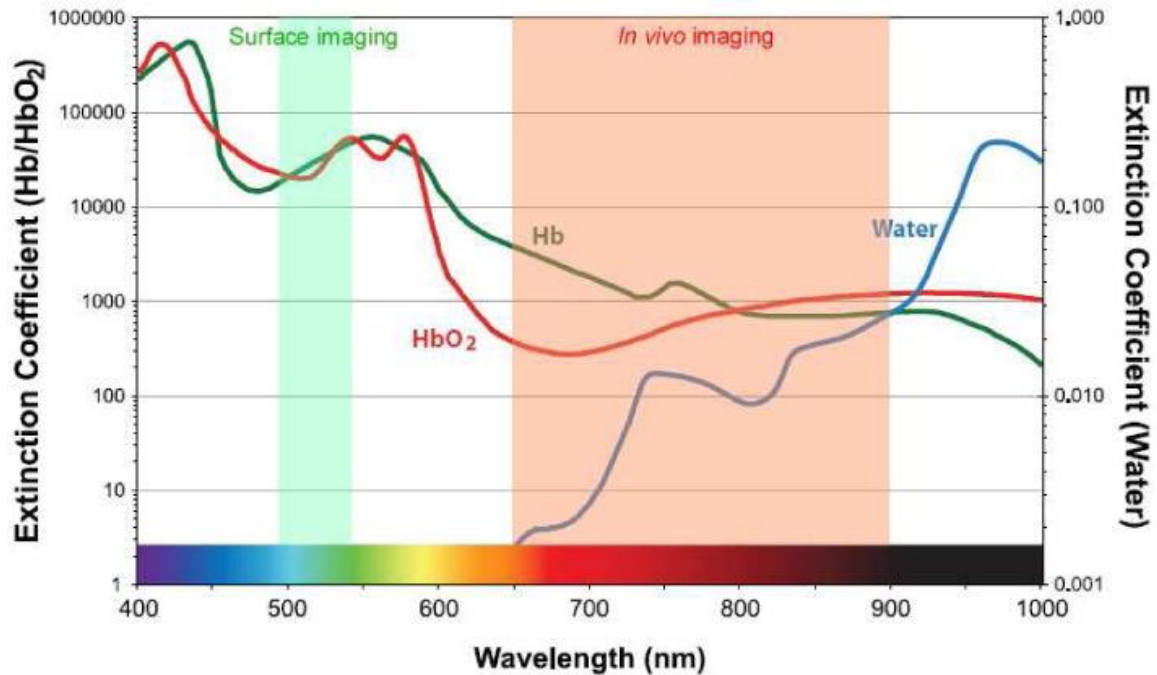


**Figure 6: Extinction coefficient value of water, oxy- and deoxy-hemoglobin** (Kobayashi et al. 2010)

Naturally occurring endogenous fluorophores (mostly hemoglobin and related molecules) can be excited in the same wavelength range as fluorescently labelled NPs, leading to high autofluorescence in biological samples.

Spectral imaging fluorescence microscopy provides a solution to overcome the limitations caused by low NP fluorescence intensity masked by high tissue autofluorescence. The technique combines conventional laser scanning confocal microscopy with a spectral detector (Figure 7). The basis of the image acquisition is that the emitted light of the sample is detected separately at consecutive wavelengths throughout a defined spectrum range, resulting a confocal image with spectral information about each pixel (Figure 8).

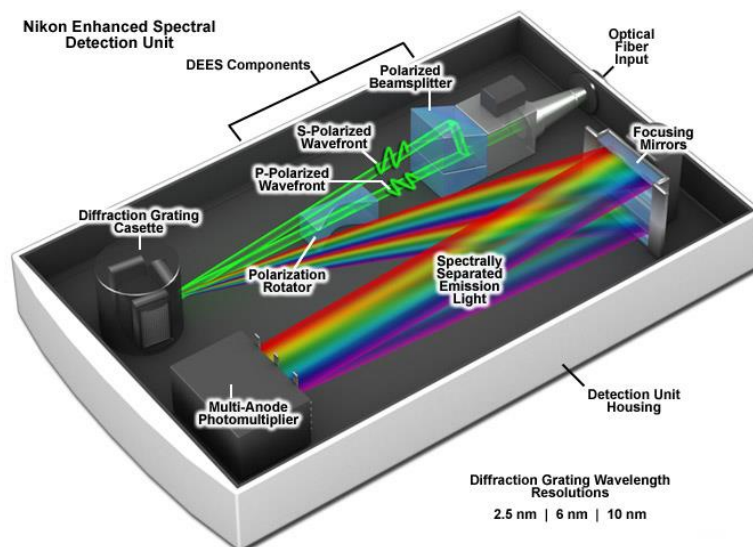


**Figure 7: Spectral detector for spectral image acquisition**

The emitted light of the sample is separated into different wavelengths by a diffraction grating and detected by a 32 channel multi-anode photomultiplier to acquire spectral images. With the different resolution of the diffraction grating, one can choose between greater spectral resolution (2.5nm, 6nm, 10nm) or wider detected spectrum range ( $\Sigma$ range = 80nm, 192nm, 320nm). (DEES: Diffraction Efficiency Enhancement System, [www.microscopyu.com](http://www.microscopyu.com))

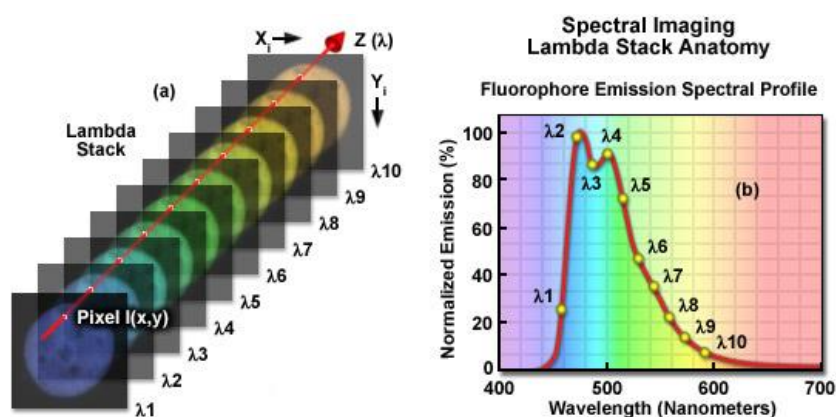


**Figure 8: Confocal images with embedded spectral information**

A spectral image consists of fluorescence intensity images on 32 different wavelengths detected by the spectral detector. Emission spectral profile (spectrum) of every pixel of the image can be drawn from the combined fluorescence intensity information.

The emission spectrum of a label dye in NPs differs unequivocally from the emission spectra of autofluorescent signals, helping the identification of NPs. Additionally the technique enables the use of multiple fluorescent labels, that cannot be distinguished by conventional fluorescence microscopy due to overlapping emission spectra (Dickinson et al. 2001).

### 3. OBJECTIVES

In the work, which provided the basis of the dissertation I investigated the physicochemical characteristics, and the interactions of fluorescent nanoparticles with biological material, including cellular uptake *in vitro* and tissue distribution *in vivo*. My interest was focused on the altered biological behavior of silica and polystyrene nanoparticles with equal size but coated with distinct functional groups; ranging from strong negative surface charges (PS-COOH, SiO<sub>2</sub>, SiO<sub>2</sub>-SH) to positive (SiO<sub>2</sub>-NH<sub>2</sub>) or passivated surfaces (PS-PEG, SiO<sub>2</sub>-PVP). Experimental work aimed to answer the following questions:

- Are polystyrene- (PS-COOH, PS-PEG) and silica nanoparticles (SiO<sub>2</sub>, SiO<sub>2</sub>-NH<sub>2</sub>, SiO<sub>2</sub>-SH and SiO<sub>2</sub>-PVP) good models for investigating the effects of surface characteristics?
- How does the chemical surface composition affect the behavior of NPs in inorganic or organic solutions?
- Which cell types can interact with and internalize the distinct types of nanoparticles in serum-free *in vitro* conditions?
- How do polystyrene nanoparticles with different surface functionalization penetrate into and clear from different organs and tissues? Special attention was paid to barrier functions of the blood brain barrier and the placenta, and to the accumulation and storage of nanoparticles in various organs.
- Can the detection efficiency of fluorescent nanoparticles be improved? Does the adaptation of spectral imaging fluorescence microscopy provide a reliable imaging approach to distinguish particle-fluorescence from tissue autofluorescence?

## 4. METHODS

### 4.1. Nanoparticles used in experiments

#### 4.1.1. Polystyrene nanoparticles

Carboxylated or PEGylated ( $M_w\text{PEG} = 300 \text{ g/mol}$ ) nanoparticles with nominal size of 50-70 nm made from “Yellow” or “Nile-Red” fluorochrome-labelled polystyrene were obtained from Spherotech Inc. (Lake Forest, IL, USA). Concentration of the stock suspensions was 10 mg/ml, fluorescence spectrum was provided by the manufacturer (Figure 9).

FITC-labelled 50-70 nm nanoparticles were purchased from Kisker Biotechnology GmbH (Steinfurt, Germany), with or without 600 Da or 2 kDa PEG chains on the NP surfaces.

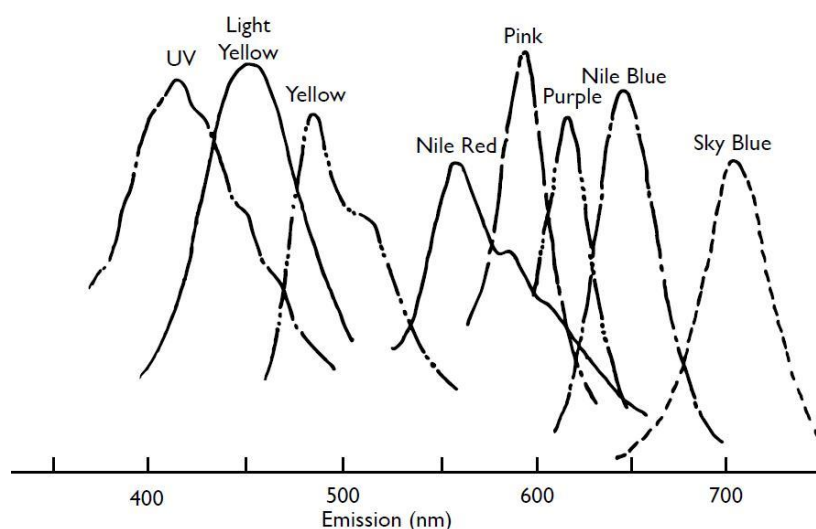


#### Figure 9: Fluorescence spectra of PS-NP

Fluorescence spectra of “Yellow” and “Nile-Red” PS-NP provided by the manufacturer, together with the spectra of other commercially available fluorescent nanoparticles (Spherotech).

#### 4.1.2. Silica nanoparticles

Fluorescent silica nanoparticles with a core-shell structure were synthesized, functionalized and characterized by Emilia Izak-Nau at Bayer Technology Services, GmbH, Germany (results summarized in (Izak-Nau et al. 2013a)). 50 nm SiO<sub>2</sub> nanoparticles encapsulating fluorescein-isothiocyanate (FITC,  $\geq 90\%$ , Fluka, Seelze, Germany) were synthesized with modified Stöber method (Stöber et al. 1968). The surface of NPs was either coated with polyvinylpyrrolidone (PVP K-15, Sigma-Aldrich,

Germany) or modified to generate amino and mercapto surface groups by addition of 3-aminopropyltriethoxysilane (APTES, 98 %, Alfa Aesar) and 3-mercaptopropyltrimethoxysilane (MPTMS, Sigma-Aldrich) organosilanes, respectively.

## **4.2. Physicochemical characterization of polystyrene nanoparticles**

### *4.2.1. Dynamic light scattering (DLS) measurements*

Size of nanoparticles was measured by dynamic light scattering with a ZetasizerNano ZS90 (Horiba Instruments Inc., Irvine, CA). Measurement was carried out at 25°C. Light beam was produced by using a 633 nm He-Ne laser, which was scattered by the nanoparticles in the measuring chamber.

Time dependent increase in particle diameter (indicator of nanoparticle aggregation) was monitored in inorganic or biological environments, including solutions used during particle handling and solutions that mimic the characteristics of body fluids. Carboxylated and PEGylated polystyrene nanoparticles (1 mg/ml in distilled water) were diluted 1:10 with PBS (pH 7.4), DMEM cell culture medium (Sigma-Aldrich, St. Louis, MO, USA) or DMEM supplemented with 10% fetal bovine serum (Invitrogen/Gibco, Carlsbad, CA, USA). After 0, 4, 24 or 96-hour incubation at 37°C, particle preparations were further diluted in 1:10 with distilled water and the hydrodynamic diameter of particles was measured by DLS.

Three samples were assayed in each condition ( $N_x = 3$ ) and each assay was repeated 3 times ( $\Sigma n_x = 9$ ). When initial size distribution of PS-COOH and PS-PEG particles was measured in distilled water, Kolmogorov-Smirnov normality test showed Gaussian distribution of experimental data ( $\Sigma n_{\text{COOH}} = 9$ ,  $\Sigma n_{\text{PEG}} = 9$ ). To compare the size distribution of PEGylated and COOH-nanoparticles unpaired t-test was used on the averaged data of repeated measurements ( $N_{\text{COOH}} = 3$ ,  $N_{\text{PEG}} = 3$ ) defined by mean, SD and the number of repeated measurements ( $n = 3$ ).

### *4.2.2. Transmission electron microscopy measurements*

Size and shape of nanoparticles were confirmed by transmission electron microscopy (TEM, JEOL JEM 1010, JEOL Ltd., Tokyo, Japan). For TEM analysis, 3  $\mu\text{l}$  aliquots of 0.01 mg/ml nanoparticle suspensions in distilled water were transferred to and dried on 200 mesh copper grids with carbon film. Microscope was operated at 80 keV accelerating voltage. Images were taken from representative fields of views.

#### 4.2.3. Zeta-potential measurements

Zeta-potential of nanoparticles was measured by ZetasizerNano ZS90 (Horiba Instruments Inc.). The technique is based on the measurement of the migration rate of dispersed particles in an electric field, providing the electrophoretic mobility of NPs as a result. The zeta-potential is calculated from the electrophoretic mobility by the software using the Henry equation. Measurements were carried out in distilled water on 3 parallels of 0.01 mg/ml nanoparticle suspensions ( $N_{\text{COOH}} = 3$ ;  $N_{\text{PEG}} = 3$ ) at 25°C with a folded capillary cell (DTS1070, Malvern Instruments, Worcestershire, United Kingdom). The measurements were repeated 3 times. Kolmogorov-Smirnov normality test showed Gaussian distribution of experimental data ( $\Sigma n_{\text{COOH}} = 9$ ,  $\Sigma n_{\text{PEG}} = 9$ ). To compare the zeta-potential of PEGylated and COOH-NPs unpaired t-test was used on the averaged data of repeated measurements ( $N_{\text{COOH}} = 3$ ,  $N_{\text{PEG}} = 3$ ) defined by mean, SD and number of repeated measurements ( $n = 3$ ).

#### 4.2.4. Assays on protein adsorption

Proteins adsorbed by particles in 10% fetal bovine serum containing minimum essential medium (FBS-MEM; Sigma-Aldrich, St. Louis, MO, USA) were analyzed by SDS-PAGE (Sodium dodecyl sulfate polyacrylamide gel electrophoresis). After 1 hour or 24-hour incubation in 10% FBS-MEM nanoparticles were sedimented by centrifugation (45min at 20000 x g) and were washed with PBS to remove non-bound proteins. Washed NPs were resuspended in Laemmli buffer containing 1% (w/v) sodium dodecyl sulfate, and loaded onto 10% polyacrylamide gel. Gel electrophoresis was performed at 130 V for about 60 min. The gels were stained with silver staining 33 kit (Cosmobio Ltd., Tokyo, Japan), according to the manufacturer's instructions.

### 4.3. Cell cultures

#### 4.3.1. Primary astroglial and neuronal cultures

Cell suspensions of primary brain cell cultures (Madarasz et al. 1984) were prepared by mechanical dissociation of embryonic (E14-19) mouse forebrains, or by combined enzymatic dissociation (Neural Tissue Dissociation Kit, Miltenyi Biotec) of early postnatal (P0-P3) mouse forebrains (Környei et al. 2000). Single cell suspension was obtained by filtering the dissociated suspension through a nylon mesh with pore diameter of 40  $\mu\text{m}$ . Cells were seeded onto cell culture plates containing poly-L-lysine (PLL,

Sigma-Aldrich) coated cover slips, in  $4 \times 10^5$  cells/cm<sup>2</sup> density. Primary cell cultures were maintained in 10% heat-inactivated FCS containing MEM, supplemented with 4mM glutamine, 2.5 µg/ml Amphotericin-B (Fungizone, Sigma) and 40 µg/ml gentamycin (Sanofi-Aventis/Chinoin) and kept in 5% CO<sub>2</sub> containing humidified air atmosphere, at 37°C. Medium was changed two times a week.

*Astroglia-enriched cultures* were prepared by changing the 10% serum containing medium on primary cultures every second day for two weeks.

*Neuron-enriched cultures* were prepared by treating primary cultures with the anti-mitotic 10 µM CAR (cytozin-arabino-furanozid, 10 µM), for 24hs, on the 4<sup>th</sup>-5<sup>th</sup> days after planting. Afterwards cultures were maintained in 10% horse serum (Bioser) containing MEM.

#### 4.3.2. Primary microglial cultures

Microglial cultures were prepared according to (Saura et al. 2003) from newborn mice. GFP-labelled microglia cells were isolated from mice expressing a green fluorescent protein under the control of CX3CR1 gene promoter (Jung et al. 2000).

First, mixed glial cultures were prepared from the forebrains of newborn (1–2 days old) mouse pups. The meninges were carefully removed and the brain tissue was incubated with 0.05% (w/v) trypsin solution supplemented with 1 mM EDTA. After 5 to 10 min incubation, the tissue was mechanically dissociated. Suspensions of single cells were seeded in 1:1 mixture of DMEM-F12 with 10% FCS and cultured at 37°C in 5% CO<sub>2</sub> containing humidified air atmosphere. Medium was replaced every 3–4 days.

After 10–12 days' cultivation, the confluent mixed glial cultures were trypsinized with 0.05% (w/v) trypsin in the presence of 0.2 mM EDTA and 0.5 mM Ca<sup>2+</sup>. After detachment of astrocytes, the firmly attached microglial cells were further propagated in 1:1 mixture of DMEM-F12 supplemented with 10% FCS.

#### 4.3.3. BV2 microglial cells

BV2 is a microglial cell line isolated from C57Bl mouse generated by infecting primary microglial cell cultures with a v-raf/v-myc oncogene carrying retrovirus (Blasi et al. 1990). BV2 cells retain most of the morphological, phenotypical and functional properties described for freshly isolated microglial cells. Namely BV2 cells are positive for MAC1

and MAC2 antigens, and negative for GFAP, MAC3 and galactocerebroside antigens (Blasi et al. 1990).

#### 4.3.4. NE-4C stem cells

NE-4C neuroectodermal stem cells (Schlett and Madarász 1997) were cloned from primary brain cell cultures prepared from the fore- and midbrain vesicles of 9-day-old transgenic mouse embryos lacking functional p53 tumor suppressor protein. NE-4C can be differentiated into neurons and astrocytes by retinoic acid induction. The retinoic acid induced neural differentiation of NE-4C cells is a highly reproducible process, where the differentiation steps follow each other in a strict order (Schlett et al. 1997, Varga et al. 2008, Hádinger et al. 2009, Madarász 2013) (Figure 10).

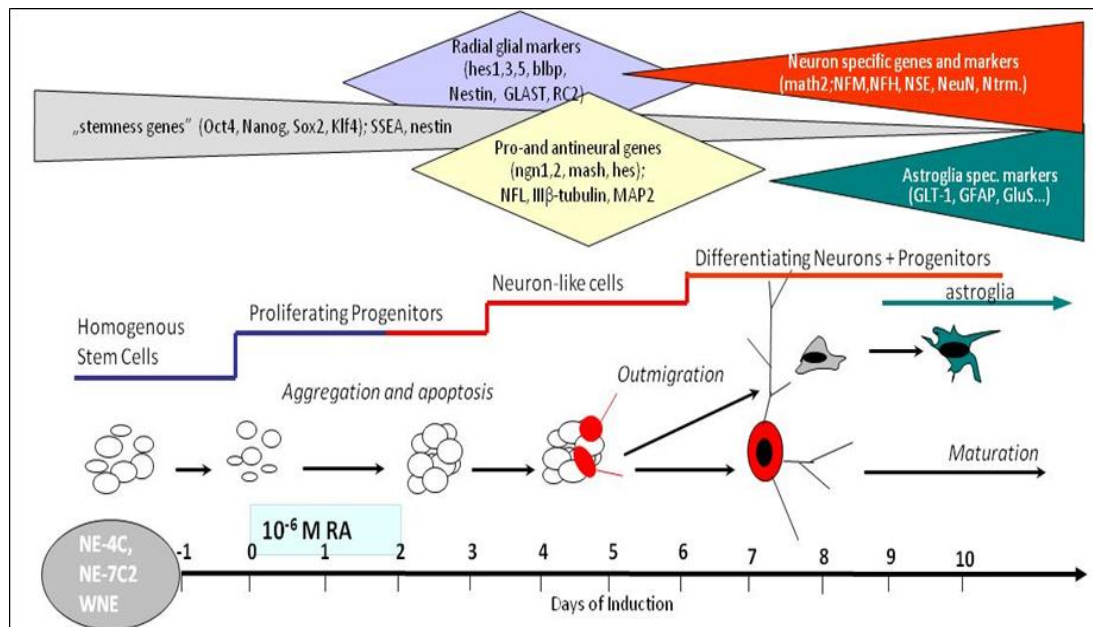


**Figure 10: The schematic representation of retinoic acid induced neural differentiation of NE-4C cells**

Neural differentiation is induced by a short RA-treatment, which at first initiates the aggregation of cells, and primes the differentiation process. Later, the differentiation proceeds in both serum-containing and serum-free culture conditions. Neuron specific markers are expressed from the 6-7<sup>th</sup> day after RA-treatment, glia genesis starts at 7-10 days after RA-priming. (Madarász 2013)

NE-4C neuroectodermal stem cells were maintained in poly-L-lysine (Sigma-Aldrich) coated culture dishes, in minimum essential medium (MEM; Sigma-Aldrich, Hungary) supplemented with 4 mM glutamine and 5% FCS (FCS; Sigma-Aldrich). Culture dishes were kept in 5% CO<sub>2</sub> containing humidified air atmosphere, at 37°C.

To induce differentiation  $10^{-6}$  M *all-trans* retinoic acid (RA; Sigma-Aldrich, Hungary) was added to confluent cultures of NE-4C cells for 48 hours. After 48-hour treatment with RA, the culture medium was changed to serum-free medium (1:1 mixture of MEM-F12 supplemented with 1 % ITS (Sigma-Aldrich)), and fresh media was given every second day during differentiation.

For mature neurons, identified by  $\beta$ III-tubulin positivity, cultures on the 7<sup>th</sup> to 9<sup>th</sup> days of induction were used. GFAP positive astroglia cells appear in the second week of induction, 5-7 days after the appearance of neuron-like cells.

#### 4.3.5. Radial glia

Cultures of adult radial glia-like cells (Markó et al. 2011) were established from hippocampi and subventricular zones of 21 day-old CD1 mice by enzymatic dissociation using the Neural Tissue Dissociation Kit (Miltenyi Biotec) according to the manufacturer's instructions. Dissociated cells were plated onto cell culture plates coated with AK-cyclo[RGDfC] (Markó 2008) and maintained in 1:1 mixture of MEM-F12 supplemented with 1% B27 supplement (Gibco) and 20 ng/ml EGF (Peprotech). The medium was changed every second day after rapid rinsing with PBS in order to wash off weakly adhering cells. After 3-4 passages, cultures the cultures contained virtually homogeneous populations of radial glia-like cells, which can proliferate continuously and display radial glia-specific markers (including nestin, RC2 immunoreactivity and Pax6, Sox2, Blbp, Glast gene expression).

Under appropriate inducing conditions, radial glia cells can differentiate into neurons, astrocytes or oligodendrocytes depending on the culture conditions (Markó et al. 2011).

#### 4.4. In vitro uptake of nanoparticles

For cellular uptake studies cell cultures were grow on poly-L-lysine coated glass coverslips in 24 well plates. The cells were incubated with nanoparticle suspension dispersed in 1:1 mixture of MEM:F12 supplemented with 1 % ITS (MEM-F12-ITS) or with 1% B27 (MEM-F12-B27) for 30min to 1 h at 4 °C or 37 °C in air with 5% CO<sub>2</sub>. Summary of treatment conditions are shown in Table 1. Control cultures were incubated under the same conditions, but without the addition of nanoparticles.

**Table 1: Nanoparticle concentrations used in uptake experiments**

Nanoparticle	Concentration	Volume	Solution
SiO <sub>2</sub>	5 x 10 <sup>11</sup> NPs/ml	500 µl	MEM-F12-ITS
SiO <sub>2</sub> -NH <sub>2</sub>	5 x 10 <sup>11</sup> NPs/ml	500 µl	MEM-F12-ITS
SiO <sub>2</sub> -SH	5 x 10 <sup>11</sup> NPs/ml	500 µl	MEM-F12-ITS
SiO <sub>2</sub> -PVP	5 x 10 <sup>11</sup> NPs/ml	500 µl	MEM-F12-ITS
PS-COOH	3.5 x 10 <sup>10</sup> NPs/ml to 2 x 10 <sup>11</sup> NPs/ml	500 µl	MEM-F12-ITS or MEM-F12-B27
PS-PEG	3.5 x 10 <sup>10</sup> NPs/ml to 2 x 10 <sup>11</sup> NPs/ml	500 µl	MEM-F12-ITS or MEM-F12-B27

After incubation, the samples were washed three times with phosphate buffered saline (PBS, pH 7.4) to remove free-floating NPs and fixed for 20 min with paraformaldehyde (PFA, 4% w/v) at room temperature.

#### 4.5. In vivo distribution of polystyrene nanoparticles

Animal experiments were conducted with the approval of the Animal Care Committee of the Institute of Experimental Medicine of Hungarian Academy of Sciences and according to the official license (No.: 22.1/353/3/2011) issued by National Food Chain Safety Office ([www.NEBIH.gov.hu](http://www.NEBIH.gov.hu)), Hungary.

Male mice (aged 25-30 days) and pregnant female mice on the 10th to 15th post conception days were anesthetized with a mixture of ketamine (CP-Pharma mbH, Burgdorf, Germany) and xylazine (CEVA-PHYLAXIA, Budapest, Hungary), 100 µg/g and 10 µg/g bodyweight, respectively. Stock suspensions (10 mg/ml) of polystyrene nanoparticles were diluted 1:30 in PBS and dispersed by sonication. Under proper anesthesia, 7 µl/g bodyweight aliquots of carboxylated or PEGylated nanoparticle suspensions were introduced into the tail vein. Animals were sacrificed by overdose of anesthetics after a 5-minute or 4-day exposure to the single-injection loading. Various organs including brain, liver, kidney, spleen as well as placenta and embryos were removed and fixed with paraformaldehyde (8 w/v% in PBS) for 24 hours at 4°C. Organs and embryos were collected from animals not exposed to nanoparticles, as controls.

#### 4.6. Microscopic evaluation

Cellular uptake of nanoparticles by cultured cells and *in vivo* penetration into various tissues were examined using Zeiss Axiovert 200M microscope (Carl Zeiss Microimaging,

Jena, Germany) and Nikon A1R Confocal Laser Microscope System (Nikon, Shinjuku, Tokyo, Japan) equipped with a spectral detector unit for fluorescence spectrum analysis. For microscopic evaluation, 30 or 60  $\mu\text{m}$  thick vibratome sections (VT1000S, Leica, Wetzlar, Germany) were made from fixed organs.

#### 4.6.1. Immunohistochemical procedures

For visualization of intracellular antigen epitopes, fixed cells or tissue sections were permeabilized with Triton X-100 (10 min, 0.1% v/v in PBS) and non-specific antibody binding was blocked by incubating the sections in PBS containing 10 % FBS for 2 hours. Primary antibodies were diluted in 1 to 1000 with PBS-FBS, and the preparations were incubated at 4°C, overnight. After incubation, the cells/sections were washed three times (15 min each) with PBS and incubated with alexa-594 conjugated secondary antibodies for 1 h. Cell cultures were occasionally stained with CellMask (Molecular Probes, Invitrogen, Carlsbad, CA, USA) according to the manufacturer's instructions, to visualize cell membranes. Detailed information on primary and secondary antibodies are shown in Table 2.

Preparations were mounted with mowiol (Sigma-Aldrich, Budapest, Hungary) containing 10  $\mu\text{g}/\text{ml}$  bisbenzimidazole (Sigma-Aldrich) for nuclear staining.

**Table 2: Antibodies used during immunocytochemical stainings**

<b>Primary antibodies</b>	<b>Dilution</b>	<b>Provider</b>
anti-Iba-1 (polyclonal goat)	1:1000	Abcam; Cambridge, UK
anti-claudin V (polyclonal rabbit)	1:1000	Abcam; Cambridge, UK
anti-GFAP (monoclonal mouse)	1:1000	Sigma-Aldrich, Budapest, Hungary
anti- $\beta$ -III tubulin (monoclonal mouse)	1:1000	Sigma-Aldrich, Budapest, Hungary
<b>Secondary antibodies</b>		
anti-goat alexa-594 conjugated AB	1:1000	Molecular Probes, Carlsbad, USA
anti-rabbit alexa-594 conjugated AB	1:1000	Molecular Probes, Carlsbad, USA
anti-mouse alexa-594 conjugated AB	1:1000	Csertex Kft., Budapest, Hungary

#### 4.6.2. Detection of particles by spectral imaging fluorescence microscopy

For enhanced detection of nanoparticles and identification of NP-derived fluorescence spectral imaging fluorescence microscopy was adapted. Fixed cells or tissue sections were examined using Nikon A1R Confocal Laser Microscope System (Nikon, Shinjuku, Tokyo, Japan) equipped with a spectral detector unit for spectral acquisition.

For spectral evaluation 457 nm argon ion laser was used as excitation source for “Yellow” PS-NP treated samples and the corresponding controls. The emitted light was detected by the spectral detector unit from 468 nm to 548 nm, with a spectral resolution of 2.5 nm. In order to record continuous spectrum, a 20/80 beam splitter (BS20/80) with continuous transmission was used instead of a paired dichronic mirror arrangement.

For the detection of other fluorophore labelled particles microscopic arrangement was similar, only the excitation and detection wavelengths were changed (Table 3).

**Table 3: Excitation wavelengths and detection ranges for nanoparticles core-labelled with different fluorochromes**

Fluorophore	Excitation wavelength	Detection range	Spectral resolution	SR (emitted light intensity ratio)
"Yellow"	457 nm	468-548 nm	2.5 nm	483/528 nm
"Nile Red"	514 nm	535-727 nm	6 nm	560/670 nm
FITC	488 nm	490-570 nm	2.5 nm	515/550 nm

*Post hoc* fluorescence spectrum analysis was carried out on selected spectral images. To establish positive and negative controls for the analysis, fluorescence spectra of NPs were determined in dry and in buffer-dispersed particle preparations, as well as in contact with fixed tissue sections made from control animals. The spectra emitted by the particles in contact with the corresponding tissue section from control animals were used as positive controls. For negative control, the intrinsic autofluorescence spectra of corresponding sections of control organs were used.

Regions of interest (ROIs) were delineated and analyzed in corresponding sections of nanoparticle-treated and non-treated organs. The photocurrent intensities detected at different wavelengths (emission spectra) in the sections of NP-treated animals were plotted against the tissue autofluorescence spectra (negative control) and the spectra of nanoparticles seeded on control-tissue (positive control).

To quantitatively classify NP-containing ROIs a spectral ratio (SR) was calculated from the fluorescence intensities at reference wavelengths corresponding to the intensity maximums of NP-fluorescence and tissue autofluorescence (Table 3). For samples containing “Yellow” labelled polystyrene NPs the SR was calculated by dividing the relative fluorescence intensities at 483nm and 528nm reference wavelengths. ROIs were considered as NP-containing if the spectral ratio was above 1 ( $SR > 1$ ).

## 5. RESULTS

### 5.1. Physicochemical characterization of nanoparticles

To compare the physicochemical characteristics of the differentially functionalized nanoparticles and to understand the differences in their interactions with the living material, thorough characterization of NPs was crucial. The physical and chemical parameters of particles were determined including hydrodynamic and dry size, aggregation properties, and protein adsorption. The changes of these parameters were monitored in distinct inorganic or biological environments, including solutions used during particle handling and solutions that mimic the characteristics of body fluids.

#### 5.1.1. *Polystyrene nanoparticles*

Polystyrene nanoparticles with carboxylated or PEGylated surfaces were used in the studies. The properties of these particles were analyzed in details and compared to each other.

Dynamic light scattering measurements revealed that the diameter of the two NPs did not differ significantly (Figure 11 A and B;  $70.81 \pm 21.09$  nm and  $68.69 \pm 18.68$  nm for PS-COOH and PS-PEG, respectively). The data showed that particles did not aggregate in distilled water. Transmission electron microscopic images showed slight agglomeration of dried particles and confirmed spherical shape of NPs (Figure 11 A and B inserts).

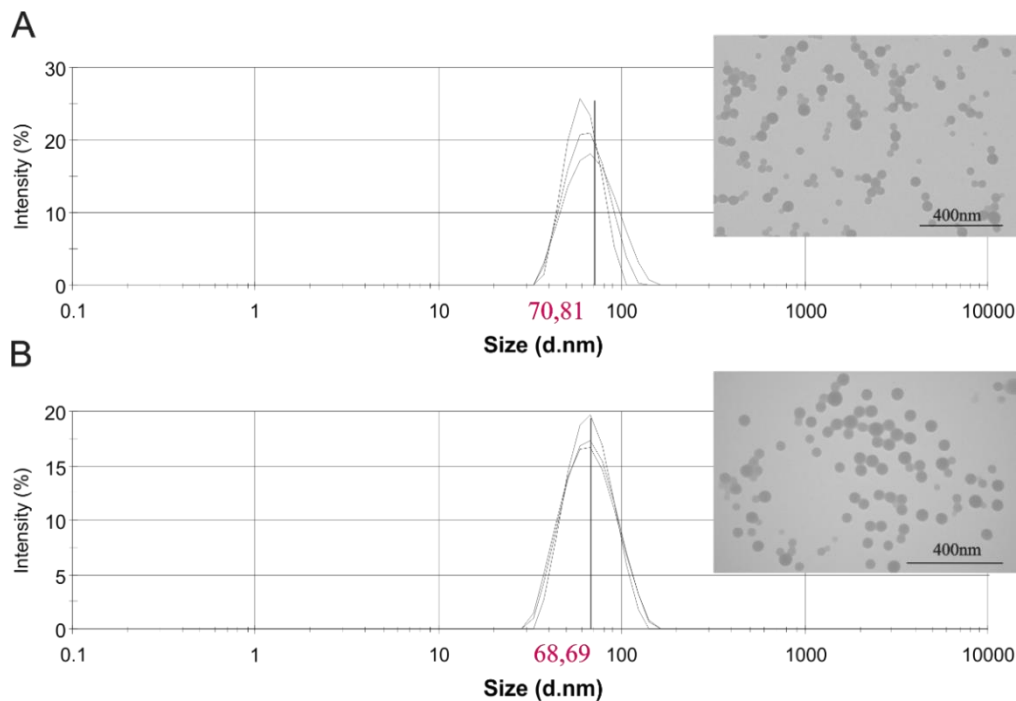


**Figure 11: Size distribution of PS-NP**

Intensity weighted size distribution of carboxylated (A;  $N_{\text{COOH}} = 3$ ) and PEGylated (B;  $N_{\text{PEG}} = 3$ ) polystyrene nanoparticles measured by dynamic light scattering in distilled water. Three repeated measurements were carried out on each sample. Average size of the NPs is marked with red. DLS measurements showed no significant difference between PS-COOH and PS-PEG NPs (unpaired t-test was carried out on the averaged data of repeated measurements ( $N = 3$ ,  $\Sigma n_x = 9$ ) defined by mean, SD and number of repeated measurements ( $n = 3$ ),  $p = 0.3622$ ). Representative transmission electron microscopic images of particles dried on copper grids are shown in the top right panels of each DLS plot. Scale bars represent 400 nm.

The zeta potential of particles measured in distilled water showed significant ( $p < 0.0001$ ; unpaired t-test) differences between the two NPs:  $-42.1 \pm 0.9$  mV for PS-COOH and  $-28.5 \pm 1.8$  mV for PS-PEG particles.

Based on the hydrodynamic particle size distributions, neither of the NPs did aggregate in distilled water or in PBS during a 96-hour assay period (Figure 12), indicating that the ionic strength of organic material-free physiological saline did not induce aggregation of PS-COOH and PS-PEG nanoparticles.

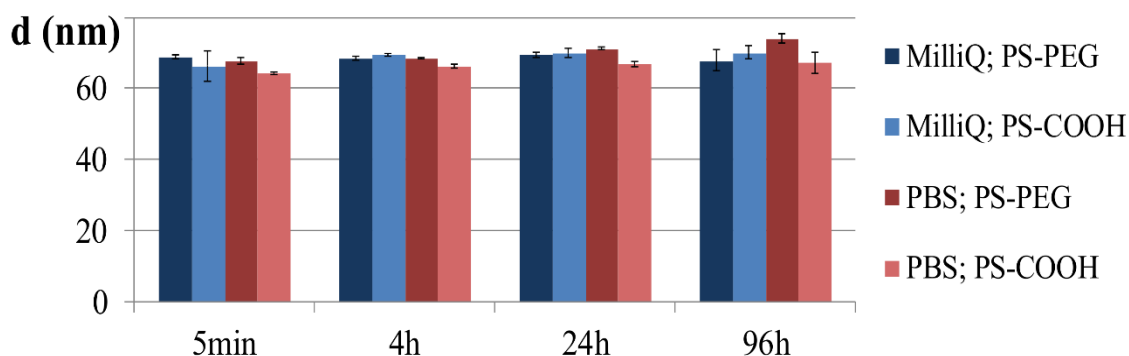


**Figure 12: Aggregation properties of PS-NP in inorganic solutions**

Particles were incubated in distilled water or PBS for 96 hours, while size distribution was monitored *via* DLS at certain time points. Data are presented as mean  $\pm$  standard deviation ( $N = 3$  in each group; three repeated measurements were carried out on the samples).

In contrast to inorganic solutions, a time-dependent, heavy aggregation of both NPs was found in serum-free DMEM (Table 4 and Figure 13). DMEM has an ionic strength similar to PBS, but contains various organic compounds including glucose, amino acids, vitamins and non-peptide hormones. In DMEM, a moderate increase in the hydrodynamic size was already observed after 4-hour incubation, and was found to be robustly elevated after 96 hours. The kinetics of particle enlargement was consistent with an immediate deposition of material on particle surfaces and a large-scale aggregation thereafter. The data showed that PEG-coating reduced the aggregation in long-term incubation (Figure 13).

**Table 4: Size distribution of PS-NP in DMEM**

Data are presented as mean  $\pm$  standard deviation ( $N_{\text{COOH}} = 3$ ,  $N_{\text{PEG}} = 3$ ).

	Size (nm)			
	5 min	4h	24h	96h
<b>PS-COOH</b>	66.40 $\pm$ 0.82	116.90 $\pm$ 2.10	178.47 $\pm$ 17.39	851.77 $\pm$ 34.27
<b>PS-PEG</b>	68.55 $\pm$ 0.45	115.93 $\pm$ 0,60	182.07 $\pm$ 30.53	559.67 $\pm$ 141.11

The incubation of nanoparticles with 10% fetal bovine serum containing DMEM evoked an immediate size increase, but prevented the large-scale aggregation of nanoparticles thereafter (Figure 13). The observation indicated that serum components were immediately adsorbed by particle surfaces, but instead of cross-linking particles, the protein corona could stabilize the suspension of dispersed particles.

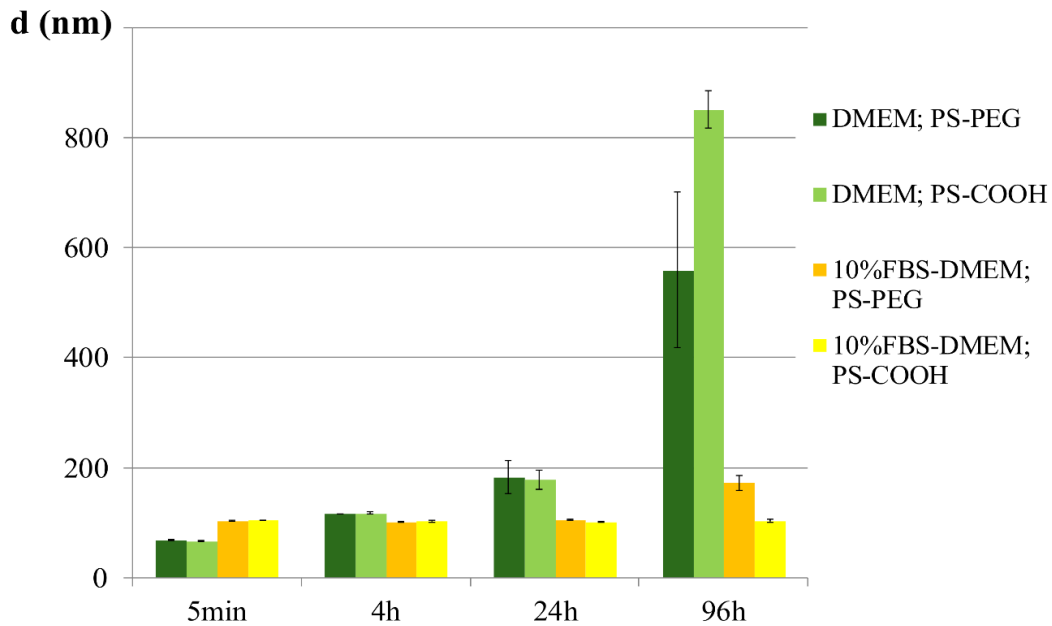


**Figure 13: Aggregation properties of PS-NP in organic solutions**

Particles were incubated in DMEM or DMEM supplemented with 10% FBS for 96 hours, while size distribution was monitored *via* DLS. Data are presented as mean  $\pm$  standard deviation ( $N = 3$  in each group; three repeated measurements were carried out on the samples).

Electrophoresis data further verified the rapid adsorption of proteins to both PS-COOH and PS-PEG nanoparticles (Figure 14A). PEG-coated nanoparticles exhibited reduced protein adsorption, which was evident after 24 hours incubation (Figure 14B) suggesting that PEGylation makes nanoparticles less prone to interactions with the environment.

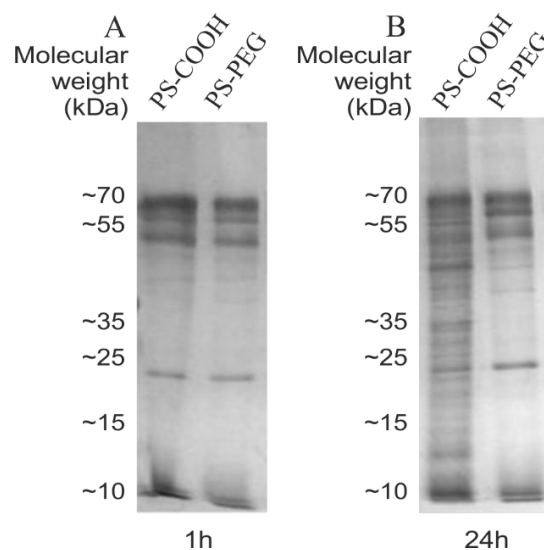


**Figure 14: Adsorption of serum proteins to polystyrene nanoparticles**

PS-COOH and PS-PEG particles were incubated for 1h or 24h in 10% FBS containing MEM and analyzed by SDS-PAGE.

### 5.1.2. Silica nanoparticles

50 nm spherical silica nanoparticles with a core-shell structure contained FITC encapsulated in the core. Surface of nanoparticles was coated either with PVP (SiO<sub>2</sub>-PVP), modified with amino (SiO<sub>2</sub>-NH<sub>2</sub>) or mercapto (SiO<sub>2</sub>-SH) functional groups, or left unmodified (SiO<sub>2</sub>-NP), generating four different types of SiO<sub>2</sub>-NPs, namely: SiO<sub>2</sub>-NP, SiO<sub>2</sub>-PVP, SiO<sub>2</sub>-NH<sub>2</sub>, SiO<sub>2</sub>-SH.

Synthesis, characterization and protein adsorption measurements of silica NPs was conducted by Emilia Izak-Nau and summarized in two publications (Izak-Nau et al. 2013a, 2013b). Here I present only briefly the basic properties of silica nanoparticles that are necessary to understand and interpret *in vitro* uptake results and to show the importance of the chemical surface composition in nano-bio interactions.

TEM and DLS measurements confirmed the size, spherical shape and monodispersity of the pristine silica particles (Figure 15) and the surface functionalized particles as well (Figure 16).

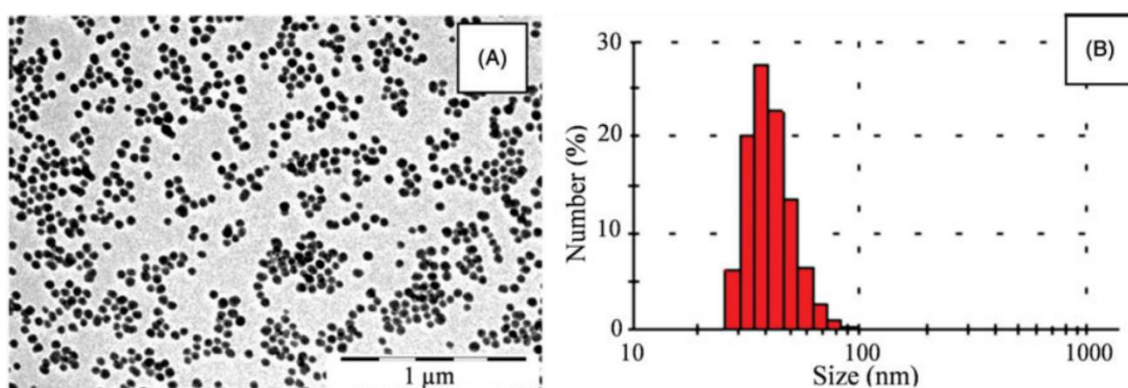


**Figure 15: Silica nanoparticles are spherical and monodisperse**

TEM (A) and DLS (B) measurements show spherical shape and monodispersity of pristine SiO<sub>2</sub>-NPs. Size measured by DLS was  $52.5 \pm 2.6$  nm (Izak-Nau et al. 2013a).

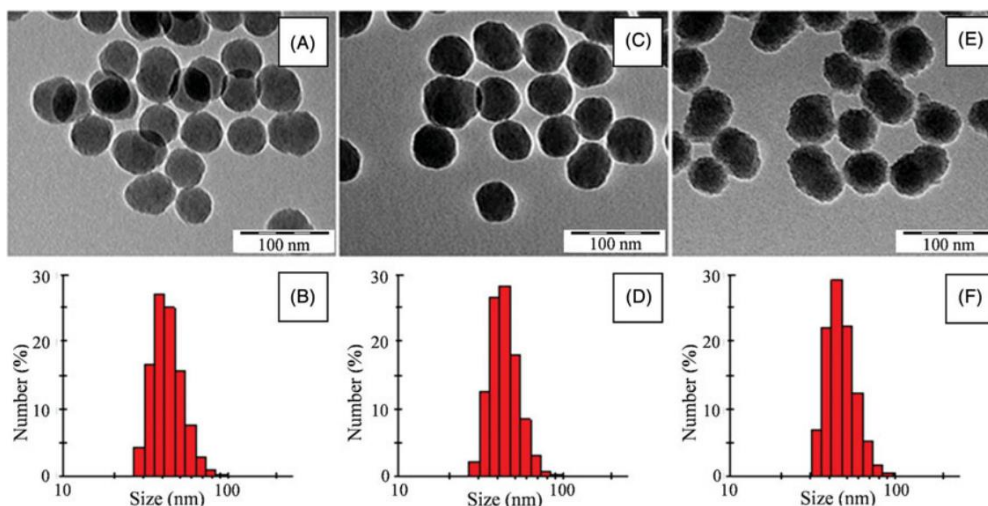


**Figure 16: Size and shape of surface functionalized SiO<sub>2</sub>-NPs**

TEM (A, C, E) and DLS (B, D, F) analyses of SiO<sub>2</sub>-NPs functionalized with amino groups (SiO<sub>2</sub>-NH<sub>2</sub>) (A, B), with mercapto groups (SiO<sub>2</sub>-SH) (C, D) or with polyvinylpyrrolidone (SiO<sub>2</sub>-PVP) (E, F) shows stability of NPs after functionalization (Izak-Nau et al. 2013a). Size measured by DLS:  $56.0 \pm 4.6$  nm for SiO<sub>2</sub>-NH<sub>2</sub>,  $49.9 \pm 2.2$  nm for SiO<sub>2</sub>-SH and  $59.5 \pm 2.3$  nm for SiO<sub>2</sub>-PVP.

The zeta potential of particles measured by DLS was  $-41.71 \pm 0.82$  mV for SiO<sub>2</sub>-NPs,  $+42.24 \pm 1.49$  for SiO<sub>2</sub>-NH<sub>2</sub>,  $-47.73 \pm 0.91$  mV for SiO<sub>2</sub>-SH and  $-40.87 \pm 1.31$  mV for SiO<sub>2</sub>-PVP (Izak-Nau et al. 2013a).

Aggregation properties and protein adsorption of silica nanoparticles was investigated with DLS and SDS-PAGE after incubation with fetal calf serum. All particles, with the exception of the PVP-coated particles, showed aggregation in cell culture media (Table 5). Additionally, PVP-coating markedly reduced the adsorption of serum proteins to the surface of silica NPs (Figure 17).

**Table 5: Size distribution of silica NP in cell culture media analyzed by DLS**

	Size (nm)			
	SiO <sub>2</sub>	SiO <sub>2</sub> -NH <sub>2</sub>	SiO <sub>2</sub> -SH	SiO <sub>2</sub> -PVP
<b>MEM</b> (48h; RT; $1 \times 10^{14}$ NPs/ml)	$1626 \pm 260$	$1892 \pm 423$	$1844 \pm 818$	$67 \pm 4$
<b>MEM-sonication 10 min</b> (48h; RT; $1 \times 10^{14}$ NPs/ml)	$785 \pm 156$	$873 \pm 199$	$932 \pm 176$	$65 \pm 3$
<b>MEM-F12-ITS</b> (1h; 37°C; $5 \times 10^{11}$ NPs/ml)	$1119 \pm 62$	$976 \pm 163$	$1247 \pm 137$	$68 \pm 6$

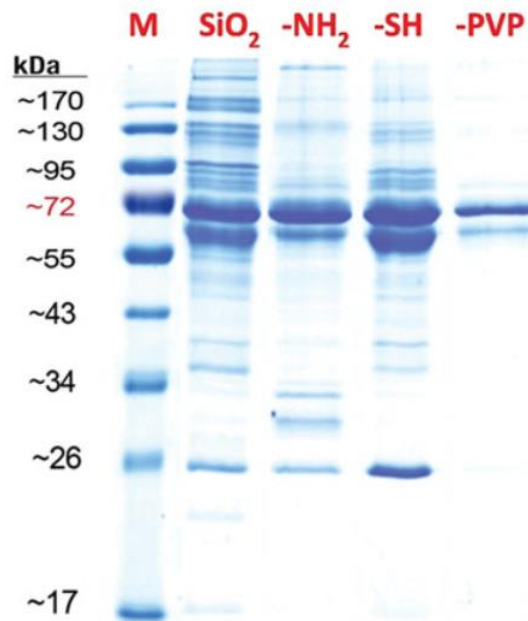


**Figure 17: Adsorption of serum proteins on silica NP**  
 SDS-PAGE analysis of silica nanoparticles after 1-hour incubation in 10% FCS containing PBS. M: molecular weight marker (Izak-Nau et al. 2013a).

Physicochemical characterization revealed that both polystyrene and silica nanoparticles gave stable, monodisperse suspensions in storage conditions. Surface functionalization resulted in different surface charges, but did not affect the dispersion stability in inorganic solutions. In contrast, particles were prone to aggregation in organic solutions, a phenomenon, which was reduced by PEGylation or PVP-coating.

## 5.2. In vitro cellular uptake of nanoparticles

### 5.2.1. Interaction of PS-NPs with neural stem- and tissue-type cells

To obtain information on the differential uptake of polystyrene nanoparticles primary cultures, containing mixed neural and glial cell populations were exposed to carboxylated and PEGylated particles.

In general, incubation with  $3.5 \times 10^{10}$  NPs/ml to  $2 \times 10^{11}$  NPs/ml polystyrene nanoparticles (diameter: 50-90nm) in serum free conditions did not result in obvious structural damage to cells after 1-hour incubation. In serum free media PS-COOH formed light microscopically detectable agglomerates. Within a 1 h exposure time, the agglomerates settled on cell surfaces and on the glass coverslip, and remained visible after multiple washing. PEGylated NPs, on the other hand, could wash off and were hardly visible outside of the cells.

When primary brain cell cultures containing neurons, astrocytes and microglia cells were exposed to PS-COOH nanoparticles, cells with microglial morphology accumulated a remarkable amount of NPs. GFAP positive astrocytes and neurons, identified by  $\beta$ III-tubulin positivity, were devoid of carboxylated particles (Figure 18).

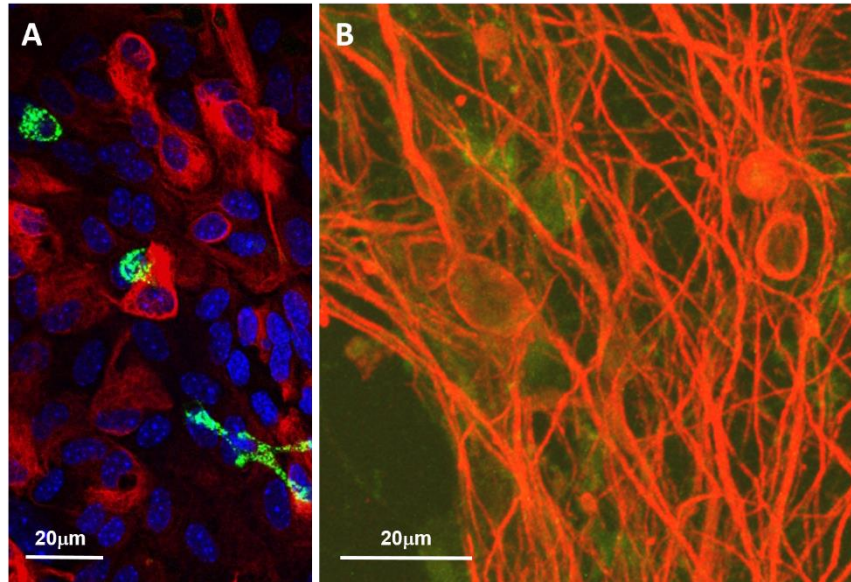


**Figure 18: GFAP and  $\beta$ III-tubulin negative cells with microglial morphology take up PS-COOH in primary forebrain cultures**

Primary mouse forebrain cultures, prepared from E17 embryos, were maintained for 14 days in glial-enriched culture (A) or in neuron-enriched culture for 6 days (B), were exposed to “yellow” fluorophore labelled PS-COOH nanoparticles (green) in serum free conditions for 1 h. Astrocytes were identified by GFAP staining (A, red) or neurons were visualized by  $\beta$ III-tubulin immunostaining (B, red) and cell nuclei by bisbenzimidazole nuclear staining (blue on A). (Murali et al. 2015)

To investigate whether the accumulated particles were internalized through active cellular processes, uptake experiments were run at +4°C and 37°C on primary cultures. In cell cultures incubated at +4°C, cells “labelled” by particles displayed markedly different morphology compared to 37°C-incubated ones (Figure 19).

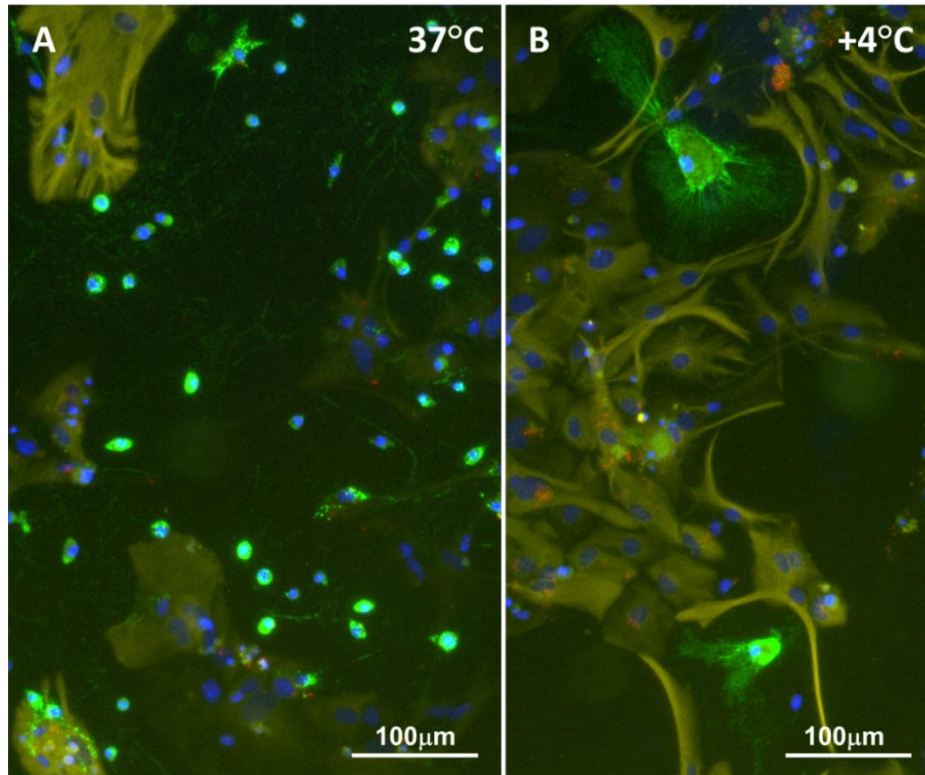


**Figure 19: Uptake of PS-COOH is activity dependent**

Mixed glial culture (from E18 mouse forebrain, 21 days after planting) was exposed to  $3.5 \times 10^{10}$  NPs/ml carboxylated polystyrene NP at 37°C (A) or +4°C (B). Cells with microglial morphology (small rounded cells in A) no longer took up particles when incubated at 4°C. Green: PS-COOH; yellow: GFAP, blue: nuclear staining.

Additionally, confocal microscopic z-stack analysis showed that at low temperatures NPs did not accumulate inside the cells, but were only attached to cell surfaces (Figure 20).

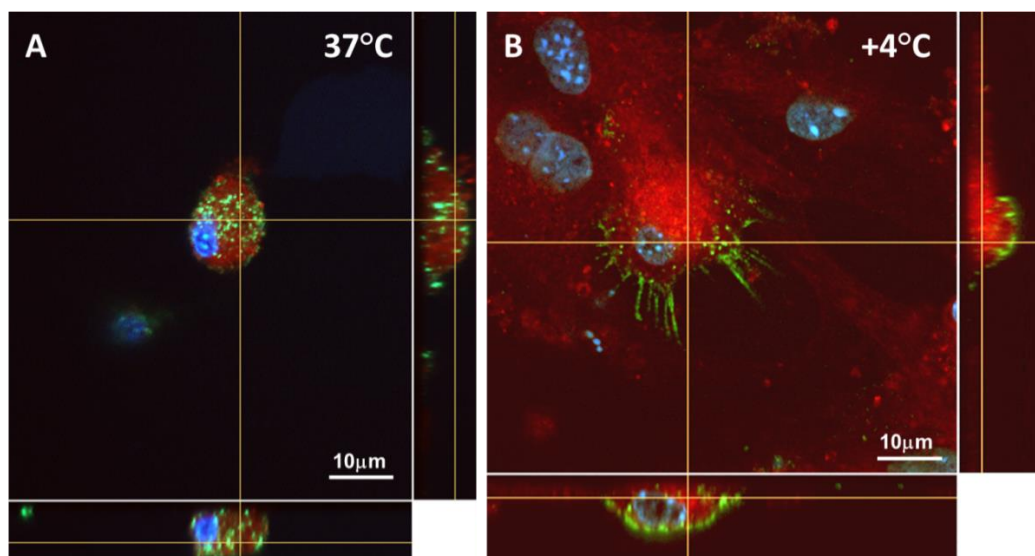


**Figure 20: Nanoparticles do not accumulate inside the cells at low temperatures**

Primary brain culture exposed to PS-NP from E15 mouse 21 days after isolation. Z-stack images show cellular uptake at 37°C (A), but only surface attachment at 4°C (B). Cell membranes were visualized with CellMask lipid staining (red). Particle fluorescence (green), nuclear staining (blue). (Experiments carried out with Kornél Demeter)

The uptake of polystyrene particles by microglia was further investigated in BV2 cells (Blasi et al. 1990) and in purified microglia cultures of GFP-labelled microglia cells expressing a green fluorescent protein under the control of fractalkine receptor 1 (CX3CR1) gene promoter (Jung et al. 2000). In 30 min exposure experiments (at 37°C) BV2 microglia cells internalized significant amount of carboxylated polystyrene nanoparticles, but were only sporadically labelled by PEG-functionalized particles (Figure 21).

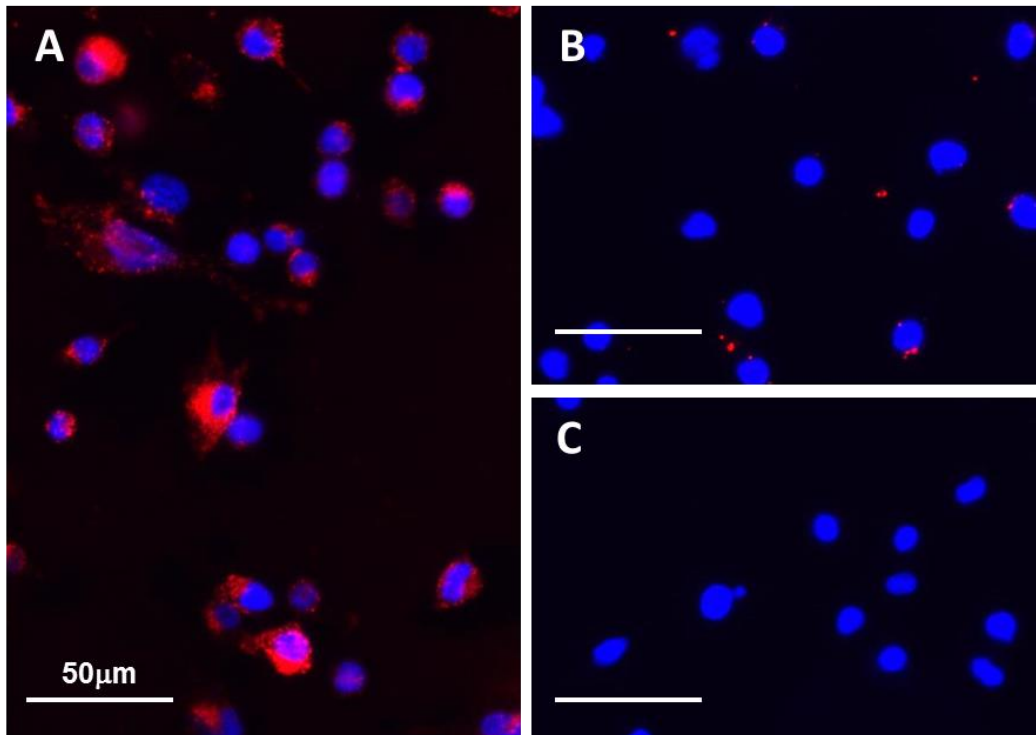


**Figure 21: BV2 cells after 30min exposure to PS-NP**

BV2 cells exposed to “nile-red”-labelled PS-COOH (A) or PS-PEG (B) nanoparticles (red) for 30 minutes in serum free conditions. Non-treated control culture (C). Cultures were stained with bisbenzimidazole nuclear staining (blue).

Similarly to BV2 cells, CX3CR1 GFP-labelled microglia cells accumulated remarkable amount of carboxylated particles, while did not take up PEGylated nanoparticles (Figure 22). Confocal microscopic video images during 1h exposures of GFP-labelled CX3CR1 microglia cultures (green) to “nile-red” PS-COOH (red) nanoparticles

([https://www.dropbox.com/s/bo4h8ibokxkgua5/in\\_vitro\\_PSNP\\_uptake\\_by\\_microglia\\_1.avi?dl=0](https://www.dropbox.com/s/bo4h8ibokxkgua5/in_vitro_PSNP_uptake_by_microglia_1.avi?dl=0) and [https://www.dropbox.com/s/1riwi4bqhd44a52/in\\_vitro\\_PSNP\\_uptake\\_by\\_microglia\\_2.avi?dl=0](https://www.dropbox.com/s/1riwi4bqhd44a52/in_vitro_PSNP_uptake_by_microglia_2.avi?dl=0))

showed that projections took up remarkably high amount of carboxylated particles during exposure, which were transferred towards the soma afterwards.

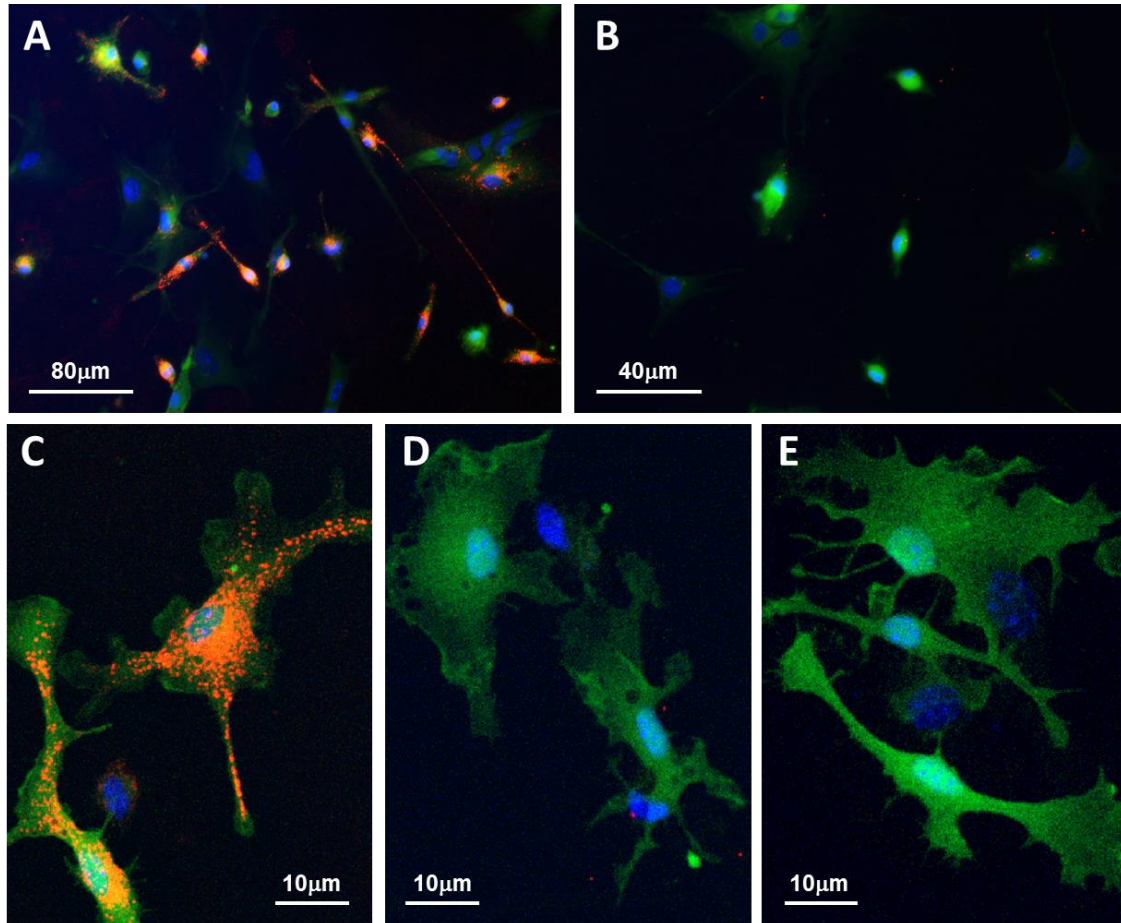


### Figure 22: Primary microglia cells take up carboxylated NPs

GFP-labelled microglia cells expressing a green fluorescent protein under the control of CX3CR1 gene promoter were treated with “nile red”-labelled (red) PS-COOH (A, C) or PS-PEG (B, D) nanoparticles for 30min. Red: particle fluorescence, green: GFP, blue: bisbenzimidazole nuclear staining. Non-treated control culture is shown in E.

Primary cultures, regardless of the majority of neural or glial populations, always contain a number of non-differentiated, progenitor type cells. We investigated the nanoparticle uptake of progenitor cells on NE-4C neuroectodermal stem cells (Schlett and Madarász 1997) and purified of radial glia cells (Markó et al. 2011). Progenitor cells did not take up polystyrene NPs, when incubated with  $3.5 \times 10^{10}$  NPs/ml suspensions for 1 hour (Figure 23).

We could conclude, that microglia cells are the primary collectors of PS-COOH NPs in mixed neural cultures. The almost complete lack of particles inside the cells after particle-loading at low temperature indicate that the uptake is an active, energy-dependent process. The uptake of PS-NPs was effectively inhibited by PEGylation of the particle surfaces.

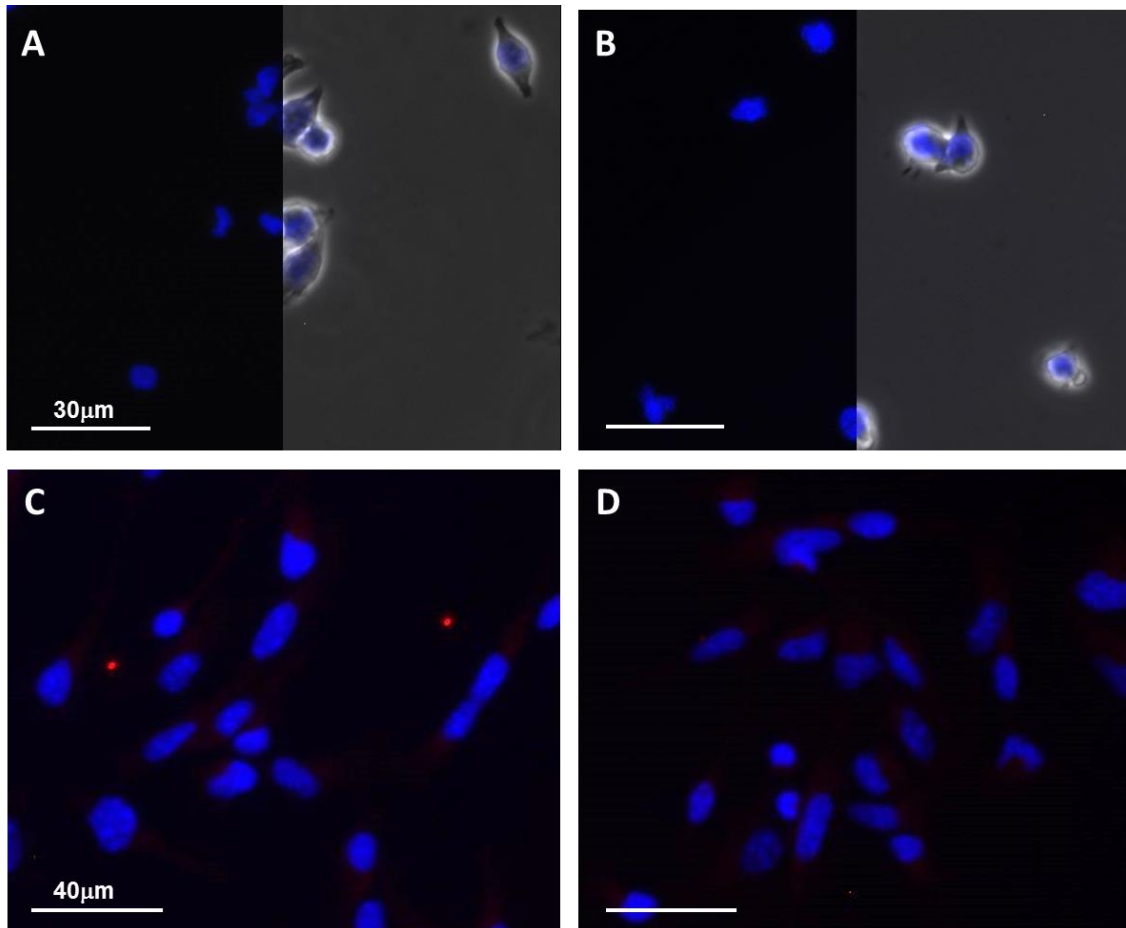


**Figure 23: Progenitor cells do not take up polystyrene nanoparticles**

Cloned embryonic neuroectodermal NE-4C stem cells (A, B) and radial glia cells (C, D) after 30-minute exposure to polystyrene NP. Cultures were treated with  $3.5 \times 10^{10}$  NPs/ml PS-COOH (A, C) or PS-PEG (B, D) NPs. Particle fluorescence is shown in red; cell nuclei are marked with blue nuclear staining. Half of the image in A and B is showing merged phase contrast and blue-fluorescence image of the same field.

### 5.2.2. Interaction of Si-NP with neural stem- and tissue-type cells

Uptake of fluorescently labelled core/shell SiO<sub>2</sub> NPs with 50nm size was investigated on various cell types. In general, incubation with silica nanoparticles in serum free conditions did not cause structural damage to the investigated cells. After 1-hour incubation with

500  $\mu\text{l}$  of  $5 \times 10^{11}$  NPs/ml nanoparticles the morphology of cells was similar to control conditions.

Plain  $\text{SiO}_2$ -NPs and amino- or mercapto-modified silica nanoparticles ( $\text{SiO}_2\text{-NH}_2$  and  $\text{SiO}_2\text{-SH}$ ) formed light microscopically detectable agglomerates. Within 1 h exposure, the agglomerates settled on both the cell surfaces and the glass substrate, and were not removed by multiple washing. In clear contrast, PVP-functionalized silica particles did not form agglomerates and/or were washed off from the surfaces.

In mixed glial cultures, plain  $\text{SiO}_2$ ,  $\text{SiO}_2\text{-NH}_2$  and  $\text{SiO}_2\text{-SH}$  nanoparticles were seen in aggregates on the cell-free substrate, on astrocytes and more abundantly, in GFAP-negative (supposedly microglia) cells (see white arrow in Figure 24A). PVP-functionalized silica particles, on the other hand, were not taken up by glial cells and washed off from the substrate and cellular surfaces more easily compared to the other types of  $\text{SiO}_2$ -NP (Figure 24).

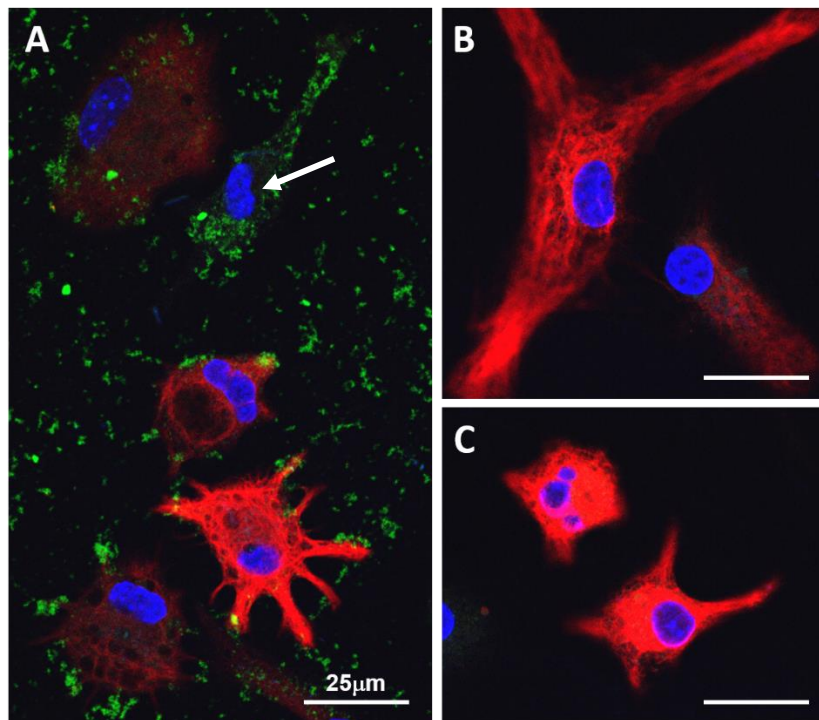


**Figure 24: Cultures of mouse forebrain glial cells exposed to silica NPs**  
Confocal images of forebrain glial cultures non treated (B) or treated with  $\text{SiO}_2$  (A) or  $\text{SiO}_2$ -PVP NPs (C). After 1 h exposure,  $\text{SiO}_2$  NPs adsorb onto astrocyte surfaces and to the culture surface, while  $\text{SiO}_2$ -PVP are easily washed out. Red: astrocytes stained for GFAP; blue: cell nuclei stained with bisbenzimidide; green: fluorescent  $\text{SiO}_2$  NPs.

Tree-dimensional reconstruction of a GFAP positive astrocyte from serial confocal images confirmed that SiO<sub>2</sub>-NPs were deposited on the cell surface, but were not engulfed by the cell (Figure 25).

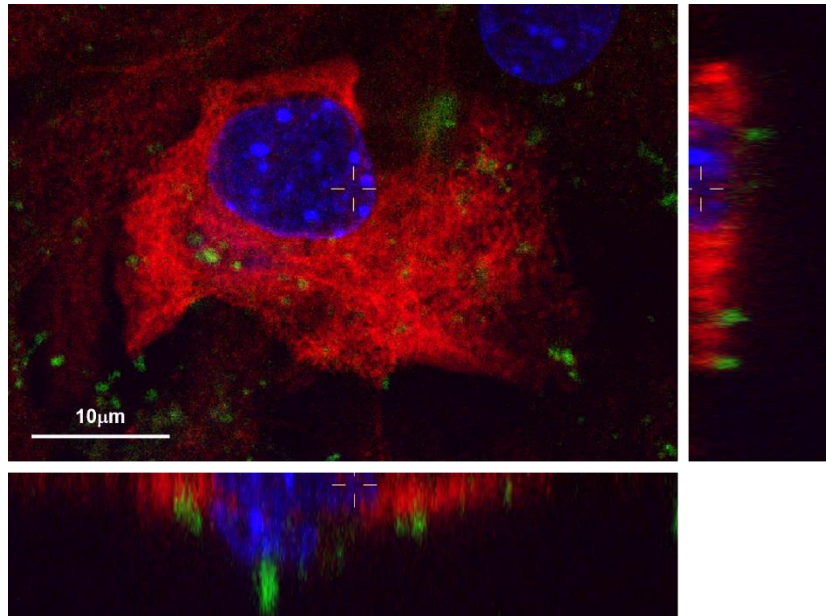


**Figure 25: Z-stack confocal image of SiO<sub>2</sub>-treated astrocyte**

GFAP positive astrocyte shows surface attachment of nanoparticles, indicating that SiO<sub>2</sub> NPs were not internalized by astrocytes. Yellow cross in the confocal image marks the pane of z-stack cross section for side views. Red: astrocytes stained for GFAP; blue: cell nuclei; green: fluorescent SiO<sub>2</sub> NPs.

Primary brain cultures enriched in neurons showed no neuronal uptake of any type of silica particles. After 1-hour exposure a few agglomerates were found on cellular surfaces. Confocal z-stack images confirmed the surface attachment and external localization of these agglomerates (Figure 26).

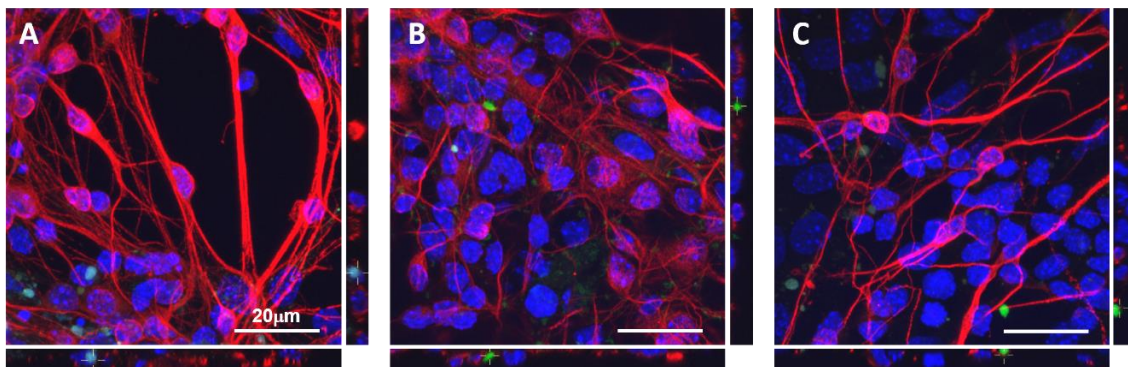


**Figure 26: Cultured embryonic mouse forebrain neurons exposed to silica NPs**

Confocal images of primary cultures enriched in neurons non-treated (A) or treated with pristine SiO<sub>2</sub> (B) or SiO<sub>2</sub>-PVP nanoparticles (C). After 1 h exposure, neurons did not

internalize any of the nanoparticles. Red: neurons stained for  $\beta$ III-tubulin; blue: cell nuclei stained with bisbenzimidazole; green: fluorescent NPs.

Plain  $\text{SiO}_2$  nanoparticles,  $\text{SiO}_2\text{-NH}_2$  and  $\text{SiO}_2\text{-SH}$  particles attached to microglia cells, while no interaction was detected with  $\text{SiO}_2\text{-PVP}$  NPs (Figure 27). On a few occasions, highly fluorescent aggregates were seen intracellularly, however, the high autofluorescence of microglia cells, prevented us to draw further conclusions. The location of nanoparticles could not be identified precisely with conventional confocal techniques, since the autofluorescence of cells masked the particle fluorescence.

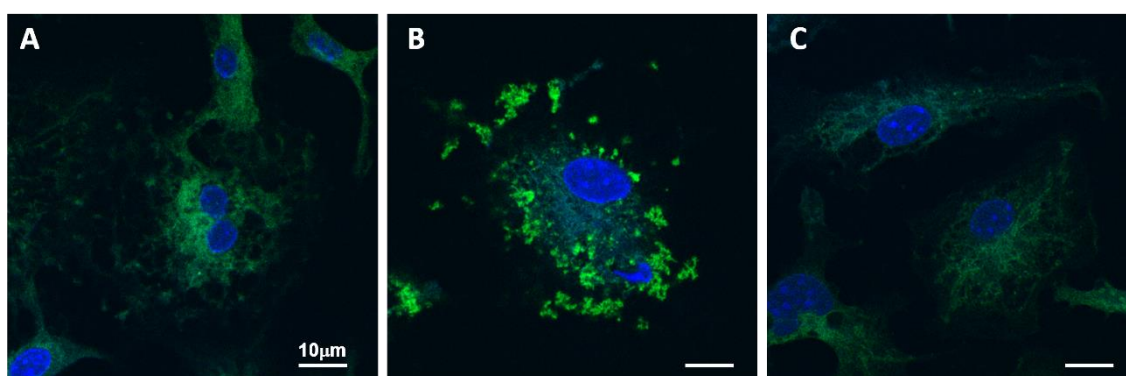


**Figure 27: Interaction of  $\text{SiO}_2$  nanoparticles with microglia**

Purified cultures of microglia cells (A) strongly interact with plain  $\text{SiO}_2$  nanoparticles (B), while almost no interaction was detected with  $\text{SiO}_2\text{-PVP}$  NPs (C). Cell cultures (in B and C) were exposed to silica NPs for 1-hour, in serum free conditions. Green: fluorescent NP; blue: bisbenzimidazole nuclear staining.

Interaction of silica particles with progenitor cells was investigated on cultures of NE-4C neural stem cells. Particles were detected on the surface of NE-4C cells in cultures treated with  $\text{SiO}_2$ ,  $\text{SiO}_2\text{-NH}_2$  and  $\text{SiO}_2\text{-SH}$  particles, while no interaction was detected with  $\text{SiO}_2\text{-PVP}$  NPs (Figure 28).

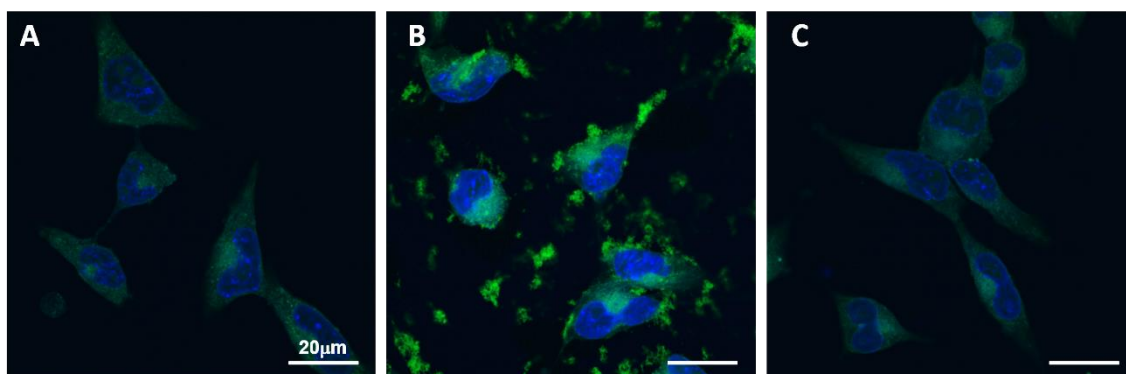


**Figure 28: Interaction of  $\text{SiO}_2$  nanoparticles with NE-4C neural stem cells**

NE-4C stem cells (A: non-treated) strongly interact with plain SiO<sub>2</sub> nanoparticles (B), while almost no interaction was detected with SiO<sub>2</sub>-PVP NPs (C). Cell cultures (in B and C) were exposed to silica NPs for 1-hour, in serum free conditions. Green: fluorescent NP; blue: bisbenzimidazole nuclear staining.

The *in vitro* cellular uptake experiments demonstrated that neurons, astrocytes and progenitor cells did not take up polystyrene or silica nanoparticles, although surface attachment of silica particles was visible on several occasions.

The chemical composition of the surface of otherwise identical NPs importantly modified the biological interactions of particles. Regardless of the particle's core material, "passivating" the particle surfaces with chemically inert polymers, like PEG or PVP, could significantly reduce the aggregation and cellular accumulation of particles.

Among neural tissue-type cells, NPs were taken up readily by microglia cells known as the phagocytes of the brain. Experiments run at 37°C and 4°C demonstrated that nanoparticles did not accumulate inside cells at low temperatures indicating that particles were internalized through activity dependent cellular processes.

While several conclusions could be drawn from fluorescence microscopic studies and confocal Z-stack analyses, the high cellular autofluorescence, together with the relatively weak particle fluorescence called for some more sensitive and more reliable detection method.

### **5.3. Optimization of NP-detection by spectral imaging fluorescence microscopy**

Fluorescence microscopy is generally the method-of-choice in biomedical studies to localize specific biologically-relevant fluorescent materials, including nanoparticles (Bouccara et al. 2015). However, visualization of fluorescent NPs even with high-resolution confocal microscopy has been notoriously difficult, because of their size (typically being between 1 and 100 nm) is below Abbe's diffraction limit of ~ 250 nm. Moreover, the detection of fluorescent NPs is further hindered by the high autofluorescence intensity of biological samples (Bouccara et al. 2015), which does not allow visualization of individual particles or even small aggregates due to the low signal-to-noise ratio.

One of the objectives of my dissertation was to develop an imaging technique to study the tissue- and cell-type-specific distribution of fluorescent nanoparticles. To overcome the limitations caused by low NP fluorescence intensity and high tissue autofluorescence,

spectral imaging fluorescence microscopy was adapted. The basis of this technique is that the emitted light is detected separately on each wavelength throughout a defined spectrum range by using a multidetector array confocal arrangement. This acquisition approach combined with *post hoc* spectrum analysis allowed selective visualization and identification of nanoparticles in various cell cultures and tissue samples.

### 5.3.1. Optimization of imaging

Several excitation and detection wavelength combinations were probed, in order to find the optimal ranges for spectral identification of fluorochrome labelled nanoparticles. The highest signal-to-noise ratio for “yellow” particles was achieved by illuminating the sample at 457 nm excitation wavelength (Figure 29) and detecting the emitted light through a wavelength-range from 468 nm to 548 nm, with a spectral resolution of 2.5 nm. Optimal instrument settings for particles labelled with different fluorophores are shown in Table 3.

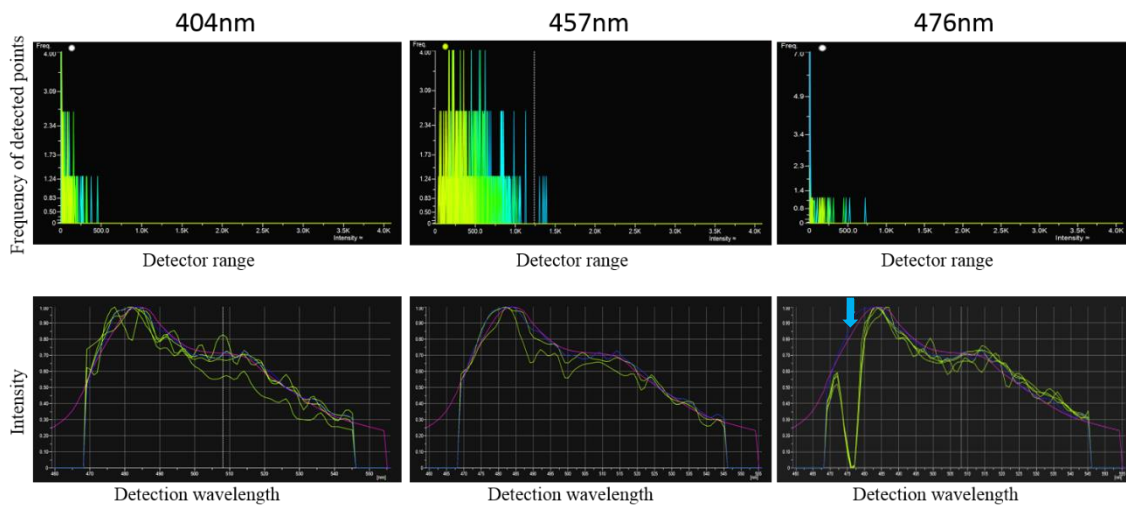


**Figure 29: Optimization of imaging**

Frequency of detected points (top row) and spectrum profiles (bottom row) of the same sample after excitation of “Yellow” NPs with 404nm, 457nm and 476nm laser lights. Detection wavelength ranged from 468 nm to 548 nm, spectral resolution: 2.5nm. Highest frequency of detected light points was reached when samples were excited at 457nm. 404nm excitation has lower signal-to-noise ratio compared to the 457nm excitation, and has the disadvantage of exciting nuclear staining (DAPI) of cells. 476nm excitation provides low signal-to-noise ratio, while it intermits with the detected spectra. This intermittence is due to the shielding of the detector from the laser light, which is marked with a blue arrow on the spectrum profile.

### 5.3.2. Spectra of nanoparticles used in experiments are stable

With the optimized imaging settings, the fluorescence spectra of nanoparticles were investigated in various environments including PBS; PBS complemented with 1% bovine serum albumin; mounting medium (Mowiol); and within fixed tissue slices. The measured spectra of polystyrene nanoparticles showed parity with the spectrum provided by the manufacturer and did not vary substantially under different conditions (Figure 30).

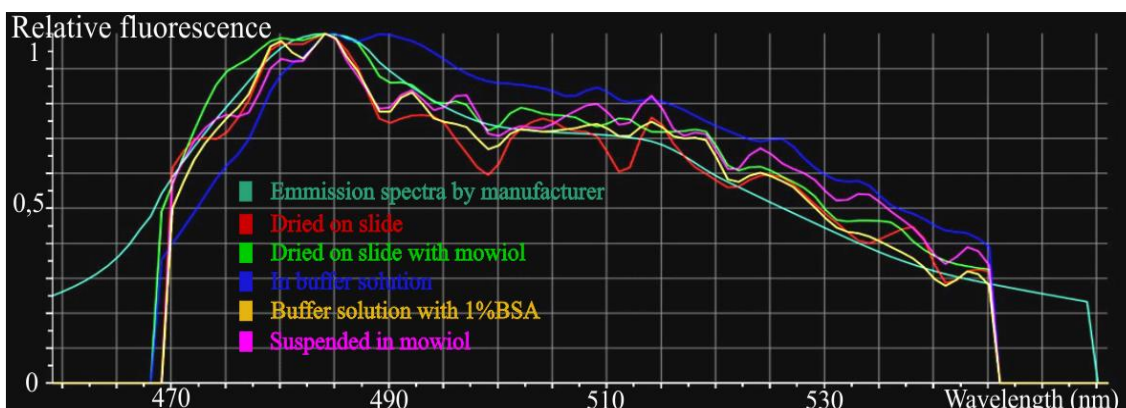


**Figure 30: Spectra of “yellow” PS-NPs measured by spectral imaging fluorescence microscopy are stable in various environments**

Relative fluorescence intensity values are plotted throughout the detected spectrum range from 468 nm to 548 nm. NP-spectra in different conditions matches the reference emission spectrum provided by the manufacturer (aquamarine spectrum).

Furthermore, particles with different surface compositions displayed identical fluorescence spectra, indicating that the functionalization had no direct effect on the NP fluorescence (Figure 31, Figure 32).

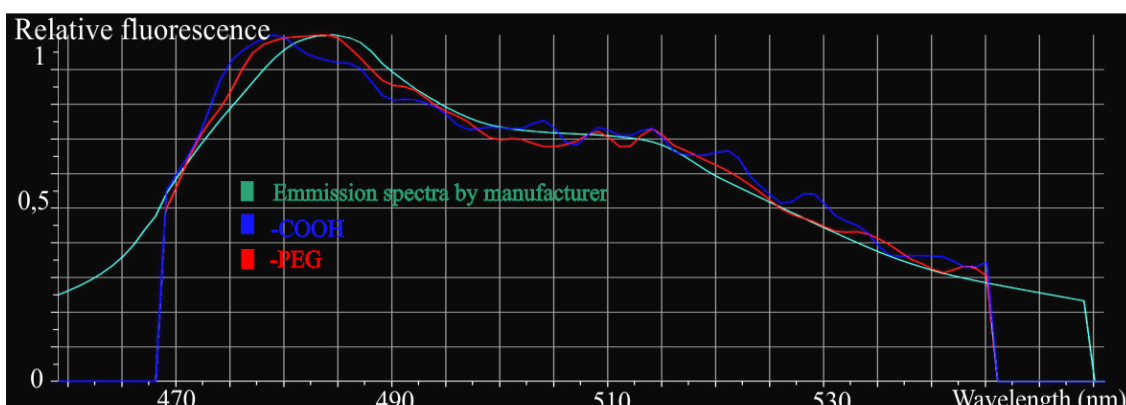


**Figure 31: Spectra of “yellow” PS-NPs after functionalization**

Spectra of PS-COOH and PS-PEG was analyzed by spectral imaging fluorescence microscopy. Fluorescence intensities were plotted against and showed similarity to the reference emission spectrum provided by the manufacturer (aquamarine spectrum).

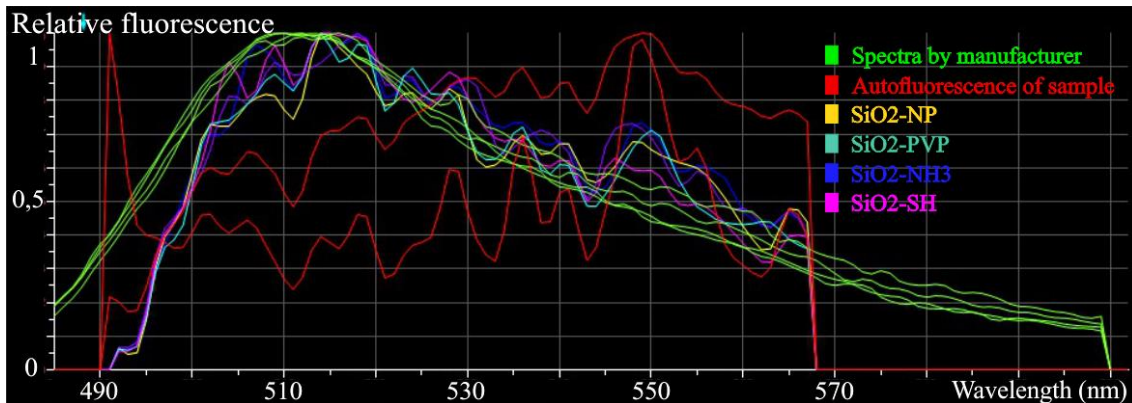


**Figure 32: Spectra of silica nanoparticles**

Spectra of bare SiO<sub>2</sub>-NP, SiO<sub>2</sub>-PVP, SiO<sub>2</sub>-NH<sub>3</sub> and SiO<sub>2</sub>-SH was analyzed by spectral imaging fluorescence microscopy. Fluorescence intensities were plotted against and showed similarity to the reference emission spectrum provided by the manufacturer (green spectra). Red: autofluorescence of sample.

For spectral analysis, an untreated (nanoparticle free) sample was used as negative control. Control spectra for each organ are shown in Figure 33, control spectra of cell cultures were determined similarly.

Positive controls were also used throughout the study in order to identify nanoparticle derived fluorescence. For this reason, nanoparticles were seeded on control tissue sections, the fluorescence was determined and used as positive controls together with the spectra provided by the manufacturer.

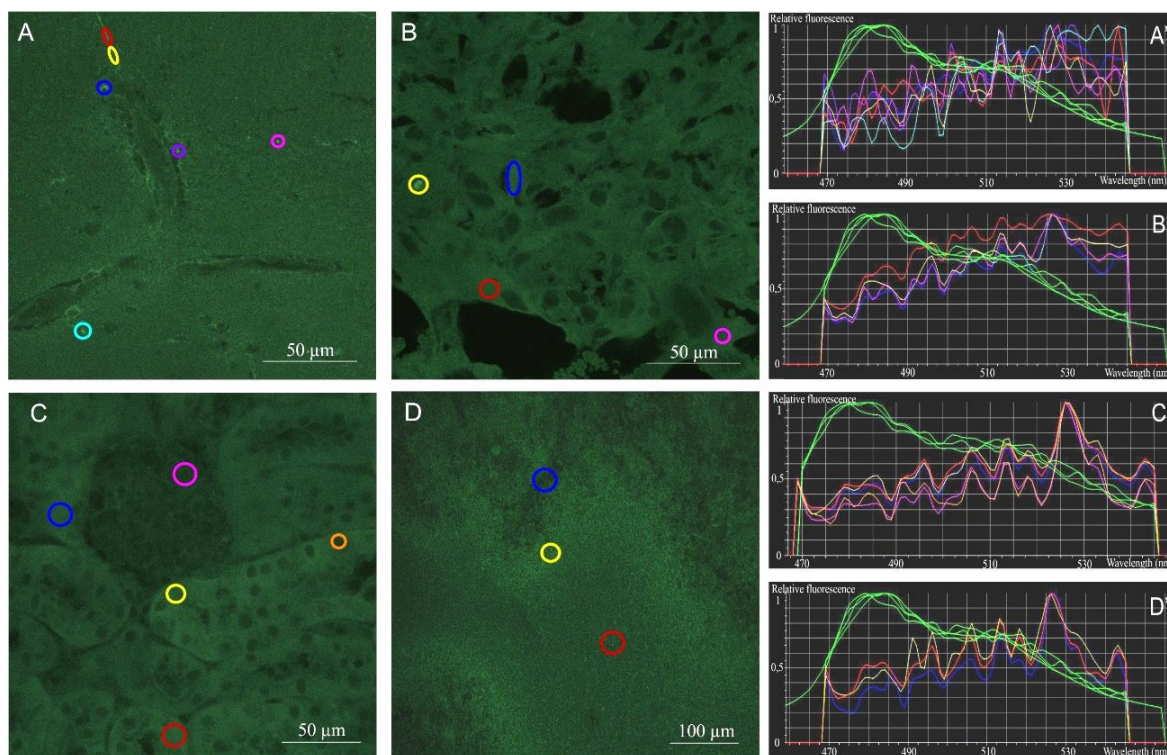


**Figure 33: Control spectra for in vivo measurements**

Spectral images showing the autofluorescence of non-treated brain (A), placenta (B), kidney (C) and spleen (D) sections used as negative controls in *post hoc* spectral identification of nanoparticles in tissues after *in vivo* NP-distribution. A', B', C', D': spectrum profiles of ROIs in the corresponding images. The spectrum of each ROI is marked with the same color as it is delineated in the microscopic image. Green curves represent fluorescence of “yellow” polystyrene nanoparticles (positive controls); red curve represents the spectrum of tissue autofluorescence (used as negative control later on).

To quantitatively classify the NP-content of ROIs a spectral ratio (SR) was calculated from the relative fluorescence intensities at reference wavelengths. The reference wavelengths corresponded to the intensity maximums of NP-fluorescence and the tissue autofluorescence. For samples containing “Yellow” polystyrene NPs the SR was calculated from the relative fluorescence intensities at 483nm and 528nm reference wavelengths ( $SR_{PS-NP} = \text{relative fluorescence intensity at 483 nm} / \text{relative fluorescence intensity at 528 nm}$ ). For other particles see Table 3. ROIs were considered as NP-containing if the spectral ratio was above 1 ( $SR > 1$ ).

With the use of positive and negative spectral controls and spectral ratios, nanoparticles were reliably detected in various environments. Spectral imaging fluorescence microscopy proved to be a valuable tool to monitor fluorescent nanoparticles in samples where high autofluorescence is an issue.

Spectral fluorescence microscopy combined with confocal z-stack analyses could identify particle derived fluorescence intracellularly in microglia. The technique demonstrated that microglia cells internalized the plain  $\text{SiO}_2$ ,  $\text{SiO}_2\text{-NH}_2$  and the  $\text{SiO}_2\text{-SH}$  NPs, while  $\text{SiO}_2\text{-PVP}$  particles were rarely found inside cells (Figure 34).

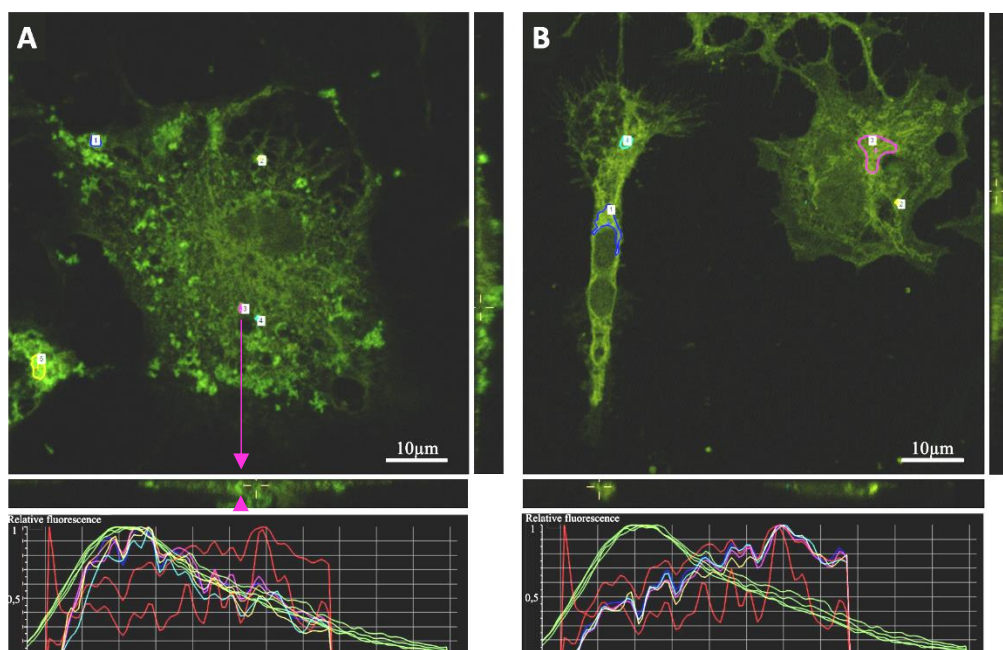


**Figure 34: Microglia cells internalize  $\text{SiO}_2$ ,  $\text{SiO}_2\text{-NH}_2$  and  $\text{SiO}_2\text{-SH}$  nanoparticles, but not  $\text{SiO}_2\text{-PVP}$**

Spectrum analyses was carried out on Z-stack optical slices of non-stained primary microglia cells to identify internalized silica nanoparticles. A: pristine  $\text{SiO}_2\text{-NP}$  treated culture. B:  $\text{SiO}_2\text{-PVP}$  treated culture. The spectrum of each ROI is marked with the same color as it is delineated in the microscopic image. Arrows in A mark the localization of ROI in the z-projection, showing intracellular localization. Lower panels: spectrum analysis confirms that the spectrum of the ROI is identical with particle derived fluorescence ( $\text{SR} > 1$ ). Green curves represent particle fluorescence (positive controls,  $\text{SR} = 2,0$ ); red curve represents autofluorescence of the non-treated culture (negative control: red curves  $\text{SR}_{\text{red1}} = 0,7$ ;  $\text{SR}_{\text{red2}} = 0,5$ ),  $\text{SR}$  for other ROIs in A:  $\text{SR}_{\text{blue}} 1,8$ ;  $\text{SR}_{\text{pink}} 1,7$ ;  $\text{SR}_{\text{yellow}} 2,0$ ;  $\text{SR}_{\text{aquamarine}} 2,0$ ;  $\text{SR}_{\text{orange}} 1,8$ ; in B:  $\text{SR}_{\text{blue/pink/yellow/aquamarine}} 0,6$ .

#### 5.4. In vivo distribution of polystyrene nanoparticles

To determine how the molecular surface characteristics of otherwise identical polystyrene NPs could influence tissue penetration and accumulation, I applied optimized spectral imaging fluorescence microscopy technique on tracking particles coated with either carboxylated (PS-COOH) or PEGylated (PS-PEG) surfaces.

Fluorescent PS-COOH or PS-PEG particles were suspended in PBS by sonication and administered via a single tail-vein injection into adult male (aged 25-30 days) or pregnant

female mice on the 10th to 15th post conception days. For evaluation of short-term and longer-term distribution of NPs, mice were sacrificed either 5 minutes ( $n_{\text{PS-COOH}} = 3$ ;  $n_{\text{PS-PEG}} = 3$ ), or after a 4-day long survival period ( $n_{\text{PS-COOH}} = 3$ ;  $n_{\text{PS-PEG}} = 3$ ). The anatomical distribution of PS-NPs in various organs were determined by fluorescence spectrum analysis (Figure 35).

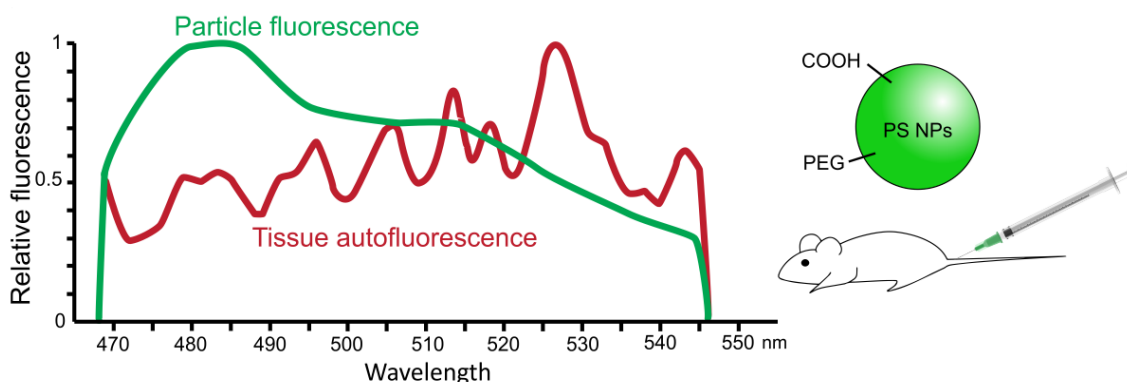


**Figure 35: Experimental design and fluorescence spectrum analysis of tissue samples of NP-treated mice**

Carboxylated or PEGylated particles were administered to mice through a single tail vein injection. After 5-minutes or 4-days exposure distribution of NPs was evaluated by fluorescent spectrum analysis. Spectrum of selected regions in tissue slices from treated mice were compared to the autofluorescence of non-treated tissues (red curve, negative control) and to the fluorescence of NPs (green curve, positive control) by calculating the SR at 483 and 528 nm. ROIs were considered NP-containing if  $\text{SR} > 1$ .

Intravenous injection of PS-COOH or PS-PEG nanoparticles at a blood-concentration of  $33.3 \mu\text{g/ml}$  did not cause circulatory blockage or other life threatening condition.

The organs studied in details including the brain, kidney, liver, placenta and the spleen contained different amounts of nanoparticles, and displayed distinct extent of clearing after the 4-day post-injection period (Table 6).

**Table 6: Presence of polystyrene nanoparticles after intravenous injection**

Organs were excised 5 minutes or 4 days after the particles were administered into the tail vein.

		Brain	Placenta	Kidney	Liver	Spleen	Embryonic tissue
PS-COOH	5 min	+	+	+	+	+	-
	4 days	-	-	-	+	+	-
PS-PEG	5 min	-	-	+	+	+	-
	4 days	-	-	+	+	+	-

Five minutes after nanoparticle injection, high abundance of both PS-COOH and PS-PEG NPs were found within the kidney, liver and the spleen known to be responsible for elimination of toxic products from the body. In the brain and the placenta protected by physiological barriers, only PS-COOH NPs were deposited, and PS-PEG NPs were rarely found (Table 6).

In the brain, aggregated PS-COOH particles were concentrated in large vessels and capillaries, whereas the parenchyma was largely devoid of NPs (Figure 36 A-A', Figure 37). The attachment to vessel walls was restricted to short-term exposure, PS-COOH NPs completely cleared out from the brain in four days after nanoparticle administration (Figure 36 C-C'). In accord with the *in vitro* experiments, PEGylation reduced the interaction of NPs with the environment, including the attachment to vessel walls (Figure 36 B-B' and D-D', Figure 37).

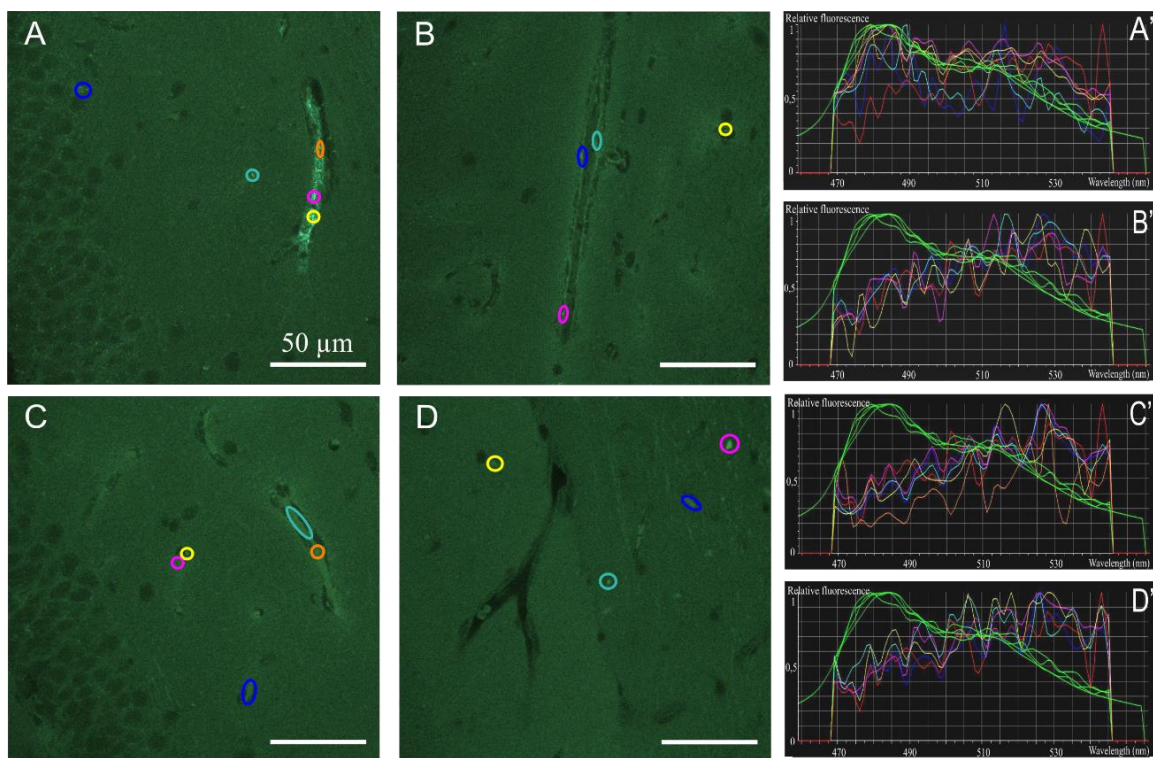


**Figure 36: Distribution of PS-NP in the brain after systemic exposure**

Spectral images of tissue sections from the mouse brain 5 minutes (A, B) and 4 days (C, D) after injection of PS-COOH (A, C) or PS-PEG (B, D) nanoparticles into the tail vein. A', B', C', D': spectrum profiles of ROIs in the corresponding images. Spectrum analysis proves the presence of PS-COOH NPs in brain vessels 5 minutes after exposure (A') and indicates their clearance after 4 days (C'). PS-PEG particles did not attach to vessel walls (B-B' and D-D'). The spectrum of each ROI is marked with the same color as it is delineated in the microscopic image. Green curves represent particle

fluorescence (positive controls, SR = 1,9); red curve represents tissue autofluorescence (negative control; SR = 0,6). SR for ROIs in A: yellow-1,5; pink-1,3; orange-1,3; blue-1,2; aquamarine-1,6; SR of ROIs in B-C-D were between 0,5 and 0,7.

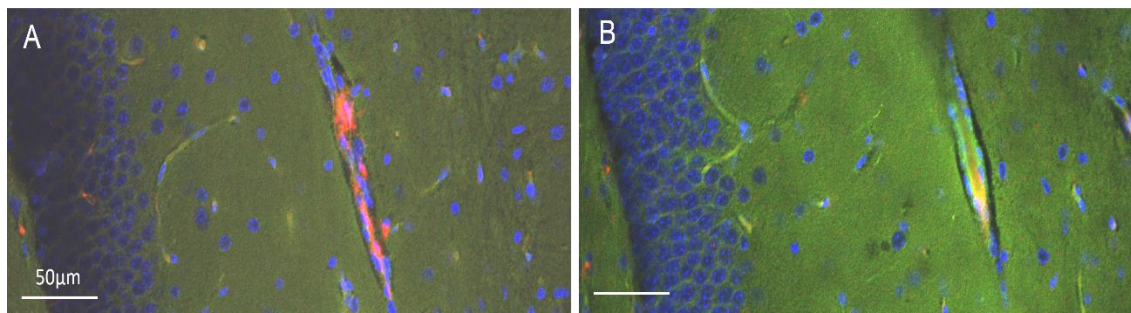


**Figure 37: Polystyrene NPs in brain vessels**

Fluorescence images of sections made from the forebrain of PS-PEG (A) or PS-COOH (B) injected adult mice. Animals were sacrificed 5 minutes after intravenous injection. Sections were stained for Claudin V (red); cell nuclei are shown in blue. Scale bars: 50  $\mu$ m

Spectrum analysis proved the presence of PS-COOH NPs in brain vessels 5 minutes after exposure and indicated an almost complete clearance after 4 days. PS-PEG particles did not attach to vessel walls even 5 minutes after administration.

In the placenta, PS-COOH NPs, but not PS-PEG NPs were seen in the lacunas (Figure 38), and importantly, neither type of nanoparticles was found in embryonic tissues (Figure 39), indicating a proper placental barrier function. As in the brain, both types of particles cleared out completely from the placenta within 4 days (Figure 38).

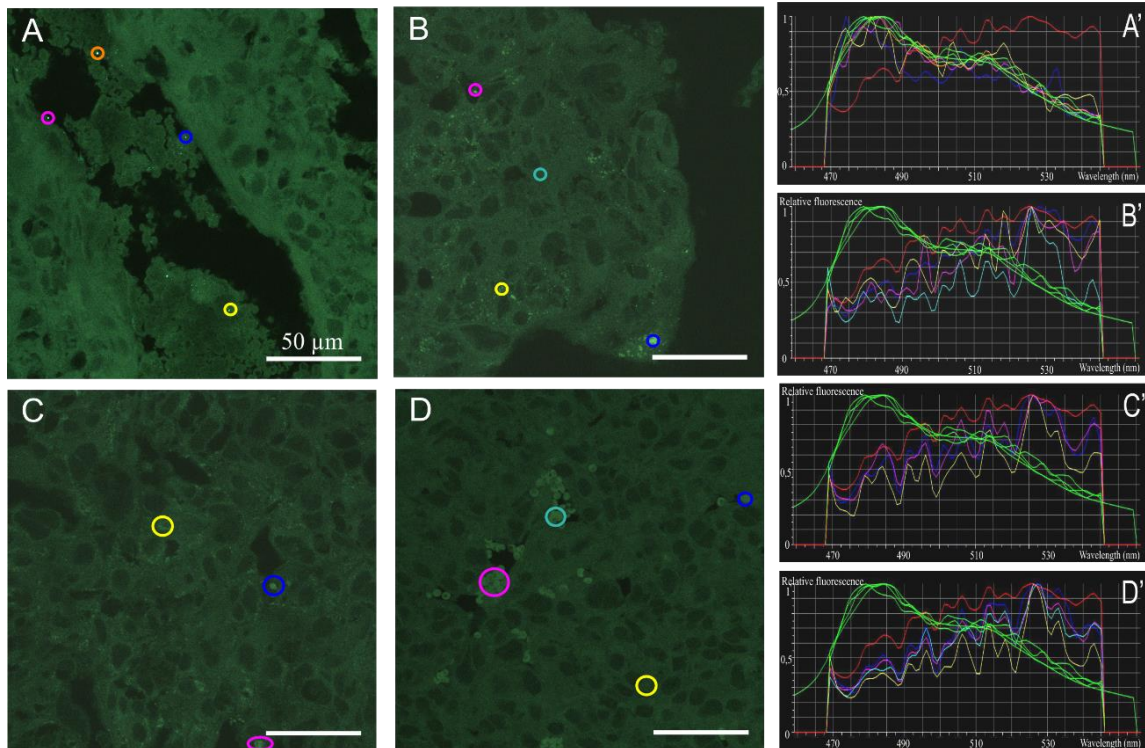


**Figure 38: Distribution of PS-NPs in the placenta**

Spectral images of tissue sections from placenta 5 minutes (A, B) and 4 days (C, D) after injection of PS-COOH (A, C) or PS-PEG (B, D) nanoparticles into pregnant female mice. A', B', C', D': spectrum profiles of ROIs in the corresponding images.

Spectrum analysis shows PS-COOH particles in the lacunas of placenta 5 minutes after exposure (A') and indicates clearance after 4 days (C'). The spectrum of each ROI is marked with the same color as it is delineated in the microscopic image. Green curves represent particle fluorescence (positive controls, SR = 1,9); red curve represents tissue autofluorescence (negative control, SR = 0,6). SR for ROIs in A: yellow-1,8; pink-2,0; orange-2,0; blue-1,8; SR of ROIs in B-C-D were under 0,6.

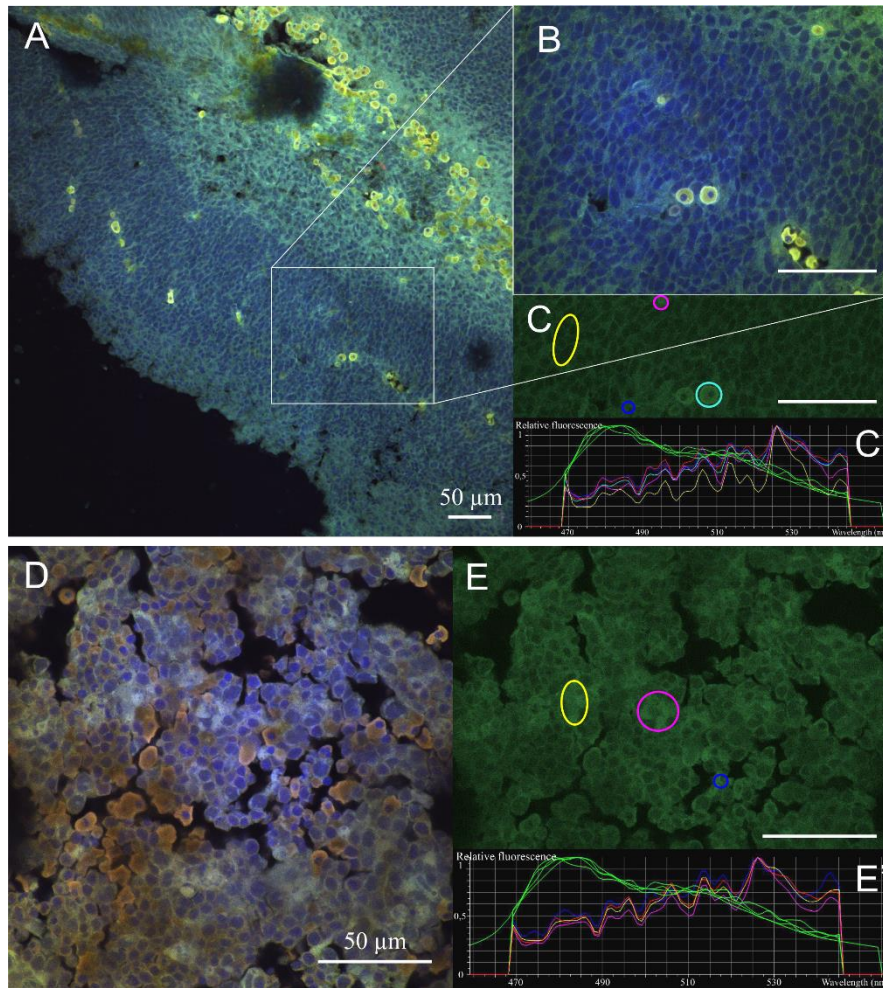


**Figure 39: Embryonic tissues were free from nanoparticles 5 minutes after maternal NP-administration**

Sections were made from mouse embryonic (E 15) forebrain cortex (A, B, C) and liver (D, E) 5 minutes after the injection of carboxylated PS-NP into the tail vein of the mother. Cell nuclei were stained with bisbenzimidazole (blue). Representative spectrum images (C, E) and spectrum profiles (C', E') showed no particles in the embryonic brain or liver tissues ( $SR_{ROI} < 1$ ). Scale bars: 50  $\mu\text{m}$ .

In striking contrast to the brain and the placenta, both PS-COOH and PS-PEG NPs were present in the kidney 5 minutes after nanoparticles administration. Particles were found in the glomeruli and also in the interstitium around the tubuli (Figure 40 A-A' and C-C'). Four days later, PS-COOH NPs cleared from the kidney, while a few PS-PEG NPs were still stuck within the glomeruli (Figure 40 B-B' and D-D').

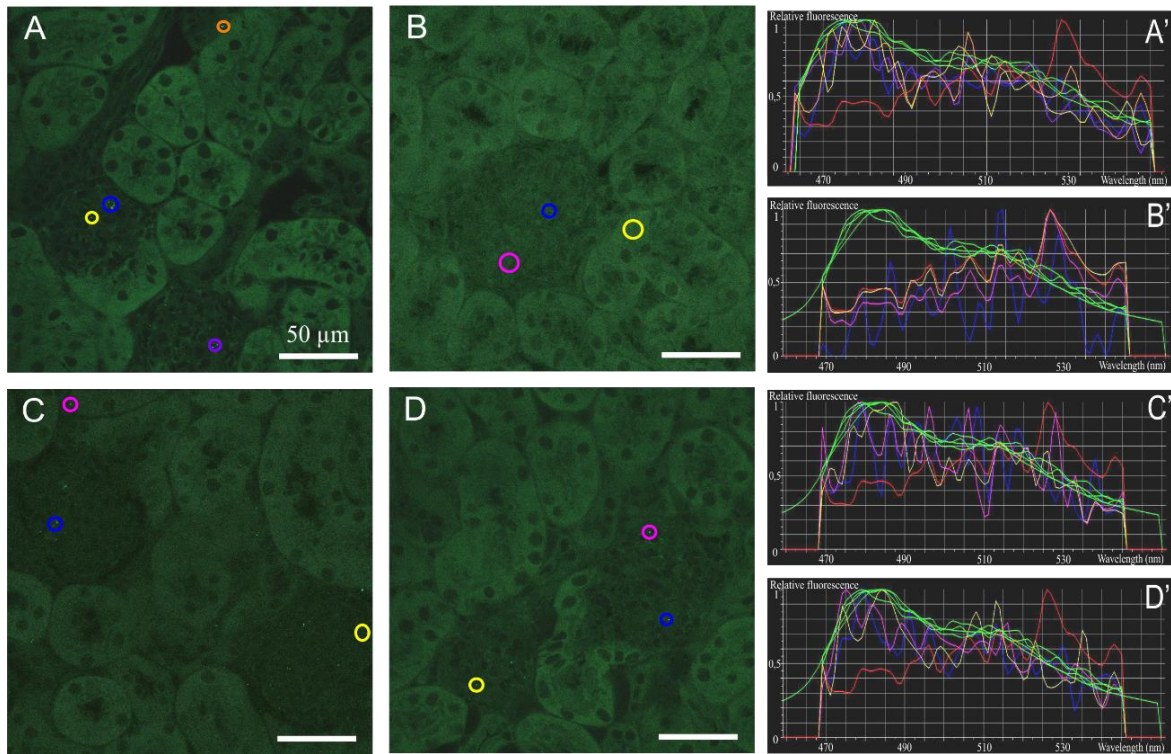


**Figure 40: Distribution and accumulation of polystyrene nanoparticles in the kidney**  
Spectral images of adult mouse kidney sections 5 minutes (A, C) and 4 days (B, D) after injection of PS-COOH (A, B) or PS-PEG (C, D) nanoparticles through the tail vein. A', B', C', D': spectrum profiles of ROIs in the corresponding images. The spectrum of each ROI is marked with the same color as it is delineated in the microscopic image. Green curves represent particle fluorescence (positive controls, SR = 1,9); red curve represents tissue autofluorescence (negative control, SR = 0,5). SR for ROIs in (A): yellow-2,0; purple-2,2; blue-1,8; orange-1,5; (B): yellow-0,5; pink-0,4; blue-0,3; (C): yellow-1,6; pink-1,1; blue-1,6; (D): yellow-2,3; pink-1,8; blue-1,6.

In the liver, high densities of both NPs were found regardless of the functionalization, and PS-COOH and PS-PEG NPs were detected even after 4-day survival. The abundance of particles was clearly seen with traditional fluorescence microscopy (Figure 41).

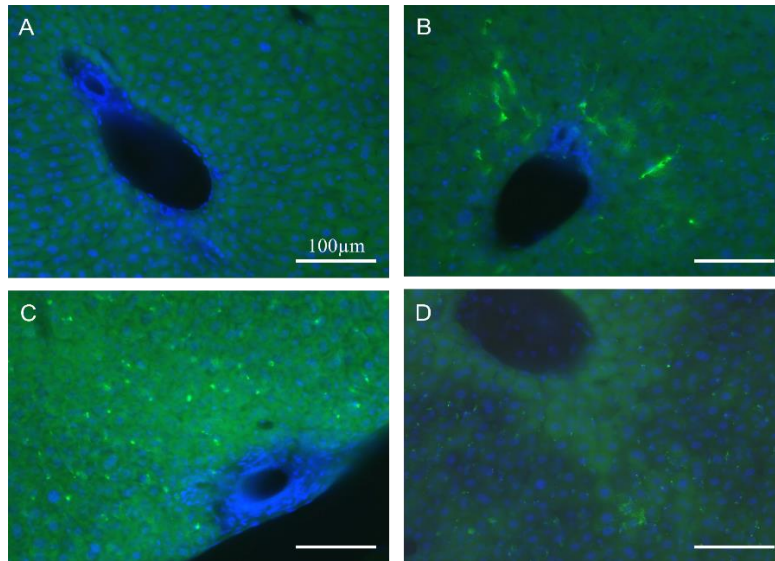


**Figure 41: PS-NPs accumulate in the liver**

Traditional fluorescence microscopic images of liver sections of non-treated (A) and NP-injected (B, C, D) adult mice. Animals were sacrificed 5 minutes (B) and 4 days (C) after intravenous injection of PS-COOH NPs and 4 days after injection of PS-PEG (D) NPs. Green: fluorescent PS-NP; blue: bisbenzimidazole nuclear staining in blue.

In the spleen, nanoparticles with both functional groups were identified in high densities (Figure 42). In 5-minute exposure, NPs were mainly restricted to the marginal zone, which is a region enriched in monocytes/macrophages (Bronte and Pittet 2013). Colocalization analysis directly demonstrated the presence of both NPs within the Iba-1 immunopositive phagocytic cells (Figure 43).

After 4 days, a characteristic redistribution of particles was detected regardless of functionalization. NPs with both functional groups were identified in the white pulp (Figure 42, red arrows).

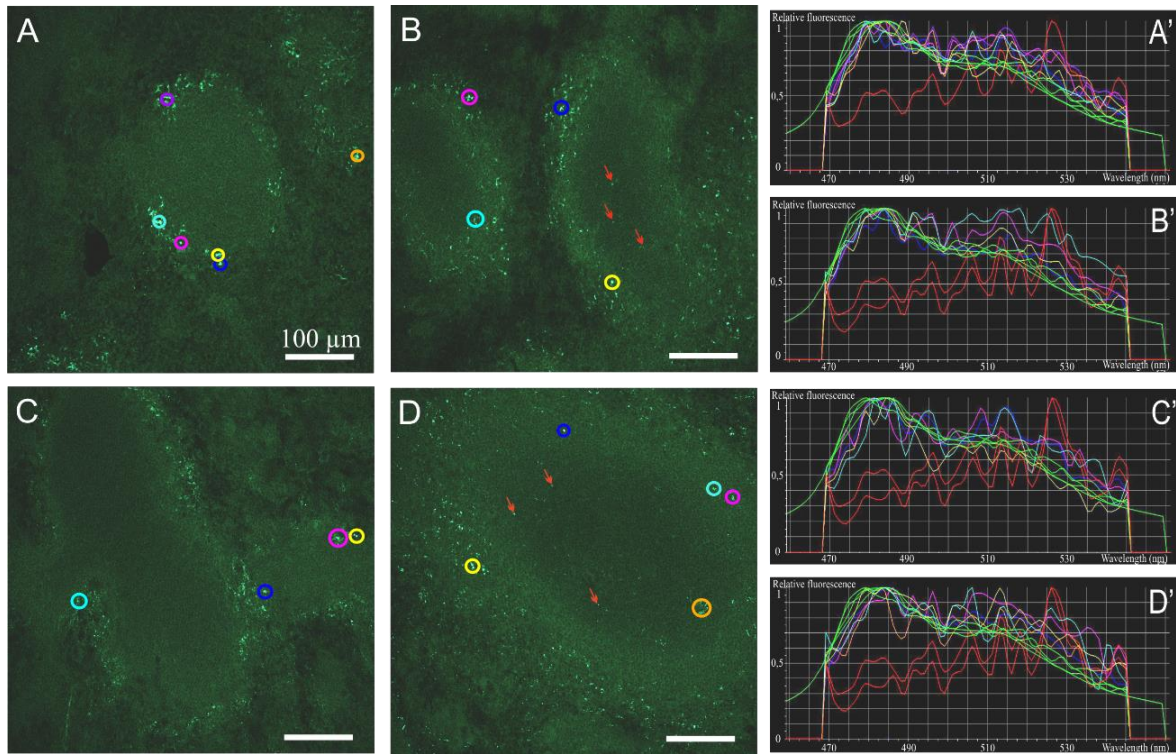


**Figure 42: Distribution and accumulation of PS nanoparticles in the spleen**

Spectral images of mouse spleen sections after a single intravenous injection of carboxylated (A, B) or PEGylated (C, D) polystyrene nanoparticles, 5 minutes (A, C) and 4 days (B, D) after exposure. Red arrows indicate translocated particles to the white pulp during the 4-day after exposure period. A', B', C', D': spectrum profiles of ROIs in the corresponding images. The spectrum of each ROI is marked with the same color as it is delineated in the microscopic image. Green curves represent particle fluorescence (positive controls,  $SR = 2,0$ ); red curves represent tissue autofluorescence (negative controls,  $SR_1 = 0,4$ ;  $SR_2 = 0,5$ ). SR for ROIs in A-B-C-D were above 1,2.

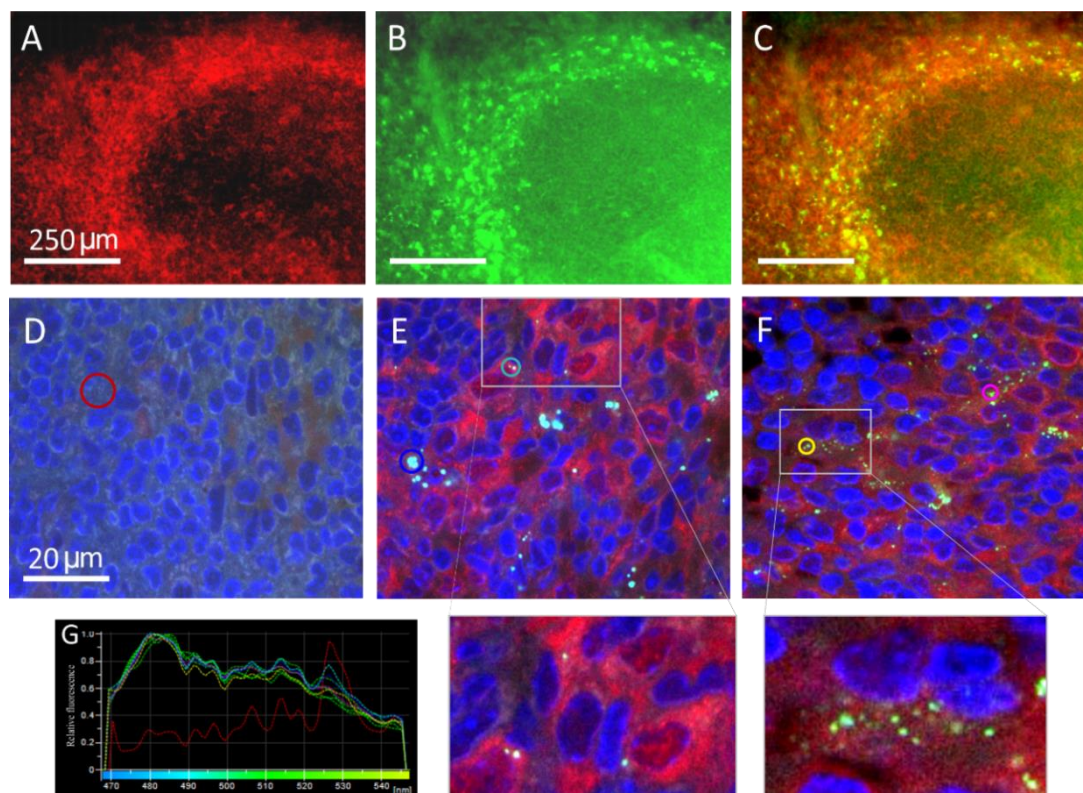


**Figure 43: PS-NPs are associated with monocytes/macrophages, identified by Iba-1 staining**

A-C: Immunohistochemical staining of spleen macrophages, with anti-Iba-1 antibody (A; red), and visualization of carboxylated PS-NPs (B; green) 4 days after a single intravenous injection of nanoparticles. Merged image (C) shows that nanoparticles (green) are co-localized with the Iba-positivity of marginal zone macrophages (red).

D-F: Confocal images of spleen sections from non-treated (D) or PS-PEG-injected (E, F) mice. Samples were collected 5 minutes (E) or 4 days (F) after exposure to PS-PEG, and were stained for Iba-1. The sample from non-treated animal (D) serves also as staining control. Enlarged areas of the boxed regions in E and F, show the presence of PS-PEG NPs in Iba-1 positive phagocytotic cells. G: The spectra of ROIs indicated the presence of PS-PEG NPs on images of both, 5-min (blue and turquoise ROI) and 4-day (yellow and pink ROI) samples. The spectrum of each ROI is marked with the same color as it is delineated in the microscopic image. Fluorescence spectrum of ROIs were compared against spectrum of non-treated sample (autofluorescence, red curve, SR = 0,3) and particle fluorescence (positive controls, green curves, SR = 1,9). SR of ROIs: blue-1,4; turquoise-1,3; yellow-1,7; pink-1,7.

Taken together, spectral imaging fluorescence microscopy was instrumental in characterizing the extent of polystyrene nanoparticle penetration into different organs. The proper barrier-functions of the blood-brain-barrier and the placenta prevented the penetration of nanoparticles into the brain parenchyma and embryonic tissues, respectively. PS-COOH NPs attached to vessel walls, while PEGylation proved to be enough to prevent particles from adhering to the vascular endothelium. On the other hand,

in organs which are responsible for detoxication of the body, as the kidney, liver and the spleen, significant amounts of PS-NPs were accumulated, and this accumulation was not prevented by PEGylation.

## 6. DISCUSSION

As the biological behavior of nanoparticles is influenced by multiple factors (Nel et al. 2009), one of the key elements of nanomaterial related research is the thorough characterization of the particles. The comprehensive knowledge on the properties of NPs (naïve NPs or NPs modified by the experimental milieu) is crucial to understand and interpret biological results.

My thesis research was focused on the impacts of chemical surface-compositions on the biological interactions of nanoparticles. To dissect the effects, nanoparticles with uniform size and shape but with different chemical surface compositions were used throughout the experiments. Polystyrene and silica was chosen as the core material of NPs, because of their stability in biological solutions, and because ions or toxic compounds could not dissolve from them (Cohen et al. 2002, Food and Drug Administration 2013).

Polystyrene nanoparticles were functionalized with carboxyl- or PEG-functional groups, while silica nanoparticles were either left unmodified (SiO<sub>2</sub>-NP) or functionalized with amino-, mercapto- or PVP functionalities (SiO<sub>2</sub>-NH<sub>2</sub>, SiO<sub>2</sub>-SH, SiO<sub>2</sub>-PVP). As expected, surface-coating resulted in significantly different zeta-potential of NPs, ranging from strongly negative to positive values. Physicochemical characterization of PS- and SiO<sub>2</sub>-NPs revealed that the size, shape and the fluorescence spectra of the emitted light of NPs were not disturbed by surface functionalization.

Besides core material, size, shape, and surface composition the biological distribution of NPs is highly influenced by substances adsorbed on NP surfaces, (Nel et al. 2009). Due to the highly reactive surfaces, nanoparticles attach to and adsorb chemical substances from the surrounding environment (Casals et al. 2010, Monopoli et al. 2012). The composition and thickness of adsorbed layers (the so-called corona) depends on the chemical properties of both the NP surface and the environment (Casals et al. 2011, Lundqvist et al. 2011, Casals and Puntès 2012). The corona governs the interaction of NPs with biological structures, hence it plays a decisive role in the tissue- and cell-type-specific NP distribution (Salvati et al. 2013, Tenzer et al. 2013). By changing the chemical reactivity of NP-surfaces, for example by coating the particles with „passivating” functional groups (Peracchia et al. 1999b, Sacchetti et al. 2013), the composition of the adsorbed corona can be altered both quantitatively and qualitatively. Our own electrophoresis data confirmed that PEGylation could not only reduce aggregation in

organic solutions, but could also scale down the amount of adsorbed proteins on particles. Similar results were shown for PVP-coated silica nanoparticles incubated in 10% FCS-MEM (Izak-Nau et al. 2013a, 2013b).

We showed previously, that neither of the investigated particles displayed toxic effects on cells exposed to particles *in vitro* up to concentrations of  $10^{11}$  NPs/ml (Izak-Nau et al. 2013a, Murali et al. 2015). In *in vitro* uptake experiments, incubation with  $3.5 \times 10^{10}$  to  $5 \times 10^{11}$  NPs/ml polystyrene or silica nanoparticles in serum free conditions did not result in obvious structural damage to cells. Cell viability (MTT-reduction assay) and membrane integrity (LDH-release assay) tests confirmed, that polystyrene or silica NPs are not toxic for the investigated neural cell types (Izak-Nau et al. 2013a, Murali et al. 2015). Mild toxicity was detected only at extremely high concentrations ( $10^{12}$  -  $10^{13}$  particles/ml), which is 100 times higher than we used in the presented *in vitro* experiments. The variations in the mild *in vitro* effects correlated with the chemical surface composition of particles. Amine functionalization of SiO<sub>2</sub> NPs increased, while PVP coating reduced the particle toxicity (Izak-Nau et al. 2013a). Similarly, carboxylated PS NPs showed slightly but significantly increased cellular effects in comparison to PEG coated particles (Murali et al. 2015). The data of my thesis work demonstrated that nanoparticles with PEG- or PVP-coated surfaces displayed markedly different *in vitro* and *in vivo* distribution compared to particles with non-passivated, ionic surface groups (Kenesei et al. 2016).

Fluorescence microscopy is generally the method-of-choice in biomedical studies to monitor fluorescent materials, including nanoparticles (Bouccara et al. 2015) at the tissue and cellular levels. However, visualization of fluorescent NPs even with high-resolution confocal microscopy has been notoriously difficult, because the size of NPs is below Abbe's diffraction limit. Therefore, fluorescent NPs can only be detected if they passively aggregate in the cellular media or at biological interfaces (e.g. on the blood vessel wall or on the cell surface) (Gambinossi et al. 2014), or if they are actively taken up by cells and are concentrated into endocytotic vesicles or lysosomes (Al-Rawi et al. 2011, Firdessa et al. 2014, Murugan et al. 2015). In serum free conditions PS-COOH, SiO<sub>2</sub>, SiO<sub>2</sub>-NH<sub>2</sub> and SiO<sub>2</sub>-SH nanoparticles formed light microscopically detectable agglomerates, which

settled on and attached to cell surfaces. In agreement with the DLS data on reduced agglomeration and reduced protein adsorption, PVP- and PEG-functionalized NPs did not form such detectable agglomerates on cell surfaces.

Cellular uptake of nanoparticles depended on functional groups, and was less related to the core material. The internalization of nanoparticles with hydrophilic, strongly charged functional groups, like PS-COOH, SiO<sub>2</sub>, SiO<sub>2</sub>-NH<sub>2</sub> and SiO<sub>2</sub>-SH was markedly higher, compared to the hydrophobic and neutral PVP- and PEG-functionalized particles. While cell surface attachment of silica particles was more pronounced, than that of PS-NPs; important *in vitro* internalization of particles was observed only in cultures of the phagocytic microglia cells. Astrocytes which are also known to phagocytose smaller cell debris from their environment (Sokolowski and Mandell 2011) were occasionally labelled by silica NPs, but confocal z-stack imaging showed surface attachment of particles without internalization. Importantly, neural stem cells and neurons, including neurons differentiated from stem cells *in vitro*, and those isolated from the mouse forebrain and cultured in primary cultures did not take up any of the particles.

The surface attached particle aggregates in cell cultures could be formed by spontaneous particle aggregation, as shown in cell-free aggregation experiments. The intracellularly localized particle aggregates in microglia, however, suggested, that nanoparticles were internalized through active cellular processes, like phagocytosis and pinocytosis, and were collected in endocytotic vesicles, phagosomes or lysosomes. To test whether intracellular accumulation was a result of active cellular uptake, primary brain cell cultures were exposed to nanoparticles at 4°C and compared to cultures treated at physiological 37°C. The reduced accumulation of NPs at 4°C indicated that the microglial NP uptake is a temperature- and activity-dependent process. The results were in accordance with recent publications showing that medium-sized (20nm < x > 100nm) PS-NPs can be internalized by multiple energy-dependent processes, including macropinocytosis, phagocytosis, clathrin-mediated endocytosis, caveolae-mediated endocytosis, and clathrin- and caveolae-independent pathways, which can collect NPs in acidic vesicles through the endolysosomal pathway (Firdessa et al. 2014). These vesicles display high autofluorescence. Therefore, the identification of fluorescent particles in such vesicles could be achieved only by distinguishing particle fluorescence from the light emitted by the vesicle material. Fluorescence spectrum analyses together with

temperature-dependent uptake experiments demonstrated that *in vitro*, ~ 50 nm silica or polystyrene NPs were actively internalized only by “professional” phagocytes.

The *in vivo* distribution of differently functionalized polystyrene nanoparticles, namely PS-COOH NPs, representing strong negative surface charge, and PS-PEG particles with hydrophilic and charge-neutralizing -PEG chains, were assessed in mice after a single intravenous injection. The use of particles in the ~50 nm size range promised several advantages. Particles were comparable in size with natural assemblies of protein complexes, but were big enough not to be excreted rapidly by the kidney, which is known to retain proteins and particles larger than 10 nm (Choi et al. 2007).

The single tail-vein injection equaled to a blood-concentration of 33.3 µg/ml nanoparticles, which corresponds to  $1.2 \times 10^{11}$  NPs/ml blood. This concentration is 10 times lower, than the concentration where mild toxicity was observed on cultured neural cells (Murali et al. 2015). Additionally, PS-COOH and PS-PEG particles were expected not to impair the blood flow conditions at the time of injection. According to *in vitro* results, large-scale aggregate formation, which could block circulation, was not expected. In the experiments, intravenous injection of  $1.2 \times 10^{11}$  NPs/ml PS-COOH or PS-PEG nanoparticles did not cause life circulatory blockage or other life threatening conditions in mice.

Several imaging approaches have already been used to visualize nanoparticles *in vivo* (Ostrowski et al. 2015). Some studies investigated NP distribution at the whole-body level by using magnetic resonance imaging, computed tomography, positron emission tomography, or radiolabeling techniques (Choi et al. 2007, Leary and Key 2014, Liu et al. 2014); whereas other reports focused on the subcellular localization of NPs by exploiting transmission or scanning electron microscopy (Fagerland et al. 2012, Ye et al. 2015). Relatively few studies attempted to follow the *in vivo* distribution of distinct types of NPs at the tissue and cellular levels (Cho et al. 2009, Liu et al. 2014, Liba et al. 2016). This approach would be important from a medical perspective, because specific tissues and cells may be differentially involved in pathophysiological responses to nanoparticle exposure. Yet the availability of high-throughput imaging modalities to compare the distribution of different NPs in the living body, is rather limited.

The small size of NPs, which is below the resolution of diffraction limited systems, makes the detection of fluorescent NPs in biological samples challenging. Fluorescent NP-detection is further hindered by the high autofluorescence of biological samples, which does not allow visualizing small and scattered particles due to the low signal-to-noise ratio (Bouccara et al. 2015). Increasing fluorescent dye concentration on the NP surface may lead to enhanced cytotoxicity; therefore, interest was turned to polymer nanoparticles which encapsulate fluorescent dyes. While the covalent embedding of the dye into the core-material prevents dissolution, the amount of “in-core” dye is limited (Hu and Gao 2010, Naczynski et al. 2010) and hinders the fluorescence detection.

These constraints stressed the importance of applying new imaging approaches in the studies on tissue- and cell-type-specific NP distribution of fluorescent NPs, and prompted us to adapt spectral imaging fluorescence microscopy, with the aim to overcome the limitations caused by low NP fluorescence versus high tissue autofluorescence. The high-resolution of confocal microscopy combined with spectral acquisition and *post hoc* spectrum analysis enabled more detailed regional and cellular analysis of nanoparticles in various tissues.

For evaluation of short-term and longer-term distribution of NPs, mice were sacrificed either 5 minutes, or after a 4-day long survival period. Initial distribution of particles could not be revealed by histological methods because of the high heart rate (300-800 beats/min) and 20-45  $\mu$ l stroke volume of mice resulting in an average 20 ml/min cardiac output (Janssen et al. 2002). The 5 min exposure allowed investigating short-term tissue distribution of particles after a single injection and comparison to a longer term (4 day) distribution.

Five minutes after NP-injection, significantly more PS-COOH than PS-PEG particles were found at the walls of brain vessels and in the placenta. As it was expected from prior experiments and from literature data (Peracchia et al. 1999a, Chilukuri et al. 2008), PEGylation inhibited the attachment of particles to biological interfaces and kept particles longer in the circulation. On the other hand, PS-COOH particles could interact with vessel walls and cell surfaces and were detected in both the brain vessels and the placenta. However, particles were never found in the brain parenchyma or in embryonic tissues, indicating a proper barrier function of the blood-brain barrier and the placenta against PS-

NP, as it was shown also in *ex vivo* human placental perfusion model (Grafmueller et al. 2015).

As opposed to *in vitro* uptake experiments, PEGylation could not prevent the *in vivo* uptake of PS-PEG NPs by professional macrophages (Moghimi et al. 1991, Moros et al. 2012). We found a remarkable accumulation of both PS-COOH and PS-PEG nanoparticles in the kidney, liver and the spleen, e.g. in organs responsible for elimination of particulate polluting agents from the circulation. The apparent controversy between the *in vitro* and *in vivo* uptake of PEGylated PS-NPs by macrophages may be explained by two conditions:

- i) *in vitro* uptake took place in serum-free conditions, where the adsorbed corona layers of PEGylated particles are substantially different from those formed *in vivo*, in the blood circulation;
- ii) The *in vitro* investigated microglia cells exist in different activation-state in comparison to *in vivo* macrophages. This later assumption is supported by our earlier findings (Murali et al. 2015) that cyto-active substances as lipopolysaccharides built on the surface of PS-PEG NPs destroys the attachment-reducing effect of PEGylation.

After 4 days, the particles were completely cleared from the vessels of the brain and the placenta, but were accumulated in the liver and the spleen. The persisting presence of PS-PEG particles in the glomeruli, suggested that particles were accumulated by intraglomerular mesangial cells known to phagocytose contaminating particles, mesangial matrix material and cell debris (Schlöndorff and Banas 2009). In the spleen, several particles were translocated from the marginal zones into the white pulp during the 4-day post-injection period. The observations on the storage and translocation of these nanoparticles are worthy of further consideration, since they may suggest a route for antigen presentation. As particles surfaces can adsorb multiple compounds, including toxins (Murali et al. 2015) and compounds of decaying cells, several particle-carried material can be presented by spleen macrophages to the lymphocytes of the white pulp (Bronte and Pittet 2013) and on that way adaptive immune responses can be initiated. Regarding the above considerations, the inflammation-initiating effects of otherwise “harmless” NPs should not be neglected.

The observations indicate that medium-sized (50-90 nm) non-biodegradable nanoparticles which are captured by macrophages in the spleen and the liver or even in the kidney interstitium, cannot be easily removed from the body. Regarding the fact that material of dying cells will be ingested by neighboring phagocytes, the question can be raised whether such particles can be cleared at all. Long-term accumulation and limited clearance may cause problems if repeated nanoparticle loading is considered, even if the acute single dose of potentially “harmless” particles is low.

For studies on particle penetration and long-term tissue-residence, spectral imaging fluorescence microscopy may provide methods which can monitor the distribution and accumulation of fluorescently labeled NPs. The results demonstrate that carefully controlled fluorescence spectrum analysis can find NPs in various tissues with high accuracy and in a time-frame which cannot be achieved with electron microscopy.

## 7. CONCLUSIONS

The results of my thesis work led to the following conclusions on the altered characteristics, cellular uptake and *in vivo* distribution of differently functionalized polymer nanoparticles:

- The cellular uptake and biodistribution of NPs is essentially modified by the chemical composition of the NP's surface.
- Passivating the NP surfaces with PEGylation or PVP-coating reduces the amount of proteins adhered to particles, alters the protein corona composition, scales down the aggregation in organic solutions and inhibits the interactions with the environment, including biomolecules and cells.
- Cellular interactions of NPs are highly dependent on the types of cells and the surface characteristics of NPs:
  - Neurons and neural stem cells did not take up ~50 nm silica or PS NPs *in vitro*.
  - In astrocyte enriched primary cultures, GFAP positive astrocytes did not internalize silica or PS NPs, even if strong attachment of charged silica NPs to cell surfaces was observed. The phenomenon was reduced by PEGylation or PVP-coating of the particles.
  - Microglia cells internalize significant amounts of silica and PS-NP by energy-dependent endocytic mechanisms, while PEGylation and PVP-coating markedly reduced the process.
- Chemical properties of the nanoparticle surfaces interfere with the *in vivo* fate of PS particles including short-term invasion and longer-term accumulation:
  - Initial attachment to blood vessel walls is reduced by PEGylation.
  - Barrier functions of the blood-brain-barrier and the placenta completely prevents the penetration of particles into the brain parenchyma and embryonic tissues, respectively.
  - Particles with carboxylated or PEGylated surface functionalizations were retained in the reticuloendothelial organs. Strong accumulation of PS-COOH and PS-PEG was detected in the liver, in the macrophages of the spleen marginal zones, and some particles were found also in the

intraglomerular mesangium of the kidney. The accumulation and long-term storage of nanoparticles in the reticuloendothelial systems rise important questions on the long-term health-risk even of otherwise non-toxic particles.

- Spectral imaging fluorescence microscopy allowed detecting the tissue- and cell-type-specific accumulation of fluorescent polymer nanoparticles in a time-frame which cannot be achieved with electron microscopy. The method was instrumental in the analysis of *in vivo* distribution of PS-NP, where the high autofluorescence of native tissues hinders the identification of particle fluorescence.

## 8. SUMMARY

In the present work the physicochemical characteristics and biological interactions of polymer nanoparticles were investigated, including *in vitro* cellular uptake and distribution in mouse tissues after a single intravenous NP-injection. During my dissertation work, I assessed the influence of the chemical composition of particle surfaces on the interaction of NPs with biological material.

The much larger proportion of surface-exposed atoms in nanoparticles provides unique properties compared to bulk materials, including enhanced chemical reactivity and large surface-energy. “Passivating” the surfaces of silica and polystyrene NPs with PEG- or PVP polymers, the reactivity of particles was decreased resulting in reduced aggregation and protein corona formation.

Experiments on the uptake of functionalized NPs by cultured neural stem- and tissue-type cells showed marked differences depending on both, the particle surface characteristics and the types of interacting cells. Particles with charged surface groups were taken up actively by microglia cells *in vitro*; while passivated NPs hardly interacted with phagocytic cells.

During the dissertation work my aim was to establish an imaging approach, which allows visualizing fluorescent NPs in various tissues. The detection of fluorescent NPs is hindered by their small size, which is below the resolution of diffraction limited systems, and by the high autofluorescence of biological samples. To overcome the limitations caused by high autofluorescence and low particle fluorescence, spectral imaging fluorescence microscopy was used. Spectral image acquisition combined with *post hoc* spectrum analysis could reliably detect fluorescent NPs in biological samples at the tissue- and cellular level.

With the established method I assessed the biodistribution and accumulation of NPs after a single intravenous injection in mice. Our *in vivo* NP-exposure data draws attention to a largescale and charge-independent accumulation of NPs in the reticuloendothelial organs.

## 9. ÖSSZEFOGLALÁS

Doktori munkám során fluorescens polimer nanopartikulumok fizikokémiai tulajdonságait és biológiai hatásait vizsgáltam, különös tekintettel a NP-ok sejtes internalizációra *in vitro* körülmények között, valamint egér szövetekben intravénás adminisztrációt követően. Munkám során arra kerestem a választ, hogy miképp változtatják meg a felszíni töltést befolyásoló funkciós csoportok a NP-ok biológiai viselkedését.

A NP-ok kivételes tulajdonságai kis méretükből és nagy fajlagos felületükből fakadnak, melynek következtében sokkal több atom helyezkedik el a struktúra felszínén a makroméretű részecskékhez képest. A felszíni atomok reakcióképessége nagyobb, változásuk a NP felszíni energiájára jelentős hatással van. Eredményeink szerint a passzíváló PEG- vagy PVP-csoporttal funkcionizált szilika és polisztirol NP-ok kevesebb kölcsönhatást alakítanak ki a környezettel, mint a töltéssel rendelkezők; valamint a passzívált felszínű NP-ok felszínén kialakuló protein korona is eltérő.

Munkám során vizsgáltam, hogyan befolyásolják a NP-ok felszíni töltését befolyásoló (pozitív-, negatív töltést eredményező vagy passzíváló) funkciós csoportok a NP-ok sejtes internalizációját. Megfigyeléseink szerint a partikulum-felvétel erősen függ mind a NP-felszín kémiai összetételétől, mind a kölcsönható sejt típusától. Idegszöveti sejtek tenyészteteiben a mikroglia sejtek aktív fagocitózissal internalizálták a részecskéket, mely folyamat a NP felszín passziválásával jelentősen csökkenthető volt.

Doktori munkám további részében céлом egy olyan képalkotó eljárás kidolgozása volt, mellyel fluoreszcens NP-ok sejtes felvétele vizsgálható változatos szövet mintákban. A NP-ok detektálását nehezíti kis méretük, mely a diffrakció által limitált mikroszkópos rendszerek felbontóképessége alatt marad, valamint a biológiai minták magas autofluoreszcenciája. A magas szöveti autofluoreszcencia és az alacsony NP-fluoreszcencia okozta detekciós korlátok leküzdésére spektrális képalkotású fluoreszcens mikroszkópiát alkalmaztam, mely *post hoc* spektrum analízissel kombinálva megbízhatóan detektálta a fluoreszcens NP-okat biológiai mintákban. A módszerrel polisztirol NP-ok *in vivo* eloszlását és hosszabb távú felhalmozódását vizsgáltam intravénás NP-adminisztrációt követően egerekben. Kapott eredményeink a retikuloendoteliális rendszerben végbemenő nagymértékű, töltéstől független NP-felhalmozódásra hívják fel a figyelmet.

**10. REFERENCES**

- Al-Rawi M, Diabaté S, Weiss C. (2011) Uptake and intracellular localization of submicron and nano-sized SiO<sub>2</sub> particles in HeLa cells. *Arch Toxicol* 85:813–26.
- Baghirov H, Karaman D, Viitala T, Duchanoy A, Lou Y-R, Mamaeva V, Pryazhnikov E, Khiroug L, Lange Davies C de, Sahlgren C, Rosenholm JM. (2016) Feasibility Study of the Permeability and Uptake of Mesoporous Silica Nanoparticles across the Blood-Brain Barrier. *PLoS One* 11:e0160705.
- Barenholz Y. (2012) Doxil® the first FDA-approved nano-drug: lessons learned. *J Control Release* 160:117–34.
- Begemann I, Galic M. (2016) Correlative Light Electron Microscopy: Connecting Synaptic Structure and Function. *Front Synaptic Neurosci* 8:28.
- Benezra M, Penate-Medina O, Zanzonico PB, Schaer D, Ow H, Burns A, DeStanchina E, Longo V, Herz E, Iyer S, Wolchok J, Larson SM, Wiesner U, Bradbury MS. (2011) Multimodal silica nanoparticles are effective cancer-targeted probes in a model of human melanoma. *J Clin Invest* 121:2768–80
- Blasi E, Barluzzi R, Bocchini V, Mazzolla R, Bistoni F. (1990) Immortalization of murine microglial cells by a v-raf/v-myc carrying retrovirus. *J Neuroimmunol* 27:229–37.
- Bouccara S, Sitbon G, Fragola A, Loriette V, Lequeux N, Pons T. (2015) Enhancing fluorescence in vivo imaging using inorganic nanoprobe. *Curr Opin Biotechnol* 34:65–72.
- Bradbury MS, Phillips E, Montero PH, Cheal SM, Stambuk H, Durack JC, Sofocleous CT, Meester RJC, Wiesner U, Patel S. (2013) Clinically-translated silica nanoparticles as dual-modality cancer-targeted probes for image-guided surgery and interventions. *Integr Biol (Camb)* 5:74–86.
- Bronte V, Pittet MJ. (2013) The spleen in local and systemic regulation of immunity. *Immunity* 39:806–18.
- Cao G, Wang Y. *Nanostructures and Nanomaterials*. World Scientific, Singapore, 2004: 1-141.
- Casals E, Pfaller T, Duschl A, Oostingh GJ, Puentes V. (2010) Time evolution of the nanoparticle protein corona. *ACS Nano* 4:3623–32.
- Casals E, Pfaller T, Duschl A, Oostingh GJ, Puentes VF. (2011) Hardening of the

- nanoparticle-protein corona in metal (Au, Ag) and oxide (Fe<sub>3</sub>O<sub>4</sub>, CoO, and CeO<sub>2</sub>) nanoparticles. *Small* 7:3479–86.
- Casals E, Puntès VF. (2012) Inorganic nanoparticle biomolecular corona: formation, evolution and biological impact. *Nanomedicine (Lond)* 7:1917–30.
- Champion JA, Mitragotri S. (2006) Role of target geometry in phagocytosis. *Proc Natl Acad Sci U S A* 103:4930–4.
- Chen F, Ehlerding EB, Cai W. (2014) Theranostic nanoparticles. *J Nucl Med* 55:1919–22.
- Chen S, Goode AE, Skepper JN, Thorley AJ, Seiffert JM, Chung KF, Tetley TD, Shaffer MSP, Ryan MP, Porter AE. (2016) Avoiding artefacts during electron microscopy of silver nanomaterials exposed to biological environments. *J Microsc* 261:157–166.
- Chilukuri N, Sun W, Naik RS, Parikh K, Tang L, Doctor BP, Saxena A. (2008) Effect of polyethylene glycol modification on the circulatory stability and immunogenicity of recombinant human butyrylcholinesterase. *Chem Biol Interact* 175:255–60.
- Cho M, Cho W-S, Choi M, Kim SJ, Han BS, Kim SH, Kim HO, Sheen YY, Jeong J. (2009) The impact of size on tissue distribution and elimination by single intravenous injection of silica nanoparticles. *Toxicol Lett* 189:177–83.
- Choi HS, Liu W, Misra P, Tanaka E, Zimmer JP, Iyengar I, Bawendi MG, Frangioni J V. (2007) Renal clearance of quantum dots. *Nat Biotechnol* 25:1165–70.
- Cohen JT, Carlson G, Charnley G, Coggon D, Delzell E, Graham JD, Greim H, Krewski D, Medinsky M, Monson R, Paustenbach D, Petersen B, Rappaport S, Rhomberg L, Ryan PB, Thompson K. (2002). A comprehensive evaluation of the potential health risks associated with occupational and environmental exposure to styrene. *J Toxicol Environ Health B Crit Rev* 5:1–265.
- Dickinson ME, Bearman G, Tille S, Lansford R, Fraser SE. (2001) Multi-Spectral Imaging and Linear Unmixing Add a Whole New Dimension to Laser Scanning Fluorescence Microscopy. *Biotechniques* 31:1272-1278.
- Elsaesser A, Howard CV. (2012) Toxicology of nanoparticles. *Adv Drug Deliv Rev* 64:129–37.
- Essa S, Rabanel JM, Hildgen P. (2011) Characterization of rhodamine loaded PEG-g-

- PLA nanoparticles (NPs): effect of poly(ethylene glycol) grafting density. *Int J Pharm* 411:178–87.
- European Parliament and the Council of the European Union. Regulation (EC) No 1272/2008: Labelling and Packaging of Substances and Mixtures. At: <http://echa.europa.eu/information-on-chemicals> EU, 2008.
- European Parliament and the Council of the European Union. Regulation (EU) No1129/2011: Establishing a Union List of Food Additives. At: <http://eur-lex.europa.eu> EU, 2011.
- European Chemicals Bureau, Institute for Health and Consumer Protection. European Union Risk Assessment Report - Styrene Part 1 Environment. 2002:27
- Fagerland J a, Wall HG, Pandher K, LeRoy BE, Gagne GD. (2012) Ultrastructural analysis in preclinical safety evaluation. *Toxicol Pathol* 40:391–402.
- Fang J, Chandrasekharan P, Liu X-L, Yang Y, Lv Y-B, Yang C-T, Ding J. (2014) Manipulating the surface coating of ultra-small Gd<sub>2</sub>O<sub>3</sub> nanoparticles for improved T1-weighted MR imaging. *Biomaterials* 35:1636–42.
- Filser JG, Gelbke HP. (2016). An evaluation of concentrations of styrene-7,8-oxide in rats and humans resulting from exposure to styrene or styrene-7,8-oxide and potential genotoxicity. *Toxicol Lett* 247:11–28.
- Firdessa R, Oelschlaeger TA, Moll H. (2014) Identification of multiple cellular uptake pathways of polystyrene nanoparticles and factors affecting the uptake: relevance for drug delivery systems. *Eur J Cell Biol* 93:323–37.
- Fleischer CC, Payne CK. (2014) Nanoparticle-cell interactions: Molecular structure of the protein corona and cellular outcomes. *Acc Chem Res* 47:2651–2659.
- Food and Drug Administration. Code of Federal Regulations - Food For Human Consumption At: [www.accessdata.fda.gov](http://www.accessdata.fda.gov) FDA, Silver Spring, 2013:177.1640
- Fröhlich E, Meindl C, Roblegg E, Ebner B, Absenger M, Pieber TR. (2012) Action of polystyrene nanoparticles of different sizes on lysosomal function and integrity. *Part Fibre Toxicol* 9:26.
- Gambinossi F, Mylon SE, Ferri JK. (2014) Aggregation kinetics and colloidal stability of functionalized nanoparticles. *Adv Colloid Interface Sci* 222:332–349.
- Garcia-Bennett AE. (2011) Synthesis, toxicology and potential of ordered mesoporous materials in nanomedicine. *Nanomedicine* 6:867–877.

- Gebel T, Foth H, Damm G, Freyberger A, Kramer P-J, Lilienblum W, Röhl C, Schupp T, Weiss C, Wollin K-M, Hengstler JG. (2014) Manufactured nanomaterials: categorization and approaches to hazard assessment. *Arch Toxicol* 88:2191–211.
- Gelbke HP, Banton M, Faes E, Leibold E, Pemberton M, Duhayon S. (2014) Derivation of safe health-based exposure limits for potential consumer exposure to styrene migrating into food from food containers. *Food Chem Toxicol* 64:258–269.
- Geng J, Zhu Z, Qin W, Ma L, Hu Y, Gurzadyan GG, Tang BZ, Liu B. (2014) Near-infrared fluorescence amplified organic nanoparticles with aggregation-induced emission characteristics for in vivo imaging. *Nanoscale* 6:939–45.
- Grafmueller S, Manser P, Diener L, Diener P-A, Maeder-Althaus X, Maurizi L, Jochum W, Krug HF, Buerki-Thurnherr T, Mandach U von, Wick P. (2015) Bidirectional Transfer Study of Polystyrene Nanoparticles across the Placental Barrier in an ex Vivo Human Placental Perfusion Model. *Environ Health Perspect* 123:1280-6.
- Hádinger N, Varga B V, Berzsenyi S, Környei Z, Madarász E, Herberth B. (2009) Astroglia genesis in vitro: distinct effects of retinoic acid in different phases of neural stem cell differentiation. *Int J Dev Neurosci* 27:365–75.
- Hardy CL, LeMasurier JS, Belz GT, Scalzo-Inguanti K, Yao J, Xiang SD, Kanellakis P, Bobik A, Strickland DH, Rolland JM, O’Hehir RE, Plebanski M. (2012) Inert 50-nm polystyrene nanoparticles that modify pulmonary dendritic cell function and inhibit allergic airway inflammation. *J Immunol* 188:1431–41.
- Hellstrand E, Lynch I, Andersson A, Drakenberg T, Dahlbäck B, Dawson KA, Linse S, Cedervall T. (2009) Complete high-density lipoproteins in nanoparticle corona. *FEBS J* 276:3372–81.
- Hirsch LR, Stafford RJ, Bankson JA, Sershen SR, Rivera B, Price RE, Hazle JD, Halas NJ, West JL. (2003) Nanoshell-mediated near-infrared thermal therapy of tumors under magnetic resonance guidance. *Proc Natl Acad Sci U S A* 100:13549–54.
- Hu F, Joshi HM, Dravid VP, Meade TJ. (2010) High-performance nanostructured MR contrast probes. *Nanoscale* 2:1884–91.
- Hu X, Gao X. (2010) Silica–Polymer Dual Layer-Encapsulated Quantum Dots with Remarkable Stability. *ACS Nano* 4:6080–6086.
- International Organisation for Standardization. *Nanotechnologies - Vocabulary - Part1: Core terms*. At: [www.iso.org](http://www.iso.org) ISO, London, 2015: ISO/TS 80004-1.

- Izak-Nau E, Kenesei K, Murali K, Voetz M, Eiden S, Puentes VF, Duschl A, Madarász E. (2013) Interaction of differently functionalized fluorescent silica nanoparticles with neural stem- and tissue-type cells. *Nanotoxicology* 5390:1–11.
- Izak-Nau E, Voetz M, Eiden S, Duschl A, Puentes VF. (2013) Altered characteristics of silica nanoparticles in bovine and human serum: the importance of nanomaterial characterization prior to its toxicological evaluation. Part *Fibre Toxicol* 10:56.
- Janssen B, Debets J, Leenders P, Smits J. (2002) Chronic measurement of cardiac output in conscious mice. *Am J Physiol Regul Integr Comp Physiol* 282:R928-35.
- Jung S, Aliberti J, Graemmel P, Sunshine MJ, Kreutzberg GW, Sher A, Littman DR. (2000) Analysis of fractalkine receptor CX(3)CR1 function by targeted deletion and green fluorescent protein reporter gene insertion. *Mol Cell Biol* 20:4106–14.
- Kenesei K, Murali K, Czéh Á, Piella J, Puentes V, Madarász E. (2016) Enhanced detection with spectral imaging fluorescence microscopy reveals tissue- and cell-type-specific compartmentalization of surface-modified polystyrene nanoparticles. *J Nanobiotechnology* 14:55.
- Kobayashi H, Ogawa M, Alford R. (2010) New Strategies for Fluorescent Probe Design in Medical Diagnostic Imaging. *Chem Rev* 2620-2640 p.
- Környei Z, Czirók a, Vicsek T, Madarász E. (2000) Proliferative and migratory responses of astrocytes to in vitro injury. *J Neurosci Res* 61:421–9.
- Krijnse Locker J, Schmid SL. (2013) Integrated electron microscopy: super-duper resolution. *PLoS Biol* 11:e1001639.
- Leary J, Key J. (2014) Nanoparticles for multimodal in vivo imaging in nanomedicine. *Int J Nanomedicine Volume* 9:711-26.
- Liba O, SoRelle E, Sen D, de la Zerda A. (2016) Contrast-enhanced optical coherence tomography with picomolar sensitivity for functional in vivo imaging. *Sci Rep* 6:23337.
- Lin W, Bazylnski DA, Xiao T, Wu L-F, Pan Y. (2014) Life with compass: diversity and biogeography of magnetotactic bacteria. *Environ Microbiol* 16:2646–2658.
- Liu Y, Hu Y, Huang L. (2014) Influence of polyethylene glycol density and surface lipid on pharmacokinetics and biodistribution of lipid-calcium-phosphate nanoparticles. *Biomaterials* 35:3027–3034.

- Lu J, Liong M, Li Z, Zink JI, Tamanoi F. (2010) Biocompatibility, biodistribution, and drug-delivery efficiency of mesoporous silica nanoparticles for cancer therapy in animals. *Small* 6:1794–805.
- Lundqvist M, Stigler J, Cedervall T, Berggård T, Flanagan MB, Lynch I, Elia G, Dawson K. (2011) The evolution of the protein corona around nanoparticles: a test study. *ACS Nano* 5:7503–9.
- Lundqvist M, Stigler J, Elia G, Lynch I, Cedervall T, Dawson KA. (2008) Nanoparticle size and surface properties determine the protein corona with possible implications for biological impacts. *Proc Natl Acad Sci U S A* 105:14265–70.
- Lunov O, Syrovets T, Loos C, Nienhaus GU, Mailänder V, Landfester K, Rouis M, Simmet T. (2011) Amino-functionalized polystyrene nanoparticles activate the NLRP3 inflammasome in human macrophages. *ACS Nano* 5:9648–57.
- Madarász E. Diversity of Neural Stem/Progenitor Populations: Varieties by Age, Regional Origin and Environment. In: Bonfanti L (editor) *Neural Stem Cells* InTech, Rijeka, 2013: 42-76.
- Madarasz E, Kiss J, Bartok I. (1984) Cell production and morphological pattern formation in primary brain cell cultures. I. Pattern formation within the basal layer(s). *Brain Res* 304:339–49.
- Mahler GJ, Esch MB, Tako E, Southard TL, Archer SD, Glahn RP, Shuler ML. (2012) Oral exposure to polystyrene nanoparticles affects iron absorption. *Nat Nanotechnol* 7:264–71.
- Mahon E, Salvati A, Baldelli Bombelli F, Lynch I, Dawson KA. (2012) Designing the nanoparticle-biomolecule interface for “targeting and therapeutic delivery.” *J Control Release* 161:164–174.
- Markó K, Ligeti M, Mezo G, Mihala N, Kutnyánszky E, Kiss E, Hudecz F, Madarász E. (2008) A Novel Synthetic Peptide Polymer with Cyclic RGD Motifs Supports Serum-Free Attachment of Anchorage-Dependent Cells. *Bioconj Chem* 1757–1766.
- Markó K, Kohidi T, Hádinger N, Jelitai M, Mezo G, Madarász E. (2011) Isolation of radial glia-like neural stem cells from fetal and adult mouse forebrain via selective adhesion to a novel adhesive peptide-conjugate. *PLoS One* 6:e28538.
- Merget R, Bauer T, Küpper HU, Philippou S, Bauer HD, Breitstadt R, Bruening T.

- (2002) Health hazards due to the inhalation of amorphous silica. *Arch Toxicol* 75:625–34.
- Milani S, Bombelli FB, Pitek AS, Dawson KA, Rädler J. (2012) Reversible versus irreversible binding of transferrin to polystyrene nanoparticles: soft and hard corona. *ACS Nano* 6:2532–41.
- Mo J, He L, Ma B, Chen T. (2016) Tailoring Particle Size of Mesoporous Silica Nanosystem To Antagonize Glioblastoma and Overcome Blood–Brain Barrier. *ACS Appl Mater Interfaces* 8:6811–6825.
- Moghimi SM, Porter CJH, Muir IS, Illum L, Davis SS. (1991) Non-phagocytic uptake of intravenously injected microspheres in rat spleen: Influence of particle size and hydrophilic coating. *Biochem Biophys Res Commun* 177:861–866.
- Monopoli MP, Aberg C, Salvati A, Dawson KA. (2012) Biomolecular coronas provide the biological identity of nanosized materials. *Nat Nanotechnol* 7:779–86.
- Moros M, Hernáez B, Garet E, Dias JT, Sáez B, Grazú V, González-Fernández A, Alonso C, la Fuente JM de. (2012) Monosaccharides versus PEG-functionalized NPs: influence in the cellular uptake. *ACS Nano* 6:1565–77.
- Murali K, Kenesei K, Li Y, Demeter K, Környei Z, Madarász EE. (2015) Uptake and bio-reactivity of polystyrene nanoparticles is affected by surface modifications, ageing and LPS adsorption: in vitro studies on neural tissue cells. *Nanoscale* 7:4199–210.
- Murugan K, Choonara YE, Kumar P, Bijukumar D, Toit LC du, Pillay V. (2015) Parameters and characteristics governing cellular internalization and trans-barrier trafficking of nanostructures. *Int J Nanomedicine* 10:2191–2206.
- Naczynski DJ, Andelman T, Pal D, Chen S, Riman RE, Roth CM, Moghe P V. (2010) Albumin nanoshell encapsulation of near-infrared-excitable rare-Earth nanoparticles enhances biocompatibility and enables targeted cell imaging. *Small* 6:1631–40.
- Nel AE, Mädler L, Velegol D, Xia T, Hoek EM V, Somasundaran P, Klaessig F, Castranova V, Thompson M. (2009) Understanding biophysicochemical interactions at the nano-bio interface. *Nat Mater* 8:543–57.
- OECD Environmental Directorate. Silicon dioxide - Manufactured nanomaterial. At: <http://www.oecd.org/chemicalsafety/nanosafety/silicon-dioxide-manufactured->

- nanomaterial.htm OECD, Paris, 2016:1-144.
- Ostrowski A, Nordmeyer D, Boreham A, Holzhausen C, Mundhenk L, Graf C, Meinke MC, Vogt A, Hadam S, Lademann J, Ruhl E, Alexiev U, Gruber AD. (2015) Overview about the localization of nanoparticles in tissue and cellular context by different imaging techniques. *Beilstein J Nanotechnol* 6:263–280.
- Paget V, Dekali S, Kortulewski T, Grall R, Gamez C, Blazy K, Aguerre-Chariol O, Chevillard S, Braun A, Rat P, Lacroix G. (2015) Specific uptake and genotoxicity induced by polystyrene nanobeads with distinct surface chemistry on human lung epithelial cells and macrophages. *PLoS One* 10:e0123297.
- Peracchia MT, Fattal E, Desmaële D, Besnard M, Noël J., Gomis J., Appel M, D'Angelo J, Couvreur P. (1999) Stealth® PEGylated polycyanoacrylate nanoparticles for intravenous administration and splenic targeting. *J Control Release* 60:121–128.
- Peracchia MT, Harnisch S, Pinto-Alphandary H, Gulik A, Dedieu JC, Desmaële D, D'Angelo J, Müller RH, Couvreur P. (1999) Visualization of in vitro protein-rejecting properties of PEGylated stealth® polycyanoacrylate nanoparticles. *Biomaterials* 20:1269–1275.
- Roduner E. (2006) Size matters: why nanomaterials are different. *Chem Soc Rev* 35:583–92.
- Ruenaroengsak P, Tetley TD. (2015) Differential bioreactivity of neutral, cationic and anionic polystyrene nanoparticles with cells from the human alveolar compartment: robust response of alveolar type 1 epithelial cells. *Part Fibre Toxicol* 12:19.
- Sacchetti C, Motamedchaboki K, Magrini A, Palmieri G, Mattei M, Bernardini S, Rosato N, Bottini N, Bottini M. (2013) Surface polyethylene glycol conformation influences the protein corona of polyethylene glycol-modified single-walled carbon nanotubes: potential implications on biological performance. *ACS Nano* 7:1974–89.
- Salvati A, Pitek AS, Monopoli MP, Prapainop K, Bombelli FB, Hristov DR, Kelly PM, Åberg C, Mahon E, Dawson KA. (2013) Transferrin-functionalized nanoparticles lose their targeting capabilities when a biomolecule corona adsorbs on the surface. *Nat Nanotechnol* 8:137–43.

- Saura J, Tusell JM, Serratos J. (2003) High-yield isolation of murine microglia by mild trypsinization. *Glia* 44:183–9.
- Schlett K, Herberth B, Madarász E. (1997) In vitro pattern formation during neurogenesis in neuroectodermal progenitor cells immortalized by p53-deficiency. *Int J Dev Neurosci* 15:795–804.
- Schlett K, Madarász E. (1997) Retinoic acid induced neural differentiation in a neuroectodermal cell line immortalized by p53 deficiency. *J Neurosci Res* 47:405–15.
- Schlöndorff D, Banas B. (2009) The mesangial cell revisited: no cell is an island. *J Am Soc Nephrol* 20:1179–87.
- Shah FA, Johansson BR, Thomsen P, Palmquist A. (2015) Ultrastructural evaluation of shrinkage artefacts induced by fixatives and embedding resins on osteocyte processes and pericellular space dimensions. *J Biomed Mater Res Part A* 103:1565–1576.
- Sokolowski JD, Mandell JW. (2011) Phagocytic clearance in neurodegeneration. *Am J Pathol* 178:1416–28.
- Spherotech Fluorescent particle catalog 2010-2011. At: [www.spherotech.com](http://www.spherotech.com), Spherotech, Lake Forest, 2010:1-5.
- Stöber W, Fink A, Bohn E. (1968) Controlled growth of monodisperse silica spheres in the micron size range. *J Colloid Interface Sci* 26:62–69.
- Strambeanu N, Demetrovici L, Dragos D. Natural Sources of Nanoparticles. In: Lungu CM, Neculae A, Bunoiu M (editors), *Nanoparticles' Promises and Risks*. Springer, Berlin, 2015: 9-19.
- Tang L, Cheng J. (2013) Nonporous Silica Nanoparticles for Nanomedicine Application. *Nano Today* 8:290–312.
- Tenzer S, Docter D, Kuharev J, Musyanovych A, Fetz V, Hecht R, Schlenk F, Fischer D, Kiouptsi K, Reinhardt C, Landfester K, Schild H, Maskos M, Knauer SK, Stauber RH. (2013) Rapid formation of plasma protein corona critically affects nanoparticle pathophysiology. *Nat Nanotechnol* 8:772–81.
- Vance ME, Kuiken T, Vejerano EP, McGinnis SP, Hochella MF, Rejeski D, Hull MS. (2015) Nanotechnology in the real world: Redeveloping the nanomaterial consumer products inventory. *Beilstein J Nanotechnol* 6:1769–1780.

- Varga B V, Hádinger N, Gócza E, Dulberg V, Demeter K, Madarász E, Herberth B. (2008) Generation of diverse neuronal subtypes in cloned populations of stem-like cells. *BMC Dev Biol* 8:89.
- Walcarius A, Ganesan V. (2006) Ion-exchange properties and electrochemical characterization of quaternary ammonium-functionalized silica microspheres obtained by the surfactant template route. *Langmuir* 22:469–77.
- Wang J, Jensen UB, Jensen G V, Shipovskov S, Balakrishnan VS, Otzen D, Pedersen JS, Besenbacher F, Sutherland DS. (2011) Soft interactions at nanoparticles alter protein function and conformation in a size dependent manner. *Nano Lett* 11:4985–91.
- Winkler HC, Suter M, Naegeli H. (2016) Critical review of the safety assessment of nano-structured silica additives in food. *J Nanobiotechnology* 14:44.
- Ye D, Dawson K a, Lynch I. (2015) A TEM protocol for quality assurance of in vitro cellular barrier models and its application to the assessment of nanoparticle transport mechanisms across barriers. *Analyst* 140:83–97.

## 11. PUBLICATIONS

### Publications related to the PhD dissertation

- Kenesei K, Murali K, Czéh Á, Piella J, Puentes VF, Madarász E. Enhanced detection with spectral imaging fluorescence microscopy reveals tissue- and cell-type-specific compartmentalization of surface-modified polystyrene nanoparticles. *Journal of Nanobiotechnology*, 2016 Jul 7;14(1):55. Impact factor: 4.239
- Murali K, Kenesei K, Li Y, Demeter K, Környei Zs, Madarász E. Uptake and bio-reactivity of polystyrene nanoparticles is affected by surface modifications, ageing and LPS adsorption: in vitro studies on neural tissue cells. *Nanoscale*, 2015 Mar 7;7(9):4199-210. Impact factor: 7.760
- Izak-Nau E, Kenesei K, Murali K, Voetz M, Eiden S, Puentes VF, Duschl A, Madarász E. Interaction of differently functionalized fluorescent silica nanoparticles with neural stem- and tissue-type cells. *Nanotoxicology*, 2014 Aug;8 Suppl 1:138-48. Impact factor: 6.411
- Demeter K, Kenesei K, Czéh Á, Török L, Orsolits B, Lustyik G, Madarász E. Cell labelling with functionalised nano-beads. Published abstract: *European Cells and Materials*, 2010, 20(3), 55. Impact factor: 9.650

### Other publications

- Lee SH, Ledri M, Toth B, Marchionni I, Henstridge CM, Dudok D, Kenesei K, Barna L, Szabó SzI, Renkecz T, Oberoi M, Watanabe M, Limoli CL, Horvai G, Soltesz I, Katona I. Multiple Forms of Endocannabinoid and Endovanilloid Signaling Regulate the Tonic Control of GABA Release. *J. Neurosci.* 2015 Jul 8;35(27):10039-57. Impact factor: 5.924

## 12. ACKNOWLEDGEMENTS

First and foremost, I would like to thank my supervisor, Prof. Emília Madarász, for her continuous support in my dissertation work, and that she promoted my scientific progress from the beginning of my studies. I would like to thank her, that being a part of her lab, I also got to know a very lively and inspiring scientific team in the NanoTOES programme. I would like to thank to Murali Kumarasamy, with whom I closely worked with on the topic of nano-bio interactions, to Emilia Izak-Nau, Kornél Demeter, Yang Li and Zsuzsa Környei who were co-authors in the publications giving the basis of the dissertation.

I would like to express my greatest thanks to all the past and present members of the Laboratory of Cellular and Developmental Neurobiology from whom I learned all the tricks in cell cultivation. Thank you all for the help and cheerful atmosphere in the lab.

Barabás, Kornélia	Jády, Attila	Murali, Kumarasamy
Demeter, Kornél	Jelitai, Márta	Nyámádi, Piroska
Fekete, Rebeka	Kóhidi, Tímea	Orsolits, Barbara
Gaál, Katalin	Környei, Zsuzsanna	Székács, Inna
Háding, Nóra	Markó, Károly	Szelényi, Judit
Herbeth, Balázs	Mészáros, Zsófia	Van-Weert, Szuzan

I would like to express my gratitude to colleagues at collaborative research laboratories: to Dr. György Lustyik and Dr. Árpád Czéh at Soft Flow Hungary Kft; to Dr. Victor Puentes and Jordi Piella at the Catalan Institute of Nanoscience and Nanotechnology for their valuable help with DLS measurements and to the QualityNano FP7 project for founding my experiments at ICN.

I wish to thank to the leaders and co-workers at IEM-HAS, that I could work at a high-standard scientific institute; and to Nikon Microscopy Center (NMC) at IEM, Nikon Austria GmbH and Auro-Science Consulting Ltd for kindly providing microscopy support.

I would like to thank to Dr. István Katona for the critical reading of my first authorship paper, and his support during the preparation of the thesis.

Last, but not least, I would like to express my greatest thanks to my friends and family for their unconditional support and encouragement during my studies and for all their help and patience during the preparation of my first author paper and PhD thesis.